UNIVERSITY OF CALIFORNIA,
IRVINE

Gravothermal Evolution of Generic Self-Interacting Dark Matter Models

DISSERTATION

submitted in partial satisfaction of the requirements
for the degree of

DOCTOR OF PHILOSOPHY

in Physics

by

Sophia Gad-Nasr

Dissertation Committee:
Professor Manoj Kaplinghat, Chair
Professor James S. Bullock
Professor Kevork N. Abazajian

2023

DEDICATION

I dedicate my Ph.D. thesis to my family, friends, and loved ones, who supported and believed in me. I honor my mother and father with this thesis, and every academic publication I have ever and will ever be part of by publishing under both family names, Gad and Nasr.

TABLE OF CONTENTS

LIST OF FIGURES

LIST OF TABLES

ACKNOWLEDGMENTS

I would like to express my gratitude and appreciation to my PhD advisor, Manoj Kaplinghat, for always believing in me, encouraging me, and helping me become the physicist I am today. It has been a tremendous honor and privilege to have had the opportunity to work so closely with you during these critical years of my academic life, and I look forward to many more collaborations with you. A special thank you to my undergraduate advisor, Sean Tulin, who sparked my passion for dark matter physics, who always believed in me, and with whom I had my first position after obtaining my PhD as a Visiting Postdoctoral Scholar. I can only hope other undergraduate students are as privileged as I was to have the opportunity to work with and be mentored by someone who can be as pivotal to their academic careers as you have been to mine. I am so grateful to have worked with you during my formative years as an undergraduate, and honored to continue working with you today.

I am extremely grateful for having had the opportunity to collaborate with and be mentored by some of the most incredible academics: Laura Sagunski, Kim Boddy, Nadav Outmezguine, Quinn Minor, Kevin Andrade, James Bullock, Kev Abazajian. I appreciate getting to learn from each and every one of you, and thank you for contributing to the physicist I am today.

Thank you to the Kaplinghat Research Group. Each and every single one of you and your unique talents have inspired me. Thank you to my class mates, office mates, and friends, for your camaraderie and making my graduate life so much brighter.

My life was made brighter by my tiny furry hamster friends, who left giant impressions that last a lifetime. It began with Furmi and Photini in undergrad, and continued with Neutrini who came with me from Toronto to sunny California. Sterlini and Axini, Gluini and Gravitini, each special and forever in my heart. Charmini and Muini, who stole our hearts. I miss each and every one of them.

Thank you to my father who instilled a love of math in me, my mother who believed in and supported me unconditionally, my brothers, Ramsey who showed me that anything is possible, is the best role model anyone can ask for, and made his home my own, and Sherif who showed me that creativity is worth more than numbers can ever sum up to, and to always stand up for myself. Without you, this would not be possible.

Kyle Kabasares, Ben Leffel, Olivia Dalager, Igor Palubski, and Edmund Witkowski, for being part of making my grad school years happy ones.

Elan Danohe, for being the light and making it all worthwhile.

I thank and acknowledge the Department of Physics and Astronomy at UC Irvine for granting me the Departmental Dissertation Fellowship in the Summer of 2023.

Elements of this work have been published in the Journal of Cosmology and Astroparticle Physics and Monthly Notices of the Royal Astronomical Society.

VITA

Sophia Gad-Nasr

RESEARCH INTERESTS Dark matter, galaxy formation and evolution, supermassive black hole formation, simulations, semi-analytic models.

EDUCATION

Doctor of Philosophy in Physics **2023**
University of California, Irvine *Irvine, CA*

Bachelor of Science in Astronomy and Astrophysics **2016**
York University *Toronto, Canada*

RESEARCH EXPERIENCE

Visiting Postdoctoral Scholar **2023**
York University *Toronto, Canada*

Graduate Research Assistant **2019-2023**
University of California, Irvine *Irvine, CA*

Undergraduate Research Assistant **2015-2016**
York University *Toronto, Canada*

TEACHING EXPERIENCE

Teaching Assistant **2017-2021**
University of California, Irvine *Irvine, CA*

FIRST-AUTHOR PUBLICATIONS (TO BE SUBMITTED)

On the Late-Time Evolution of Velocity-Dependent Self-Interacting Dark Matter Halos **2023**
MNRAS

OTHER REFEREED JOURNAL PUBLICATIONS

An unexpected high concentration for the dark substructure in the gravitational lens SDSSJ0946+1006 **2021**
MNRAS

Velocity-dependent self-interacting dark matter from groups and clusters of galaxies **2021**
JCAP

A Stringent Upper Limit on Dark Matter Self-Interaction Cross Section from Cluster Strong Lensing **2021**
MNRAS

Universal gravothermal evolution of isolated self-interacting dark matter halos for velocity-dependent cross sections **2023**
MNRAS

SELECTED PRESENTATIONS

Korea Astronomy and Space Science Institute Seminar **Jun 2023**
Gravothermal Evolution of Velocity-Dependent Self-Interacting Dark Matter Halos in the Short Mean Free Path Regime

UCLA Dark Matter Conference **Mar 2023**
Core Collapse in Self-Interacting Dark Matter Halo (joint poster presentation with colleague Maya Silverman)

iid2022 Conference: Statistical Methods for Events Data – Illuminating Dynamic Universe **Nov 2022**
Forming Supermassive Black Holes with the Collapse of Self-Interacting Dark Matter Halos

GalFRESCA Conference **Sept 2022**
Gravothermal Evolution of Self-Interacting Dark Matter Halos in the Long Mean Free Path Regime

SELECTED HONORS, AWARDS & FELLOWSHIPS

Zuckerman Postdoctoral Fellowship **2023-2024**
Zuckerman Postdoctoral Fellowship at the Technion–Israel Institute of Technology

Science Communication Fellowship **January 2020**
School of Physical Sciences, Department of Physics and Astronomy, UC Irvine

Outstanding Contributions to the Department Award **May 2018**
Department of Physics and Astronomy, UC Irvine

NSF GRFP Honorable Mention **April 2018**
National Science Foundation Graduate Research Fellowship Program

Charlene Anne Heisler Prize **October 2014**
Department of Physics and Astronomy, York University

ABSTRACT OF THE DISSERTATION

Gravothermal Evolution of Generic Self-Interacting Dark Matter Models

By

Sophia Gad-Nasr

Doctor of Philosophy in Physics

University of California, Irvine, 2023

Professor Manoj Kaplinghat, Chair

In self-interacting dark matter (SIDM) halos undergoing gravothermal evolution, the cores of halos are driven into the short-mean-free-path (SMFP) regime and undergo core collapse. In this dissertation, I study generic SIDM models with velocity-dependent cross-sections and elastic scattering, in SIDM halos experiencing gravothermal collapse. We study the structure and dynamics of halo cores in the SMFP and discover a new approximate universality deep in the SMFP regime. This new SMFP universality allows for the mapping of velocity-dependent cross sections to constant ones in this regime, offering improved predictions for physics occurring in the SMFP evolution of SIDM halos. We devise a semi-analytic recipe to predict the entire SMFP evolution of halos with our newfound SMFP universality by relating this new phase to the long-mean-free-path (LMFP) regime. This methodology streamlines the procedure of acquiring core properties within the SMFP regime and allows for estimates of the minimum mass of the black hole left behind, using simply the initial halo characteristics and particle physics parameters.

Chapter 1

Introduction

The field of cosmology strives to unravel the mysteries of our universe, tracing its evolution from the earliest moments to its eventual fate. A fundamental goal of this field is to determine the universe's composition, which includes the mysterious and elusive dark matter, constituting approximately 27% of the universe's total mass-energy density. In contrast, baryonic matter makes up about 5%, while dark energy comprises the remaining 68%. These components, along with the flat spacetime geometry of the universe, form the cornerstone of the standard cosmological model known as Λ-Cold Dark Matter (ΛCDM). The role of dark matter is pivotal in the formation of cosmic structures, making its study crucial for understanding the universe's structural evolution.

The concept of dark matter was first proposed by Swiss astrophysicist Fritz Zwicky in the 1930s. Observing the Coma cluster and using the virial theorem, Zwicky discovered that the visible matter was insufficient to account for the observed galactic velocities, leading him to conclude that there must be a large amount of invisible matter holding the cluster together [159, 160]. He called it "dunkle Materie", which means "dark matter" in German [159]. It was not until the 1970s that the concept of dark matter gained traction,

thanks to American astronomer Vera Rubin and her colleague Kent Ford. Their observations of the Andromeda galaxy's rotation curve revealed stars moving at nearly constant speeds irrespective of their distance from the center [122]. These observations furnished the first compelling evidence of dark matter's existence, ushering an enduring quest for a particle that, until this day, remains elusive.

The ΛCDM model has served as the standard cosmological framework in the fields of cosmology and astrophysics. Its successes are undeniable: it provides an accurate description of large scale structure and the Cosmic Microwave Background (CMB) [135, 111, 137]. However, the model faces challenges on small scales[1] [84, 148]. These challenges include the "core-cusp" problem, where observed dark matter halos display central cores instead of the predicted CDM cusps [94, 51], the "missing satellites" problem regarding the discrepancy in the predicted and observed number of satellite galaxies in the Local Group [79, 51], the "too big to fail" problem related to the absence of massive galaxies predicted by ΛCDM [19], and the diversity problem concerning the variation observed in dwarf and low surface brightness galaxy rotation curves that cannot be explained by CDM [105].

To address these discrepancies, researchers have proposed alternative models to ΛCDM, with many focusing on a dynamic dark sector. A prominent candidate is self-interacting dark matter (SIDM), where dark matter particles scatter via non-gravitational interactions. SIDM emerged as a solution to the small-scale issues, initially featuring constant cross-section contact interactions that transformed central density cusps into cores, thus addressing the core-cusp dilemma [135]. Recent observations suggest that the SIDM cross-section must be velocity-dependent to align with observations at both dwarf and cluster scales [1, 139, 75]. This enables SIDM to maintain the large scale successes of ΛCDM while resolving its small scale conflicts. The self-interactions in SIDM give rise to gravothermal evolution, potentially

[1]See Appendix A.2 for a detailed account of these problems.

explaining the formation of supermassive black holes (SMBHs) in the early universe [8, 7, 50, 83, 91, 103, 106, 112].

In this dissertation, I present a series of significant contributions I have made to the study of dark matter, particularly focusing on the exploration of SIDM. These include my substantial work in a study where I use the IllustrisTNG simulations [99] to highlight the challenges CDM faces in explaining the high concentration of a dark substructure observed in the gravitational lens SDSSJ0946+1006 [92]. This study underscores the limitations of the standard CDM paradigm in certain astrophysical contexts.

Furthermore, I have co-authored research supporting velocity-dependent cross sections in SIDM [124]. This work tests the effects of adiabatic contractions on the SIDM cross section, examines the concentration-mass relation for SIDM, and places the first group scale constraints on the SIDM cross section.

In another key piece of research I co-authored that explores the long-mean-free-path (LMFP) regime of SIDM halos undergoing gravothermal evolution [106], I made significant contributions to generalizing the LMFP self-similar and universal solutions to velocity dependent cross sections for the first time.

Finally, I led a study that uncovers a new universality in the short-mean-free-path (SMFP) evolution of SIDM halos [58]. This work provides a comprehensive characterization of the SMFP evolution of halos. A noteworthy achievement of this research is the development of a method to analytically predict key characteristics of the cores of SIDM halos undergoing SMFP evolution, assuming elastic scattering. This semi-analytic framework bypasses the necessity of running time-intensive numerical gravothermal code, thereby streamlining future research in this area. It enables a deeper exploration of gravothermal evolution in SIDM halos and provides a guide for future simulations investigating black hole formation from gravothermal collapse.

Collectively, my research contributions advocate for exploring the dark sector and emphasize the necessity of velocity-dependent cross sections in dark matter self-interactions. This perspective is bolstered by emerging studies indicating the presence of core-collapsed halos in dwarf galaxies [130], as well as the potential of core collapse to produce supermassive black hole seeds [7, 50, 91, 103, 55].

The subsequent sections of this chapter will outline critical topics in cosmology, examine the evidence supporting the existence of cold dark matter, introduce the concept and motivations behind SIDM, and explore the particle physics aspects of SIDM. The following chapters will detail my contributions and address the significance of the problems addressed in each project. Finally, I will conclude by summarizing the implications of SIDM and gravothermal collapse in our quest to understand the particle physics nature of SIDM, in an effort to unravel the longstanding question of the particle properties of dark matter.

1.1 Modern Cosmology

Cosmology delves into the profound questions regarding the universe's origin, structure, evolution, and ultimate fate. It seeks to understand what the universe is composed of and the laws governing its behavior. Its main framework, the Standard Model of Cosmology, is commonly referred to as the ΛCDM model. Here, Λ stands for the cosmological constant, representing dark energy, within a flat and homogeneous universe, while CDM is cold dark matter. This model is predicated on key assumptions. Chief among them is Einstein's Theory of General Relativity, which provides the framework for understanding the universe's geometry and dynamics. Additionally, the model assumes that the universe is homogeneous and isotropic at large scales. This uniformity, however, breaks on small scales, yielding to

tiny density fluctuations[2] in the Cosmic Microwave Background (CMB), the vestiges that have guided the formation of galaxies we observe today.

The ΛCDM model further posits that the laws of physics are invariant across the universe and throughout its history. It postulates that the universe was birthed from a hot, dense state called the Big Bang, and experienced a period of rapid inflation. Integral to this model is the existence of dark matter and dark energy, which are crucial to the universe's evolutionary history. This section is based on material in the following sources: [42, 123, 86, 68].

1.1.1 Standard Model of Cosmology in a Homogeneous Universe

The foundation of the standard model of cosmology is based on the Friedmann-Lemaitre-Robertson-Walker (FLRW) metric, which describes a universe that is both homogeneous and isotropic. For a Euclidean (spatially flat) universe, the FLRW metric can be expressed as follows:

$$\begin{aligned} ds^2 &= g_{\mu\nu} dx^\mu dx^\nu \,, \\ g_{00}(\mathbf{x}, t) &= -1 \,, \\ g_{0i}(\mathbf{x}, t) &= 0 \,, \\ g_{ij}(\mathbf{x}, t) &= a^2(t)\delta_{ij}, \end{aligned} \tag{1.1}$$

where $a(t)$ represents the scale factor.

[2]These fluctuations are on the order of 1 part in 100,000 [42, 123].

The Friedmann equations, which are derived from Einstein's field equations, form the backbone of the cosmological model. The field equations are:

$$\begin{aligned} G_{\mu\nu} + \Lambda g_{\mu\nu} &= 8\pi G T_{\mu\nu}\,, \\ G_{\mu\nu} &\equiv R_{\mu\nu} - \frac{1}{2} g_{\mu\nu} R\,, \\ R &\equiv g^{\mu\nu} R_{\mu\nu}\,, \end{aligned} \tag{1.2}$$

where $G_{\mu\nu}$ is the Einstein tensor, $R_{\mu\nu}$ is the Ricci tensor, R is the Ricci scalar, and $T_{\mu\nu}$ is the energy-momentum tensor.

The Friedmann equations succinctly encapsulate the dynamics of a homogeneous and isotropic universe:

$$\begin{aligned} H^2(t) = \left(\frac{\dot{a}}{a}\right)^2 &= \frac{8\pi G}{3}\rho - \frac{\kappa}{a^2}\,, \\ \frac{\ddot{a}}{a} &= -\frac{4\pi G}{3}(\rho + 3\mathcal{P})\,, \end{aligned} \tag{1.3}$$

Here, H denotes the Hubble parameter, ρ is the density, $\mathcal{P}$ is the pressure, and κ is the curvature term, which is negligible in a flat universe.

A key concept is the density parameter, derived by normalizing the density to the critical density $\rho_{\rm cr} = 3H_0^2/8\pi G$ and recasting Eq. 1.3 in terms of the Hubble constant H_0:

$$\frac{H^2(t)}{H_0^2} = \frac{\rho(t)}{\rho_{\rm cr}} = \sum_s \Omega_s [a(t)]^{-3(1+w_s)} + \Omega_K [a(t)]^{-2}\,, \tag{1.4}$$

Ω_s refers to the density parameter for each constituent s (radiation, neutrinos, matter, dark energy) of the universe, with w_s as the equation of state parameter for each constituent. The term Ω_K, which signifies curvature, is negligible for a flat universe.

The geometry of the universe is encoded within these parameters. A universe with $\Omega < 1$ exhibits negative curvature, while $\Omega > 1$ implies positive curvature. In our universe, $\Omega = 1$

indicates flat geometry, hence $\Omega_K = 0$. These equations not only govern the expansion and geometry of space but also detail the evolution of the scale factor a, which encapsulates the expansion history of the universe. The matter energy density evolves with the expansion as $\propto a^{-3}$, radiation energy density as $\propto a^{-4}$, while the cosmological constant Λ remains invariant through the expansion.

1.1.2 Cosmological Redshift

Cosmological redshift is a fundamental concept in observational cosmology, offering a crucial link between the observed properties of distant celestial objects and the universe's expansion. This phenomenon occurs as the universe expands, causing the wavelengths of photons traveling through space to stretch, thus shifting them towards longer, redder wavelengths — a process known as "redshifting."

To understand this better, it is useful to relate the scale factor of the universe to the redshift. This relationship is described as[3]:

$$a = \frac{1}{1+z}\,, \tag{1.5}$$

where z represents the redshift. It is important to note that redshift, as a measurable quantity, is integral to observational astronomy. This is because redshift allows us to calculate the distance to celestial objects by assessing the extent to which the light they emit has been redshifted. The equation for redshift is given by:

$$z = \frac{\lambda_{\text{obs}} - \lambda_{\text{emit}}}{\lambda_{\text{emit}}}\,, \tag{1.6}$$

[3]More generally, the equation is $\frac{a_e}{a_0} = \frac{1}{1+z_e}$ where the subscript e stands for "emitted" (it is the scale factor and redshift taken at the time the photons measured were emitted), and a_0 is the scale factor today, which is equal to 1. Setting $a_0 = 1$, and removing the subscripts e, yields the equation given.

where λ_{emit} is the wavelength of the light at the time it was emitted, and λ_{obs} is the wavelength observed upon reaching our telescopes. Additionally, redshift serves as a valuable metric for estimating the universe's rate of expansion.

1.1.3 Distances in an Expanding Universe

Understanding distances in an expanding universe is crucial in cosmology. The expansion of the universe is characterized by the Hubble parameter, $H(t)$, which describes the rate of expansion as a function of time. Its inverse, the Hubble time $t_H = H(t)^{-1}$, approximates the age of the universe, assuming a linear expansion since the Big Bang.

The Hubble time can be used as a gauge for the time scale of processes on cosmological scales. For example, processes with time scales shorter than a Hubble time occur within the age of the universe, and thus, should be observable. We determine the universe's age through the lookback time, defined as:

$$t_l = \int_{t_e}^{t} dt' = \int_{a_e}^{a_0} \frac{da'}{\dot{a}'}\,, \tag{1.7}$$

where we have used Eq. (1.3) to transform from t to a. Transforming this into a form involving redshift z, we get:

$$t_{\text{age}} = \frac{1}{H_0} \int_0^z \frac{dz'}{(1+z')E(z')}\,, \tag{1.8}$$

with $E(z)$ representing the Hubble parameter's evolution:

$$\frac{H(z)}{H_0} \equiv E(z) = \sqrt{\Omega_m(1+z)^3 + \Omega_r(1+z)^4 + \Omega_\Lambda + \Omega_k(1+z)^2}\,. \tag{1.9}$$

This formulation is more practical since the redshift z is an observable.

The Hubble radius $D_H = aH^{-1}$ marks the distance at which objects recede at light speed. Objects beyond this distance recede faster than light, yet we can observe some objects that were within the Hubble radius at the time when they emitted the light now reaching us. The particle horizon defines the observable universe's boundary, marking the farthest distance from which light could have reached us since the Big Bang. The cosmic event horizon, conversely, delineates the boundary beyond which light emitted today will never reach us.

Measuring distances in an expanding universe involves understanding both proper and comoving distances. Proper distance is the physical distance between two points at a given time, increasing over time due to expansion. Comoving distance measures the distance with the universe's expansion factored out, and is thus unaffected by the expansion. The comoving distance along the line of sight is expressed as:

$$\chi = \int_{z_1}^{z_2} c \frac{dz'}{H(z')} \,. \tag{1.10}$$

The proper distance is thus simply $D_p = a(t)\chi$.

The angular diameter distance D_A, another crucial measurement, relates an object's angular diameter in our sky to its physical size, accounting for the effects of the expansion. Interestingly, up to about $z \sim 1$, the angular size of an object appears to increase, but decreases beyond $z \sim 1$. For a flat universe, D_A is given by:

$$D_A = \frac{D_M}{1+z} \,, \tag{1.11}$$

where the transverse comoving distance $D_M = \chi$ as given in Eq. (1.10) for a flat universe, $D_M = D_H \Omega_k^{-1/2} \sinh\left(\Omega_k^{1/2} \chi / D_H\right)$ for a negatively curved universe with $\Omega_k > 1$, and $D_M = D_H (|\Omega_k|)^{-1/2} \sin\left((|\Omega_k|)^{1/2} \chi / D_H\right)$ for a positively curved universe with $\Omega_k < 1$. Another useful quantity to measure with observations is the luminosity distance. When we observe distant objects, the light we see is dimmed r^{-2}, and redshifted due to the universe's

expansion. Assuming the luminosity of an object is known, as is the case with type 1a supernovae which always have the same luminosity and are used as standard candles in astronomy, you can then relate the flux of the object to its luminosity and distance through $F \equiv L/(4\pi D_L^2)$. With this, one can find its distance after factoring in the effects of redshift:

$$D_L = (1+z)D_M = (1+z)^2 D_A \,. \tag{1.12}$$

With these distances, we can correlate observations with theoretical models, enhancing our understanding of the universe's expansion and structure.

1.1.4 Inhomogeneous Universe and Structure Formation

Structure formation in the universe is a process that originates from the minute quantum fluctuations during the inflationary period, a phase of rapid exponential expansion in the early universe [67]. These initial fluctuations grew with the expansion, and once frozen in at the end of inflation, became the seeds for the cosmic structures we observe today. Without these perturbations, our universe would be represented by the idealized perfectly homogeneous metric in Eq. (1.1), and would lack the rich breadth of galaxies, clusters, and large-scale structures we see today.

The true state of our universe is better captured by a perturbed metric, a deviation from the ideal homogeneity in Eq. (1.1), can be expressed as[4]:

$$\begin{aligned} g_{00}(\mathbf{x},t) &= -1 - 2\Psi(\mathbf{x},t)\,, \\ g_{0i}(\mathbf{x},t) &= 0\,, \\ g_{ij}(\mathbf{x},t) &= a^2(t)\delta_{ij}[1+2\Phi(\mathbf{x},t)]\,. \end{aligned} \tag{1.13}$$

[4]This perturbed metric is given in the Newtonian gauge. A full treatment can be found in [96].

In this perturbed framework, Ψ represents the Newtonian potential affecting nonrelativistic objects under gravity, and Φ signifies the perturbations in local spatial curvature, crucial for structure formation independent of the universe's expansion. These perturbations originate in the inflation field and grow as space expands post-inflation.

A key component in this process is dark matter, which, due to its non-interaction with radiation, can clump unobstructed by radiation pressure and form halos. These halos, initially small in size and mass, gradually merge to form larger structures in a hierarchical manner, a cornerstone concept in the CDM model.

To understand the evolution of these structures, we rely on the following fundamental equations:

Continuity Equation:

$$\frac{\partial \rho}{\partial t} + \nabla \cdot (\rho \mathbf{v}) = 0\,. \tag{1.14}$$

This equation underlines the conservation of mass within a fluid and governs the time evolution of density perturbations.

Euler's Equation:

$$\frac{\partial \mathbf{v}}{\partial t} + (\mathbf{v} \cdot \nabla)\mathbf{v} = -\frac{1}{\rho}\nabla p - \nabla \Phi\,. \tag{1.15}$$

This encapsulates the momentum conservation dynamics of the fluid.

Poisson's Equation:

$$\nabla^2 \Phi = 4\pi G \rho\,. \tag{1.16}$$

This equation links the gravitational potential Φ to the matter distribution, which is vital for understanding gravity's role in shaping density perturbations.

The fractional overdensity, an essential concept in structure formation, is defined as:

$$\rho = \rho_0 \left(1 + \delta + \mathcal{O}(\delta^2)\right) , \tag{1.17}$$

where $\delta = \delta\rho/\rho_0$ represents the density contrast. In the linear regime where $\delta \ll 1$, higher-order terms become negligible.

Lastly, the evolution of matter distribution becomes a statistical endeavor, described by the Boltzmann equation:

$$\frac{df}{dt} = C[f] , \tag{1.18}$$

where df/dt governs the collisionless interactions with a distribution function f that depends on the particle species, while $C[f]$ is a collision term for fluids with particle interactions. This equation governs the evolution of particle distributions, accounting for both collisionless and collisional interactions.

The distribution function for neutrinos is given by the Fermi-Dirac distribution, and for photons, by the Bose-Einstein distribution. These distribution functions are very important because these particles are relativistic in the early universe. For non-relativistic particles like baryons and CDM, because their velocities are much smaller than the speed of light, a Maxwellian distribution is typically sufficient.

1.2 Cold Dark Matter

The concept of CDM is pivotal in our understanding of the universe's structure and evolution. CDM is crucial for explaining the observable small-scale structures in the cosmos. For dark matter particles to form such structures, they needed to be "cold," or non-relativistic, at the time of their freeze-out [13, 12, 42]. This characteristic implies that they were moving slower than the universe's expansion rate. Had they been "hot," moving at relativistic speeds, they would have washed out the small-scale structure [13, 135, 42].

The freeze-out of CDM occurs when the universe cools sufficiently, and the rate of particle interactions falls below the expansion rate of the universe. This moment depends on various properties of the dark matter particles, such as mass and interaction characteristics [42]. After this freeze-out, the number density of CDM particles becomes fixed, and they effectively become invisible, ceasing to interact with other particles [42, 13, 12].

Though invisible, the presence of dark matter is inferred through its gravitational interactions. Evidence for its existence comes from astrophysical phenomena such as rotation curves of galaxies, gravitational lensing effects, dynamics of galaxy clusters, large-scale structure of the universe, and the Cosmic Microwave Background (CMB).

In simulations, CDM is often represented using the Navarro-Frenk-White (NFW) profile [97, 98], a model that has been validated through numerous N-body simulations. The NFW profile is mathematically described as:

$$\rho_{\mathrm{NFW}}(r) = \frac{\rho_s}{(r/r_s)(1 + r/r_s)^2}\,, \tag{1.19}$$

where ρ_s, r_s represent the scale density and radius, respectively. It is important to note that real astrophysical systems exhibit variations due to factors like stellar and gas content, adiabatic contraction, and tidal disruptions, which can modify the profile away from the

idealized NFW form. However, the NFW profile is a good approximation for the dark matter halo.

1.2.1 Rotation curves

One of the most compelling pieces of evidence for dark matter comes from the observation of galactic rotation curves. Vera Rubin and her colleague Kent Ford discovered the first compelling evidence for dark matter in the rotation curve of M31 Andromeda galaxy [122]. Rotation curves plot the circular velocity of stars with respect to the distance from the center of the galaxy, where the circular velocity is given by

$$v_{\rm circ}^2 = \frac{GM(r)}{r}\,, \tag{1.20}$$

where $M(r)$ is the enclosed mass given by $M(r) = 4\pi \int_0^r \rho(r')r'^2 dr'$, r is the distance from the center, and G is the gravitational constant [14]. The expectation, then, is that the circular velocities drop as $r^{-1/2}$, but what is observed is a different picture: velocities remain relatively constant right our to the edge of the galaxy, as seen in Fig. 1.1. This clearly implies that a large amount of unseen matter is present.

1.2.2 Galaxy clusters

Galaxy clusters, the largest gravitationally bound structures in the universe comprised of as many as 1000 galaxies bound together under gravity, reveal that there is more mass than visible matter alone can account for. Fritz Zwicky inferred that there was at least 400 times more matter than the visible mass can account for in the Coma cluster [159]. He estimated the mass using the virial theorem which states that a gravitationally bound system in steady-state obeys $2\langle T\rangle + \langle U\rangle = 0$ [52, 14, 28, 133].

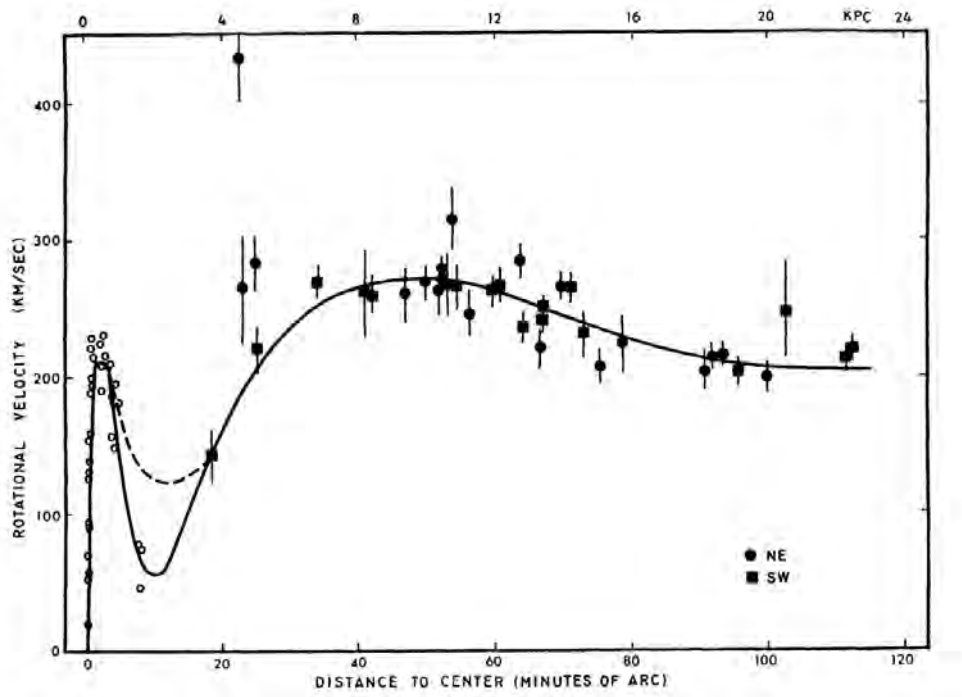

Figure 1.1: Plot of the rotational velocities of OB stars in the Andromeda galaxy. The data points are rotational velocities derived from the N II emission lines of bright OB stars. The solid curve is a polynomial fit to the data. [122]

While he overestimated the mass by a factor of ~ 10 due to the Hubble constant being very inaccurate at the time, he accurately determined that there was much more matter than that which is visible [14].

Additional evidence for dark matter comes from X-ray emission of hot gas, which makes up ~ 10 times more mass in clusters than the stars do [26, 108]. A great example is yet again the Coma cluster, which contains a large amount of hot gas detected in X-rays with temperatures of 8.11 keV ($\sim 1 \times 10^8$ K) [20]. Since the galaxy mass is only $\sim 10\%$ of the gas mass, it can not provide the required gravitational potential to hold such a large amount of gas at such extreme temperatures, which indicates that the gravitational potential holding onto the gas is sourced by dark matter [57].

The Bullet Cluster, as depicted in Fig. 1.2, stands as a crucial piece of empirical evidence supporting the existence of dark matter. This object is the result of a high-speed collision

~ 4700 km/s [26, 113], between two galaxy clusters. A notable aspect of the Bullet Cluster is its composition: it possesses a significantly higher proportion of mass in gas ($5-15\%$ of the total mass) compared to stars (about $1-2\%$ of the total mass) [108]. Given that stars behave as collisionless particles, in contrast to gas which experiences interactions, this scenario presents an ideal opportunity to study dark matter. In such a collision, dark matter, like stars, would be expected to exhibit collisionless behavior and thus pass through the clusters along with the stars, whereas the gas would lag behind due to the drag from its collisional properties. This is precisely what gravitational lensing observations reveal: the majority of the clusters' mass aligns with the galaxies themselves, not with the gas [26]. This conclusion is shown in Fig. 1.2. The left panel of the figure shows contours tracing the positions of the clusters post-collision, while the right panel overlays these contours onto an X-ray image depicting the location of the gas. There is a clear offset between the gas distribution and the peaks in the contour map, indicating that the primary mass component in the Bullet Cluster is not the visible gas, but rather, dark matter. These observations from the Bullet Cluster provide strong evidence for the existence of dark matter, demonstrating that the majority of mass in these clusters is unseen, consistent with the theoretical predictions and characteristics of dark matter.

1.2.3 Cosmic Microwave Background

The Cosmic Microwave Background (CMB) provides some of the most compelling evidence for the existence of dark matter. It is a relic from the time when the universe was approximately $400,000$ years old, capturing crucial details about the universe's composition and the evolution of cosmic structures.

The CMB is essentially a snapshot of the early universe, revealing temperature anisotropies that are the result of density perturbations present at that time. This snapshot can be seen

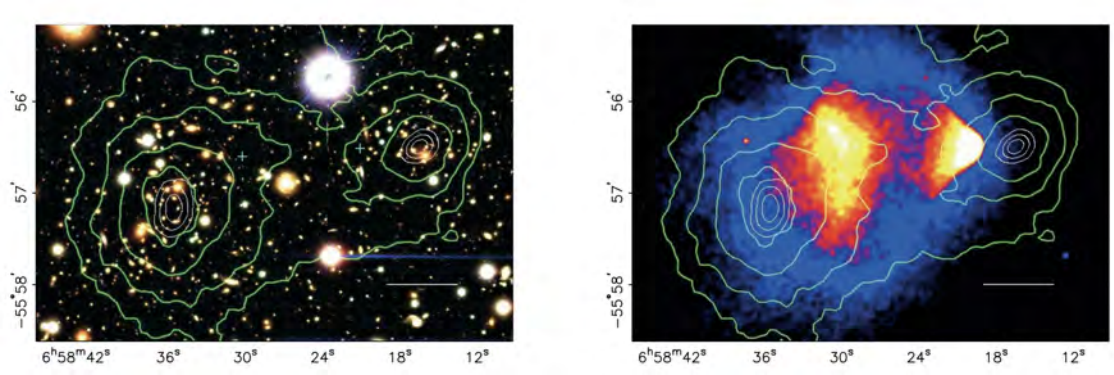

Figure 1.2: Left: Color images of the Bullet Cluster, taken by the Magellan. Right: Image of the Bullet cluster from the Chandra X-ray Observatory. In both panels, the white bar corresponds to 200 kpc, and the green contours are the κ from weak lensing (see §A.1 for more on lensing). The white contours are the 68.3%, 95.5%, and 99.7% confidence level of the peak positions. The blue plus symbols are the locations that were used for the center of the gas clumps. [26]

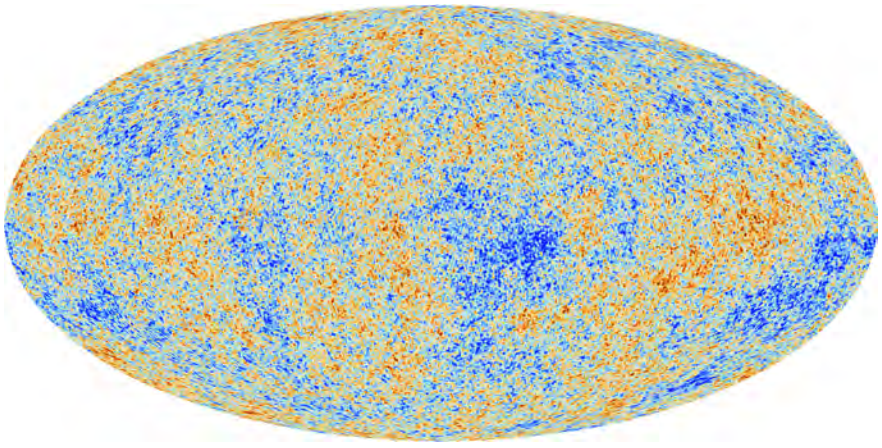

Figure 1.3: Anisotropies in the CMB showcasing temperature variations, with the red spots corresponding to colder and denser regions, and blue spots to regions that are hotter and less dense. Credit: ESA and Planck Collaboration.

in Fig. 1.3, from data taken by the Planck observatory. These perturbations, influenced by gravity, grew over time and eventually led to the formation of the large-scale structures observed in the current universe.

Analyzing the CMB involves studying its power spectrum, which characterizes the amplitude of temperature fluctuations across different scales, as shown in Fig. 1.4 [150]. This power spectrum is crucial for understanding the early universe's composition and the interplay between various constituents, including baryons, photons, and dark matter.

The temperature fluctuations in the CMB are closely related to the baryon acoustic oscillations (BAO) created by the interplay between baryons and photons in the early universe, when they were tightly coupled. Radiation pressure prevented baryons from collapsing gravitationally into overdense regions, causing them to undergo BAO. Dark matter, uninhibited by radiation pressure, was able to clump under gravity to form the seeds for our universe's structure.

The power spectrum's peaks (see Fig. 1.4) provide insights into the universe's shape and matter content. The first peak's position indicates the universe's curvature. In the CMB power spectrum, the location of this peak (around $l \sim 200$) corresponds to a flat universe. A negatively curved universe would show smaller perturbations (higher l), and a positively curved one would show larger perturbations (lower l).

The second peak in the power spectrum is a direct consequence of BAO and sheds light on the universe's baryon content. The ratio of the heights of the second to the first peak helps determine the proportion of the universe's energy density composed of baryons.

The third peak in the power spectrum is particularly informative about the amount of dark matter in the universe. Its amplitude is influenced by the depth of the potential wells created by dark matter. A higher third peak suggests deeper wells, indicating a significant presence of

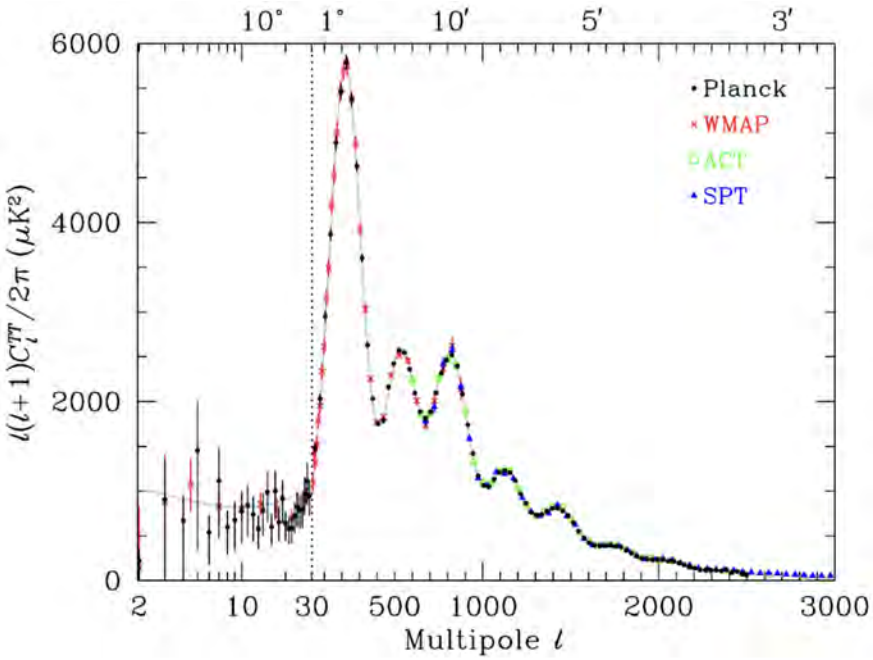

Figure 1.4: Power spectrum of the CMB, showing the amplitude of the temperature fluctuations with respect to the scale, or multipole. Larger multipoles correspond to smaller scales. The points with error bars are data from Planck, WMAP, ACT, and SPT (the error in the multipoles is not shown here). The curve is the predicted ΛCDM model from Planck. Acoustic peaks appear at the largest scales (lowest multipoles, as well as a damping region for the smallest scales (highest multipoles). From [150].

dark matter. The similar amplitude of the third peak to the second peak suggests that dark matter was the dominant component of matter density during this period of the universe.

1.2.4 Large Scale Structure

The large-scale structure in the universe formed from the seeds created by dark matter during BAO, when matter was pushed out of the overdensities while dark matter was able to clump together. This formed a cosmic web, a vast and intricate network of galaxies, clusters, and filaments throughout the universe. This structure is seen in N-body simulations like the Millennium Simulation, as shown in the right panel of Fig 1.5. In N-body simulations, only the physics of gravity, as it pertains to CDM, is taken into account. The resulting cosmic web seen in these simulations is a testament to the role of dark matter in shaping the universe.

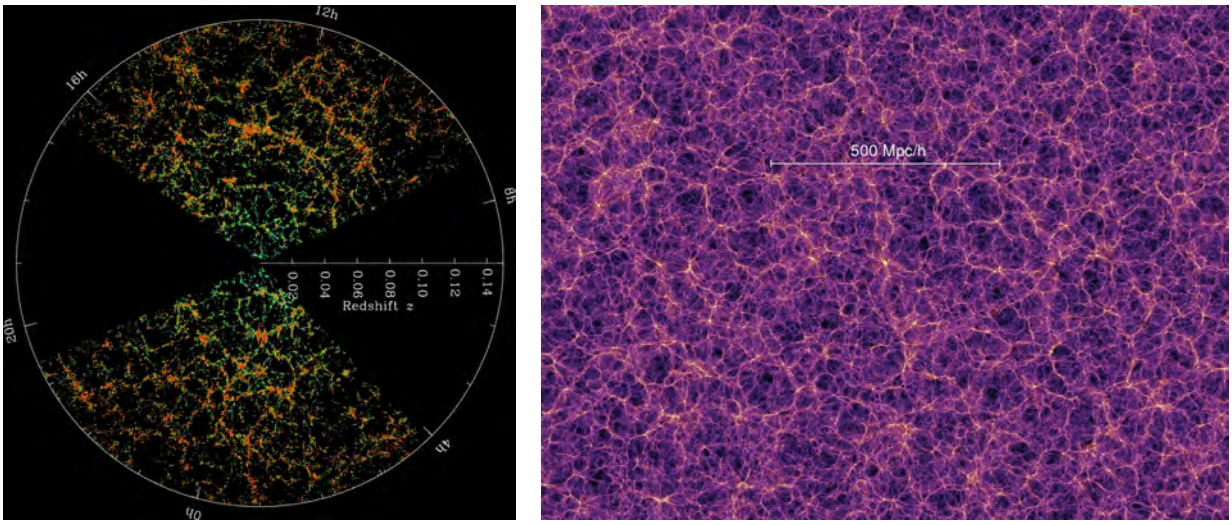

Figure 1.5: Left: 3D map of the distribution of galaxies out to 2 Gly from the Sloan Digital Sky Survey (SDSS). Each point represents a galaxy colored by age, with redder being older. The regions in the two gaps that are void of data were not mapped due to the dust in the Milky Way obscuring the view of the SDSS. Credit: M. Blanton and the Sloan Digital Sky Survey [155]. Right: A slice of the dark matter distribution from the Millennium simulation. The slice has a thickness of 15 Mpc/h. The full N-body simulation has a box length of 500 Mpc/h. Credit: Millennium Simulation.

In contrast, baryonic matter, which interacts with photons, was subject to pressure that caused it to oscillate in and out of the overdense regions. This oscillation hindered the ability of baryons alone to form the complex cosmic web observed today. Essentially, baryons decoupled too late to be able to create the observed large-scale structure within the time necessary to explain observations today.

This theoretical understanding is strongly supported by observational data. For example, the 3D map of the universe from the Sloan Digital Sky Survey (SDSS) (shown in the left panel of Fig 1.5) reveals patterns that strikingly resemble those produced in the CDM simulations (seen in the right panel of Fig 1.5). The similarity between these observed structures and CDM simulations underscores the importance of dark matter in the formation and evolution of the universe's large-scale structure.

1.3 Particle Physics of SIDM

In understanding the particle physics of SIDM, it is essential to consider the broader context of dark matter research and the motivations behind exploring models beyond the CDM paradigm. While the ΛCDM model has been successful in explaining large-scale structures in the universe, it encounters challenges at smaller scales (see Appendix A.2 for a detailed account of these small-scale challenges). This has led to a growing interest in alternative dark matter models.

Classes of well-motivated dark matter models include particles borne out of symmetries proposed to address inconsistencies in the Standard Model (SM) of particle physics, and those that might interact through yet undetected dark forces [32, 66]. Despite extensive searches, weakly-interacting massive particles, or WIMPs, which are a primary candidate in the first class of models, have not been detected [5]. This lack of detection has shifted the focus of particle physicists towards the second class of models, which include dark sector particles and forces and access a new range of parameter space [1, 32, 66].

The dark sector is characterized by dark matter self-interactions, mediated by new dark forces. The dark matter can be multi-component, involving more than one type of particle [112], and can manifest either as elastic scattering, where energy is conserved (as discussed in my recent work [106] and others [8, 16, 75, 1]), or as inelastic, where scattering is dissipative [17, 50, 151]. One of the most promising dark sector models is SIDM featuring a velocity-dependent cross-section, a natural feature of Yukawa models with a light boson mediator [139]. From a particle physics standpoint, velocity-dependent interactions could be a hint for the existence of a rich dark sector, comprised of more than one particle.

1.3.1 The Dark Sector

The dark sector encompasses a range of particles and forces which constitute dark matter that may or may not be coupled to the SM. It could be composed of one or more particles that may interact with each other through dark sector forces [53]. SIDM postulates that interactions among dark matter particles with a dark sector force can lead to thermalization in halos and redistribution of mass, offering solutions to the small-scale challenges faced by CDM (see Appendix A.2). These interactions can be mediated by a light mass mediator like a dark photon, typically in the mass range of $1 - 100\,\mathrm{MeV}$ [74, 131]. These interactions can also arise through resonant scattering which does not require the introduction of light particles [140, 138]. The interaction Lagrangian for such models varies depending on the mediator. A model with a light mediator can be described by a vector boson where dark matter particles are charged under a spontaneously broken $U(1)$ symmetry and interact through gauge boson exchange, or a scalar boson that mediates self-scattering between dark matter particles. These interactions can be represented as follows:

$$\mathscr{L}_{\mathrm{int}} = \begin{cases} g_\chi \bar{\chi} \gamma^\mu \chi \phi_\mu & \text{(vector mediator)} \\ g_\chi \bar{\chi} \chi \phi & \text{(scalar mediator)} \end{cases} , \tag{1.21}$$

Here, χ denotes the dark matter particle, ϕ represents the mediator, and g_χ is the dark matter coupling constant.

Interactions between the dark sector and the SM, if present, can occur through various mechanisms. Photon kinetic mixing involves the SM photon mixing with a light mass mediator like a dark photon [131, 74]. Z boson mass mixing involves a new dark sector Z' boson mixing with the SM Z boson [74], while the Higgs portal coupling involves a scalar

dark sector particle interacting with the SM scalar Higgs boson [74]. Given an SM coupling opens up potential avenues for direct detection of dark matter in experiments [74, 131].

1.3.2 Yukawa Potential and Velocity Dependence

Yukawa potential The velocity dependence of the interaction cross section of SIDM serves as a guideline for model building [124, 139, 130]. This velocity dependence emerges naturally in Yukawa interactions, mediated by a light mediator [1, 16, 139]. This interaction can be described by a Yukawa potential [75] which is characterized by

$$V(r) = \pm\frac{\alpha_\chi}{r}e^{-m_\phi r}\,, \tag{1.22}$$

where $\alpha_\chi \equiv g_\chi/4\pi$ is the dark fine structure coupling constant, m_ϕ is the mass of the mediating particle, and r is the distance between interacting particles. The $+(-)$ sign indicates that the interactions are attractive (repulsive) [139, 75].

Velocity dependence The velocity-dependent scattering cross-section is a hallmark of SIDM that is natural in Yukawa models. It can lead to observable effects on the structure of dark matter halos on small scales while leaving large scales unchanged. The velocity dependence is such that the cross section diminishes as the relative velocity increases [139].

The scattering amplitude, representing the interaction probability of SIDM particles, is the solution to the Schrödinger equation. Solving the Schrödinger equation can be computationally expensive. The Born approximation, applicable in the $\alpha_\chi m_\chi \ll m_\phi$ regime (where m_χ is the mass of the dark matter particle), simplifies this by assuming minimal alteration of the wave during scattering [139, 140]. The Born differential cross section is [140]

$$\frac{d\sigma}{d\Omega} = \frac{\alpha_\chi^2 m_\chi^2}{\left(m_\chi^2 v_{\rm rel}^2 (1-\cos\theta)/2 + m_\phi^2\right)^2}\,, \tag{1.23}$$

where $v_{\rm rel}$ is the relative velocity between the scattering dark matter particles. It must be stressed that Eq. (1.23) is only applicable in the $\alpha_\chi m_\chi \ll m_\phi$ limit; in the resonant regime, the Schrödinger equation must be solved. See [140] for a treatment of the resonant regime.

Cross sections Two cross-sections often used to study SIDM interactions in simulations are the momentum transfer cross-section and the viscosity cross-section. They are given by

$$\begin{aligned} \sigma_T &= \int d\Omega (1-\cos\theta)\frac{d\sigma}{d\Omega}\,, \\ \sigma_V &= \int d\Omega \sin^2\theta \frac{d\sigma}{d\Omega}\,, \end{aligned} \tag{1.24}$$

where $d\Omega$ is over the solid angle [119, 140]. The momentum transfer cross section, σ_T, emphasizes the forward momentum transfer, and is weighted by $(1-\cos\theta)$ which measures the longitudinal momentum transfer, $\Delta p = p(1-\cos\theta)$. Conversely, the viscosity cross section, σ_V, emphasizes transverse scattering, weighted by $\sin^2\theta$. The viscosity cross section accounts for the fact that forward and backward scattering impact the dark matter halo equally, and that scattering in the perpendicular direction is the most efficient for halo thermalization.

Velocity dependence is incorporated through the differential cross section. For Rutherford-like scattering with only t-channel contributions, it is expressed as [69, 153]:

$$\frac{d\sigma}{d\Omega} = \frac{\sigma_0}{4\pi\left(1+\frac{v^2}{w^2}\sin^2\frac{\theta}{2}\right)^2}\,, \tag{1.25}$$

where the normalization prefactor is $\sigma_0 = 4\pi\alpha_\chi^2/\left(m_\chi^2 w^4\right)$ and α_χ is the dark fine structure constant as defined in Eq. (1.22), $w = m_\phi c/m_\chi$ is the characteristic velocity, v is the relative velocity between scattering particles, and θ is the scattering angle of the particles. For Møller-like scattering with t- and u-channel contributions, the differential cross section is [153]:

$$\frac{d\sigma}{d\Omega} = \frac{1}{\pi}\frac{\sigma_0 w^4[(3\cos^2\theta + 1)v^4 + 4v^2w^2 + 4w^4]}{(\sin^2\theta v^4 + 4v^2w^2 + 4w^4)^2}. \tag{1.26}$$

The choice between momentum transfer and viscosity cross sections depends on the specific scenario of SIDM interactions. In the case for Møller-like scattering where particles are indistinguishable, the viscosity cross-section should be used as it minimizes forward and backward scattering which do not affect the distribution of dark matter in the halo, while emphasizing transverse scattering which plays a crucial role in thermalizing the halo [140, 29]. The momentum transfer cross section, on the other hand, is not well defined for identical particles and cannot distinguish between forward and backward scattering when particles are indistinguishable [140, 29]. It is thus more useful for interactions where forward scattering plays a significant role.

Chapter 2

Testing CDM and Motivating Physics Beyond CDM using Gravitational Lensing

The text in this chapter is based on work in [92]. I was not the lead, but my role in this paper was substantial. The entire analysis performed using the IllustrisTNG simulations [99] was performed by me, and most of the section was written by me. I will cite the paper and use "we" and "our" to distinguish work that was not done by me, but is necessary for context.

2.1 Introduction

In the quest to reveal the properties of dark matter, the study of dark matter substructures and their influence on gravitational lensing has garnered significant attention. The gravitational lens galaxy SDSSJ0946+1006 has emerged as a pivotal system for the study of

dark matter, having previously been identified to possess an invisible substructure through its perturbative effects on lensed images [144].

In this chapter, I will discuss the results of this work where we constrain, for the first time, the concentration of the observed substructure in SDSSJ0946+1006, and tested its consistency with CDM predictions. We employed a two-pronged approach, using observations and testing them with simulations. For the observational work, the lead author [92] used strong lensing models to probe the dark substructure in SDSSJ0946+1006 to extract parameters like the inner log-slope of the projected density profile, and the dark matter mass within a 1 kpc radius. For the simulations, I used the state-of-the-art suite of CDM simulations, IllustrisTNG [99], to obtain theoretical predictions for the substructure's properties and test against the parameters extracted from the observations. The combination of observed data with simulated predictions laid the groundwork for the crucial findings of this work.

The substructure in SDSSJ0946+1006 is characterized by a drastically high concentration as compared with the CDM prediction of a similar mass halo using the concentration-mass relation of [46]. This is accompanied by an inordinately steep slope in the inner projected density. To constrain substructure, we can use something called the perturbation radius [93], which is the radius within which the gravitational influence of the substructure is dominant (it is from the subhalo center to the most perturbed part of the critical curve). It turns out this radius is about $\sim$ 1 kpc. We determined the substructure's projected mass within a 1 kpc radius to be approximately between $2 - 3.7 \times 10^9\, M_\odot$, and the average log-slope of the projected density profile within 0.75-1.25 kpc was steeper than isothermal [92]. We also established an upper limit for the luminosity of the perturber of $L = 1.2 \times 10^8\, L_\odot$.

To juxtapose these findings, I selected analogue subhalos in the IllustrisTNG simulation, both in the hydrodynamical runs as well as the dark-matter-only (DMO) ones, thereby providing a test of the effect of adiabatic contractions from the baryons. I also accounted for selection bias, a phenomenon where the triaxiality of dark matter halos yields the possibility

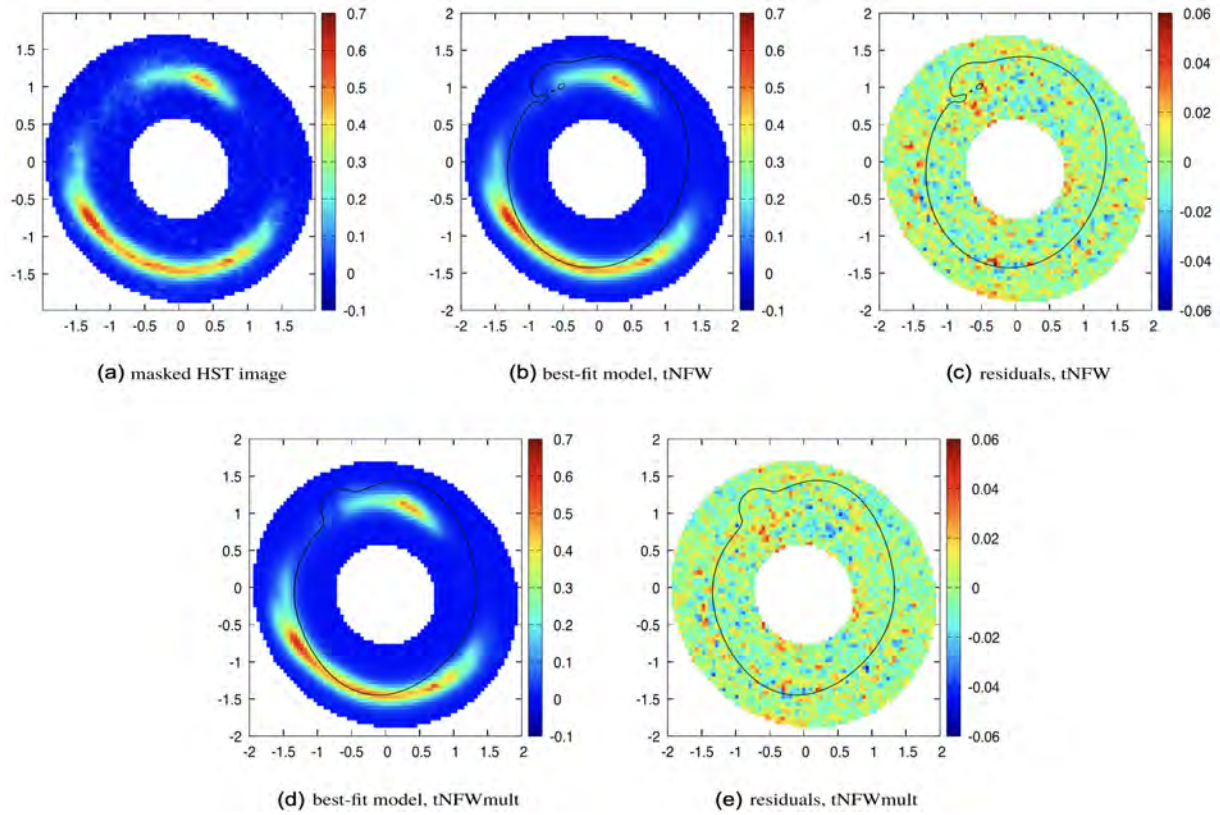

Figure 2.1: Masked HST image from [59] along with tNFW and tNFWmult models and their residuals. Also seen is the critical curve, which shows the perturbation by the dark substructure in the upper left. [92]

of them being positioned such that the line-of-sight is along the long axis, producing stronger lensing [129]. I will lay out that, despite having a substantial sample size of over 2000 subhalos in our sample from the hydrodynamical simulation and nearly 5000 subhalos in DMO, we conclude that the existence of such a dark, highly concentrated subhalo is at odds with the predictions of a ΛCDM universe, motivating dark sector models for dark matter.

2.2 Lensing model and results

In this study, four lensing models were employed to study the substructure in the lensing galaxy SDSSJ0946+1006. The two main models used were an elliptical truncated NFW (tNFW) profile [9] for the subhalo, as well as a tNFW profile with multipoles (tNFWmult),

which is the same as the tNFW but allowing for departures from ellipticity through the multipoles. The inclusion of multipoles is supported by the presence of perturbations in the isophotes that may have been caused by a recent interaction with a nearby galactic neighbor [59, 132], as well as the model used by [144] who found a preference for smooth corrections. The critical curve from these models can be seen in Fig. 2.1, which reveal a strong perturbation in the upper left due to the substructure.

For the purpose of testing how robustly constrained the density profile is, other models were tested, such as the "cuspy halo model" [95] (the CoreCusp model in [4]), and an additional CoreCusp with multipoles (CoreCuspmult). The results can be seen in Fig. 2.2. Between 0.5–1 kpc, for each panel, the slopes are generally the same. This makes it a useful observable for comparing to simulations. However, due to resolution limitations, [92] derived a parameter in which the slope of the projected density is measured between 0.75–1.25 kpc, $\gamma_{2\mathrm{D}}(0.75 - 1.25\,\mathrm{kpc})$. It turns out that this parameter is correlated with r_s and c_{200}.

To see how well suited the projected mass at the perturbation radius (approximately 1 kpc) is for constraining substructures, look at the projected mass profiles of both the tNFW and tNFWmult models in Fig. 2.3. While the profiles differ, at right around 1 kpc, the profiles cross and have around the same projected mass. This further supports the use of the projected mass within the perturbation radius (for this subhalo, 1 kpc) as a robust way to constrain the properties of dark substructure, as was done in [93].

With the tNFW model, a subhalo mass of $4.69 \times 10^9\,M_\odot$ is obtained, along with an extraordinarily high concentration of 1560. The tNFWmult model gives a more reasonable concentration of 70.5, and a subhalo mass $2.61 \times 10^{10}\,M_\odot$ [92]. Comparing to the concentration-mass relation of [46], these concentrations deviate by at least 5σ. For the projected mass within a 1 kpc radius, [92] found a range $2 - 3.7 \times 10^9\,M_\odot$, a log-slope of the inner density of $\gamma_{2D}(0.75 - 1.25\,\mathrm{kpc}) < -1$, specifically -1.98, -1.27, -3.27, and -1.79 for

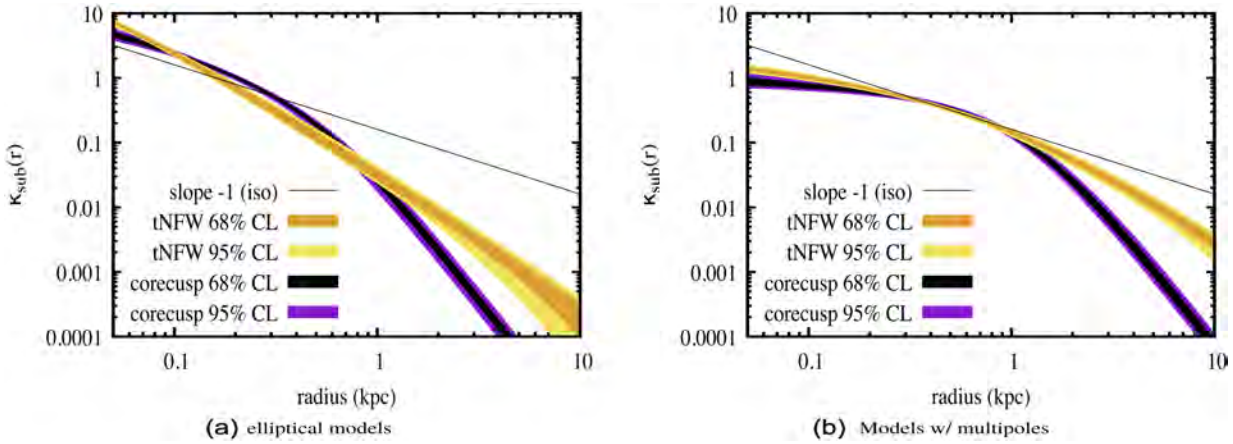

Figure 2.2: Projected density profiles for the elliptical models (left panel) and models with multipoles (right panel). [92]

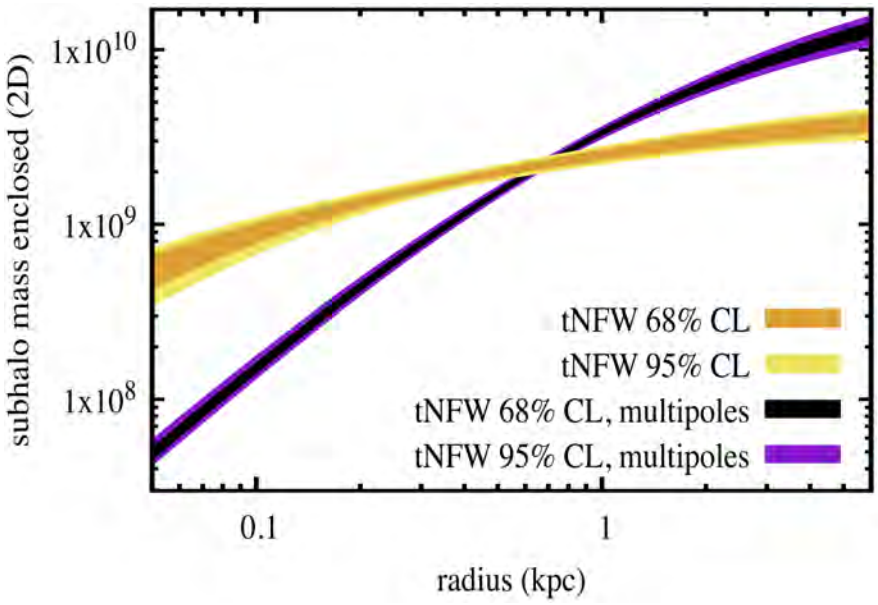

Figure 2.3: Projected mass profiles for the tNFW and tNFWmult models. While the mass profiles differ substantially, near the perturbation radius at around 1 kpc, the projected masses converge to a similar value. [92]

tNFW, tNFWmult, CoreCusp, and CoreCuspmult respectively, and an upper bound on the luminosity of $L < 1.2 \times 10^8\, L_\odot$ [92].

2.3 Comparison to the IllustrisTNG Simulations

For this portion of the work, the three bounds obtained by [92] that are essential for accurately representing the dark substructure are as follows: $M_{2\mathrm{D}}(1\,\mathrm{kpc}) \gtrsim 2 \times 10^9\,\mathrm{M}_\odot$, $\gamma_{2\mathrm{D}} < -1$, $L_V < 1.2 \times 10^8\, L_\odot$. To test the consistency of the substructure with CDM, I used these bounds to find analog subhalos in the IllustrisTNG simulations to compare [99].

For a relevant comparison, we must account for baryonic effects on galaxy mass distributions, as radiative cooling and subsequent adiabatic contraction of the dark matter halo will lead to denser galaxies with larger Einstein radii than those in DMO simulations [15, 65]. Baryonic processes, especially adiabatic contraction and AGN feedback, influence subhalo distribution and mass functions [37]. We utilize the IllustrisTNG suite, which offers both hydrodynamical and DMO simulations. The hydrodynamical suite includes gas cooling effects and subgrid physics, including star and black hole dynamics and feedback mechanisms. In contrast, the DMO suite of simulations are N-body, representing only collisionless CDM with gravity.

2.3.1 Sample Selection of Analog Subhalos

For a comprehensive test of the effect of baryons on subhalos, we analyze both the hydrodynamical and DMO simulations in IllustrisTNG, specifically TNG100-1 and TNG100-1-DARK. These simulations have box lengths of 100 Mpc and dark matter particle masses of $7.5 \times 10^6 M_\odot$ and $8.9 \times 10^6 M_\odot$, respectively. Given the resolution, subhalos with masses below $7.5 \times 10^9 M_\odot$ may be unresolved, leading to potential inaccuracies [24]. Thus, our analysis is

confined to subhalos with dark matter masses $5 \times 10^9 M_\odot$ or larger to ensure ~ 1000 particles per subhalo.

To identify analogues of the dark substructure, I used a similar method to that of [37]. I scanned the TNG100-1 simulations, targeting host halos at redshift $z = 0.2$ with total masses between $1 \times 10^{13} - 6 \times 10^{13} M_\odot$ and stellar masses from $8 \times 10^{10} - 8 \times 10^{12} M_\odot$. Subhalos of these hosts were selected based on total masses ranging from $8 \times 10^9 - 4 \times 10^{11} M_\odot$ and dark matter masses between $5 \times 10^9 M_\odot - 4 \times 10^{11} M_\odot$. I identified 3056 subhalos from 167 hosts in the hydrodynamical run and 4909 subhalos from 188 hosts in the DMO run. After filtering out subhalos with insufficient star particles or projected mass, 2205 subhalos remained for the hydrodynamical run.

For each subhalo, I constructed density profiles by binning particles in radial mass bins. For the 2D mass and surface density profiles, I shot 1000 random lines of sight (LOS) through each subhalo, binned the particles in cylindrical shells, and averaged over the LOS for each halo. Given the triaxial nature of dark matter halos, the LOS along the long axis of a halo can amplify projected density and thus lensing, introducing selection bias [129]. We thus selected the LOS with the projected density in 1 kpc in the top 10th percentile, in order to examine the effect of selection bias. To determine the 2D density profile slope, γ_{2D}, we fitted a power law to the profile between $0.75 - 1.25$ kpc.

2.3.2 Comparison of Sample to Lensing Constraints

In Fig. 2.4 I have plotted the projected dark matter (DM) mass within 1 kpc, $M_{2D,DM}(1\text{kpc})$, against the total subhalo mass for both hydrodynamical and DMO simulations. From the tNFWmult band, we see that only subhalos with a total mass around $\sim 10^{10} M_\odot$ or greater meet the required $M_{2D,DM}(1\text{kpc})$. Subhalos below this threshold were excluded, which eliminated many subhalos with low stellar mass.

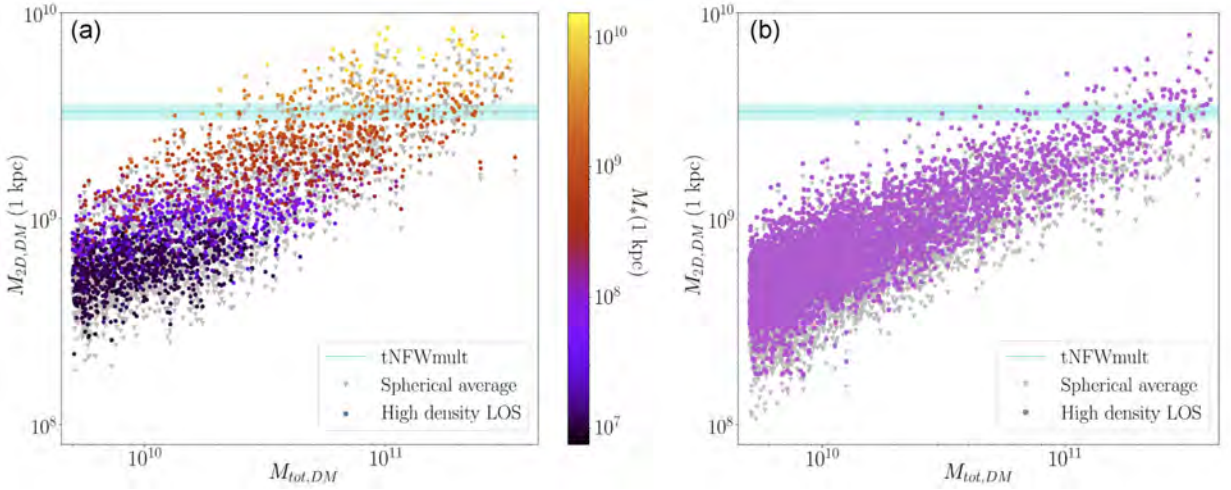

Figure 2.4: Projected dark matter mass within 1 kpc with respect to the total mass for subhalo sample in the hydrodynamical run (left panel (a)) and DMO run (right panel (b)). Gray triangle points are the full spherical average over 1000 LOS, and colored circles are the LOS giving the top 10% highest density in 1 kpc. Panel (a) circles are color-coded by $M_*(1$ kpc). We include the 2σ error bands for $M_{2D,DM}(1$ kpc) in the tNFWmult model.

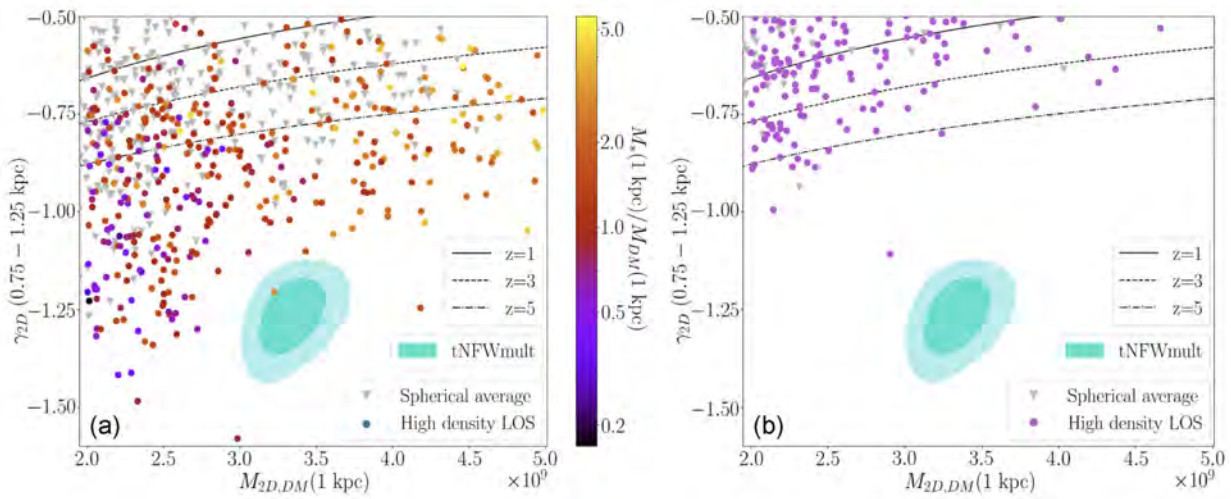

Figure 2.5: Slope of the surface density profile versus projected mass in 1 kpc. Here, we limit the sample to the range $M(1 \text{ kpc}) = 2 - 5 \times 10^9 M_\odot$ and $\gamma_{2D} \leq -0.5$ for both the hydrodynamical (panel (a)) and DMO (panel (b)) runs. Color conventions for markers are the same as in Fig. 2.4. Both panels include the 68% and 95% contours from lensing constraints for the tNFWmult model. Included is the cosmological relation for dark matter for z = 1, 3, 5 at 3σ.

The right panel of Fig. 2.4 reveals a correlation: as the projected halo mass within 1 kpc increases, so does the stellar mass in the same region. This means that CDM predictions can only align with lensing results if the subhalos also have a stellar mass of at least $\sim 2\times10^8 M_\odot$ within 1 kpc, which conflicts with the lower stellar mass suggested by the observational data.

For the density slope analysis, we focused on the log-slope of the projected density profile of the subhalos. Due to resolution constraints, we used the range between 0.75 and 1.25 kpc to determine the average log-slope, γ_{2D}, for each subhalo. Looking at Fig. 2.5 and comparing the hydrodynamical and DMO simulations, the DMO data exhibits a markedly milder slope and fewer subhalos meeting the M_{2D}(1kpc) criteria. This discrepancy is expected due to the baryonic effects of adiabatic contraction and tidal stripping in the hydrodynamical simulations, making the subhalo sample denser, especially for larger subhalo masses.

Our findings highlight the significance of the LOS in determining density profiles, and show that selection bias indeed is a problem. The DMO run, in particular, showed greater triaxiality, consistent with previous studies that show that baryons make halos more spherical [44, 77]. Also plotted in Fig. 2.5 are the lensing constraints as 68% and 95% contours, which reveal that most of the subhalos in our hydrodynamical sample do not have a steep enough slope to match lensing data. Only a fraction of the hydrodynamical sample met the slope constraints when selection bias is amplified, while none aligned with both the inferred slope and M_{2D}(1kpc) when averaged across all LOS. The DMO data was even less consistent, with no subhalos achieving the required slope.

2.3.3 Concentration of the Subhalo in SDSSJ0946+1006

I explored the likelihood of observing a perturber as concentrated as the one in SDSSJ0946+1006 with our subhalo sample. To smooth out noise in the density profiles, I averaged over 20 nearby LOS for each subhalo, serving as mock observations to determine

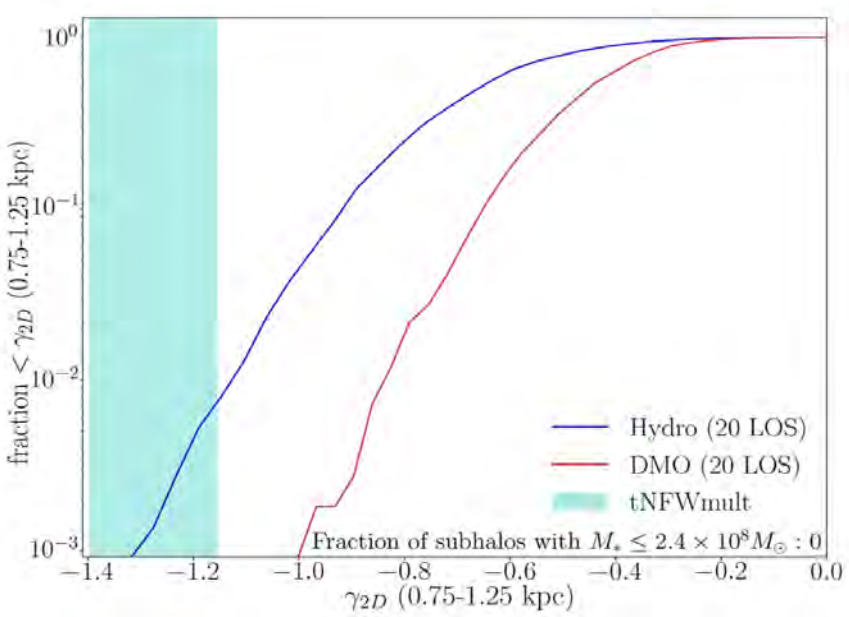

Figure 2.6: Fraction of mock observations in our sample that have a log-slope steeper than a given threshold γ_{2D}(0.75-1.25kpc). Only observations where M_{2D}(1kpc) is within $3-4\times 10^9 M_\odot$ are included. The 95% confidence in γ_{2D} from our tNFWmult model is shown as the vertical shaded bar. Each subhalo in our mock observations is averaged over 20 similar LOS. Fewer than 1% satisfy the lensing constraints.

the projected mass and density slope. Fig. 2.6 illustrates that less than 1% of these observations align with the lensing constraint, with the DMO simulation showing no matches. This indicates that the SDSSJ0946+1006 subhalo is extremely rare in CDM. Furthermore, the few matching subhalos exhibit stellar masses exceeding the expected upper limit, intensifying the discrepancy with CDM.

2.3.4 Mismatch with CDM Predictions

The subhalo is very difficult to fit with CDM predictions, as depicted in Fig. 2.5 and 2.6. Only a few subhalos match the lensing constraints for specific LOS. The stellar mass of nearly all the subhalos from our sample that fit the lensing constraints surpass $10^9 M_\odot$, which, given the luminosity constraint of $L_V < 1.2\times 10^8\, L_\odot$, implies an unusually steep stellar initial mass function (IMF). Typical IMFs suggest a much lower M/L_V ratio [90, 60, 61, 149, 43], and

only the centers of massive galaxies have shown IMFs steep enough to produce the observed $M/L_V > 8M_\odot/L_\odot$ [31].

None of the subhalos in our sample that have the required projected mass also have stellar masses below the upper limit of $2.4 \times 10^8 M_\odot$. The TNG100-1 simulation has been shown to produce stellar masses consistent with Local Group dwarf galaxies, which suggests that subhalos with such high projected masses must have a stellar mass exceeding that of the SDSSJ0946+1006 substructure. Furthermore, most of the subhalos have more stellar than dark matter mass within 1 kpc, hinting at a significant boost by adiabatic contraction. The DMO simulation supports this, as none of the DMO mock observations achieved the required density slope.

In conclusion, the SDSSJ0946+1006 substructure is anomalous in the ΛCDM model. Its projected mass and density slope make it a distinct outlier that is unlikely to be produced in a ΛCDM universe.

2.4 Possible Explanations: from Line-Of-Sight Halos to Dark Matter Physics

Numerous studies propose that lensing perturbations might arise from dark matter halos along the line of sight rather than subhalos of the lensing galaxy [38, 152, 85]. In our case, our analysis suggests that this does not significantly alleviate the tension with CDM. Recursive lensing, where light from a distant galaxy is lensed in stages by closer entities, complicates this scenario, especially when the perturber is behind the primary lens [128]. Ultimately, the dark substructure is likely a perturbing subhalo rather than a line-of-sight halo in the context of CDM.

It is highly unlikely that CDM could produce the SDSSJ0946+1006 substructure, which motivates other dark matter physics. One such model is SIDM (see §1.3 for a detailed discussion of its particle physics). Specifically, gravothermal evolution (as described in §5.2) will drive the core of the halo into core collapse due to the scattering of dark matter particles [8, 3, 103, 47, 106]. Halos in the core collapse phase will experience a rapid increase of the central densities, which in turn would result in higher concentrations and steeper inner log-slopes. Further, as a subhalo, the onset of core collapse can be hastened [103]. SIDM could thus potentially explain the steep inner density slope and high concentration, and as a result, the mass in 1 kpc, of the substructure in SDSSJ0946+1006.

2.5 Conclusion

Using lens models to extract observables from the gravitational lensing galaxy, SDSSJ0946+1006, this work has verified the discovery of a dark substructure as reported by [144], and, for the first time, constrained its concentration, which is found to be inordinately high. Our analysis yields a projected mass within 1 kpc of its center between $(2 - 3.7) \times 10^9 M_\odot$. Comparing our findings with a sample of subhalos from the Illustris TNG100-1 simulations, we observe that less than 1% of the simulated subhalos align with our lensing constraints, even when we account for selection bias which would return a surface density that appears higher than it is due to the LOS. Moreover, all simulated subhalos with a projected mass exceeding $2 \times 10^9 M_\odot$ surpass our upper limit for the observed stellar mass of the substructure. The observed high central dark matter density, concentration, and low luminosity make it a significant deviation from the predictions of ΛCDM.

Chapter 3

Constraining the SIDM Cross Section on Intermediate Scales

The material in this chapter is based the publication [124] on which I am a co-author. For work that was not performed by me but is required for context, I will cite the paper. If I am discussing collective results, I will use "we", "our", etc. Specifically, I wrote the Jeans model section (§2.1) and did the work for and wrote the adiabatic contractions section (§3.3) and the mass-concentration relation section (§3.5). I performed the work for figures 4, 5, 8, and helped the lead author derive the adiabatic contraction form we used in the code. I also wrote the code for the cosmological lensing distances used in the Markov Chain Monte Carlo (MCMC) written by the lead author [124]. I also made figures 13 and 16.

3.1 Introduction

The nature of dark matter, which constitutes approximately 27% of the total mass-energy content of the universe, remains one of the most intriguing and fundamental questions in

cosmology and astrophysics. While the existence of dark matter is well-established through its gravitational effects on visible matter, its particle properties and interactions are still largely unknown. One of the key questions in the study of dark matter is whether it can experience self-interactions, and if so, how these interactions affect the structure and dynamics of astrophysical systems.

This chapter delves into my work in [124], where we investigate SIDM using observational data of relaxed galaxy groups and clusters from [102, 101, 100]. Galaxy groups and clusters are ideal for studying dark matter self-interactions due to their high dark matter content and range of velocities. By analyzing the kinematics of galaxies within these systems, we can infer the properties of the underlying dark matter distribution and place constraints on the self-interaction cross section of dark matter.

We use the Jeans formalism [75], a mathematical framework that describes the equilibrium state of self-gravitating systems, to analyze the observational data. In our analysis, we consider a wider range of systematic effects than in previous work, including adiabatic contraction (AC) and stellar mass-to-light ratio and anisotropy, to robustly constrain the self-interaction cross section. We also explore the velocity-dependence of the self-interaction cross section and its implications for the structure and dynamics of galaxy groups and clusters. We ran a Markov Chain Monte Carlo (MCMC) to fit the group and cluster data, and considered four cases: SIDM with or without AC, and CDM with or without AC.

Our work provides a comprehensive analysis of the self-interactions of dark matter in galaxy groups and clusters. We find that the concentration is systematically shifted to higher values in SIDM compared to CDM. We find a mild preference for a nonzero cross section compared with CDM in both galaxy groups and clusters. We also place the first constraint on SIDM at an intermediate scale between galaxies and massive clusters.

3.2 A Summary of Jeans Modeling

Jeans modeling provides a mathematical framework for describing the equilibrium state of a self-gravitating system, taking into account the gravitational potential, velocity dispersion, and density distribution of the system. The model used to study SIDM halos in this work is based on the time-independent Jeans equation that describes the distribution of matter in a system [73, 75].

In the Jeans model, collisions drive the inner halo towards hydrostatic equilibrium, while the outer region remains effectively collisionless due to its lower density. The boundary between these regions is determined by the radius r_1, where dark matter has scattered on average once per particle per lifetime of the system, according to the rate equation:

$$\rho_{\rm SIDM}(r_1)\,\frac{\langle\sigma v\rangle}{m}\,t_0 = 1\,, \tag{3.1}$$

where $\rho_{\rm SIDM}(r_1)$ is the dark matter density at r_1, $\langle\sigma v\rangle$ is the velocity-averaged SIDM cross section, m is the mass of the dark matter particle, and t_0 is the age of the system. We set the age to 5 Gyr for groups and clusters in our work.

We use a non-singular isothermal profile to model the inner halo experiencing collisions by solving the time-independent Jeans equation:

$$\boldsymbol{\nabla}\left(\sigma_0^2\rho_{\rm iso}(\boldsymbol{r})\right) = -\rho_{\rm iso}(\boldsymbol{r})\boldsymbol{\nabla}\Phi_{\rm tot}(\boldsymbol{r}), \tag{3.2}$$

where we include the dark matter and baryon potential in $\Phi_{\rm tot}$. In our analysis, we assume spherical symmetry and solve Eq. (3.2) for a fixed baryon density. The solution relies on two parameters: the central dark matter density $\rho_0 = \rho_{\rm iso}(0)$ and the one-dimensional velocity dispersion σ_0. We assume that σ_0 is isotropic and constant throughout the system.

We then define the full SIDM profile with the following piece-wise function matched at r_1:

$$\rho_{\rm SIDM}(r) = \begin{cases} \rho_{\rm iso}(r) & r < r_1 \quad \text{(self-interacting)} \\ \rho_{\rm CDM}(r) & r > r_1 \quad \text{(collisionless)} \end{cases} \tag{3.3}$$

where the inner halo is thermalized by self-scattering, and the outer halo profile can be assumed to be collisionless and thus is modeled with a CDM profile. N-body simulations have shown that the NFW profile of Eq. (1.19), which can be parameterized in terms of the virial mass and concentration, (M_{200}, c_{200}), is a good representation of dark matter halos. The presence of baryons falling into the halo, however, can result in a profile cuspier than NFW due to the process of adiabatic contraction (AC). To include AC, the standard method assumes there is an adiabatic invariant $M_{\rm tot}(r)r$, with $M_{\rm tot}(r)$ being the total mass enclosed within r, and that particle orbits are circular [15]. Another approach from [65, 64] involves a modified adiabatic invariant $M_{\rm tot}(\bar{r})r$ that allows for eccentric orbits rather than circular ones. Here, the orbit-averaged radius $\bar{r}$ is given as

$$\bar{r}/r_0 = A_0 \left(r/r_0\right)^w \ , \tag{3.4}$$

with $r_0 = 0.03 r_{200}$. The standard AC prescription [15] is recovered with $A_0 = w = 1$. The modified prescription [65] is retrieved by setting $A_0 = 1.6$, $w = 0.8$. For our MCMCs, we set $A_0 = 1.6$ and allowed w to float between $0.6 - 1.3$. In this study, we explore both a pure NFW profile as well as one that has been modified by AC for the outer halo. The parameters of the Jeans model include the baryon density, the SIDM profile parameters for the inner halo, the parameters for the outer NFW halo, and the matching radius r_1. Allowing for AC, w is an additional parameter.

Lastly, the Jeans model exhibits a two-fold degeneracy, where two values of the cross-section σ/m can yield similar spherically-averaged profiles. This corresponds to core growth or core collapse. In this analysis, we only consider the core-growth solutions.

3.3 Cross sections

This part of the study was led by the lead author, and the MCMC code used was written by the lead author as well [124]. The results from our MCMCs for the self-interaction cross section show that AC tends to shift the cross sections toward larger one compared to pure NFW. While there is a mild preference for a nonzero cross section compared to CDM, a few of the groups (CSWA141, CSWA165, CSWA6) and clusters (MS2137, A963, A2390) preferred cross sections $\sigma/m \leq 0.2\,\mathrm{cm}^2/\mathrm{g}$. These results disfavor constant cross sections of $\geq 1\,\mathrm{cm}^2/\mathrm{g}$ needed to solve small scale issues (see Sec. A.2), and are thus consistent with velocity-dependent SIDM [124].

We determine upper limits on the cross section at the 95% confidence level, which are presented for the case where AC is not considered, as:

$$\begin{aligned} &\sigma/m < 0.9\,\mathrm{cm}^2/\mathrm{g}\ \text{(groups)}, \\ &\sigma/m < 0.28\,\mathrm{cm}^2/\mathrm{g}\ \text{(clusters)}, \end{aligned} \tag{3.5}$$

and when we include AC, we have the following upper limits:

$$\begin{aligned} &\sigma/m < 1.1\,\mathrm{cm}^2/\mathrm{g}\ \text{(groups)}, \\ &\sigma/m < 0.35\,\mathrm{cm}^2/\mathrm{g}\ \text{(clusters)}. \end{aligned} \tag{3.6}$$

We also consider a dark sector model with a dark photon mediating self-interactions, through a repulsive Yukawa potential $V(r) = \alpha' e^{-\mu r}/r$, with μ being the mass of the dark photon and α' the dark fine structure constant. We set the dark matter mass to $m = 15\,\mathrm{GeV}$, and use $\alpha' = 1/137$ and $\mu = 11\,\mathrm{MeV}$ for the dark photon [124]. This model is shown in Fig. 3.1, which was made by the lead author [124]. The solid line in Fig. 3.1 is $\langle\sigma v\rangle/m$ as a function of $\langle v\rangle$, which, including our results and new constraints for group scales, is consistent with a velocity dependence. The yellow-shaded region $1\,\mathrm{cm}^2/\mathrm{g} \leq \sigma/m \leq 100\,\mathrm{cm}^2/\mathrm{g}$ represents the

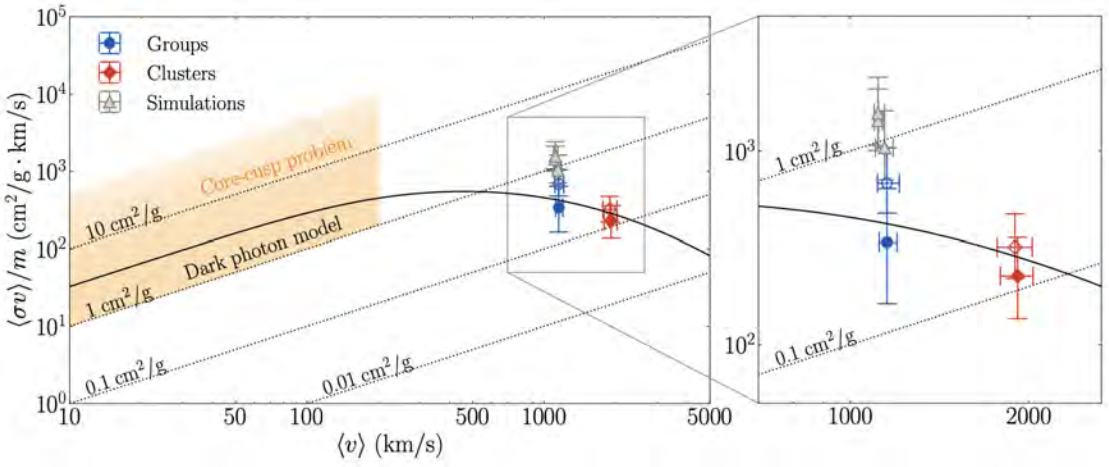

Figure 3.1: The velocity-dependence of self-interactions, $\langle\sigma v\rangle/m$, vs the mean scattering velocity $\langle v\rangle$. The blue and red points represent, respectively, our fits to the galaxy groups and clusters. The closed and open circles are SIDM fits without AC, and with AC, respectively. Gray points are mock SIDM-plus-baryons simulations with $1\,\mathrm{cm}^2/\mathrm{g}$ from [118]. The shaded region represents the space in which SIDM solves the core-cusp problem. The solid line represents $\langle\sigma v\rangle/m$ for a dark matter mass of 15 GeV and dark photon 11 MeV. [124]

region in which small-scale problems are solved [75]. In that region, self-interactions behave like a contact interaction with a constant cross section $\sim 3\,\mathrm{cm}^2/\mathrm{g}$, and then the cross-section falls with increasing mean velocity, consistent with a velocity dependent cross section.

3.4 Adiabatic Contractions

We extended the Jeans model to account for adiabatic contraction (AC) in this study for the groups and clusters. The profile is represented by a modified NFW profile in the outer halo beyond r_1 where dark matter particles are effectively collisionless. We explore the impact of AC on SIDM profiles and on stellar kinematics and lensing observables. Three prescriptions were considered: standard adiabatic contraction (SAC) [15], modified adiabatic contraction (MAC) [65], and pure NFW profiles without AC [97].

I found that AC has a noticeable effect on SIDM halos only for small cross sections, when r_1 is comparable to the extent at which baryon effects in the halo are strong. To illustrate

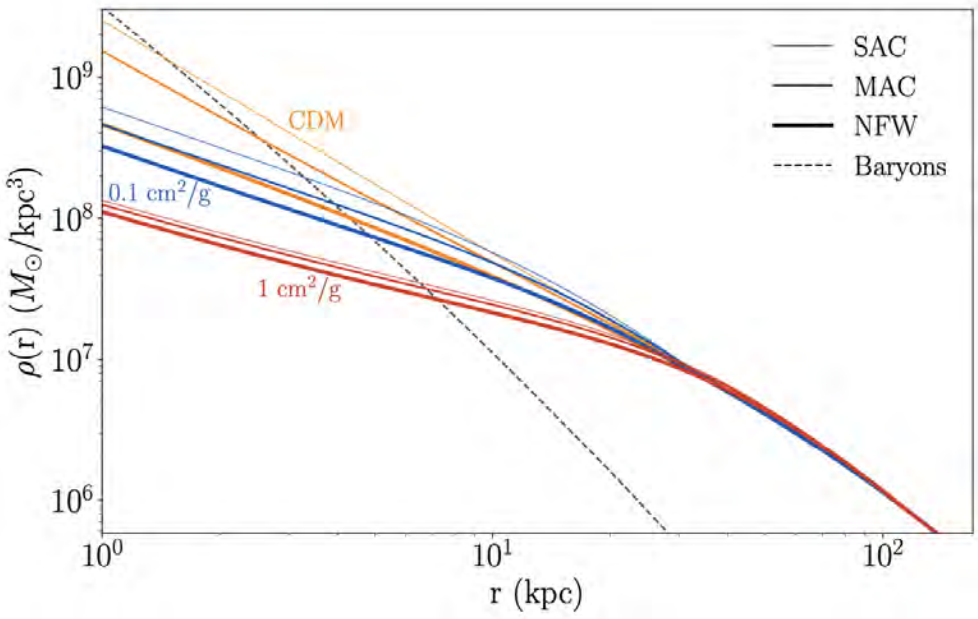

Figure 3.2: Density profiles for the group CSWA6. A set of curves for CDM (yellow), and SIDM with $0.1\,\mathrm{cm}^2/\mathrm{g}$ (blue) and $1\,\mathrm{cm}^2/\mathrm{g}$ (red) for SAC, MAC, and pure NFW. As also include the baryon profile. We use the fixed parameters $M_{200} = 10^{13.84}\,M_\odot$, $c = 10^{0.88}$, and $\Upsilon_* = 10^{0.48}$.

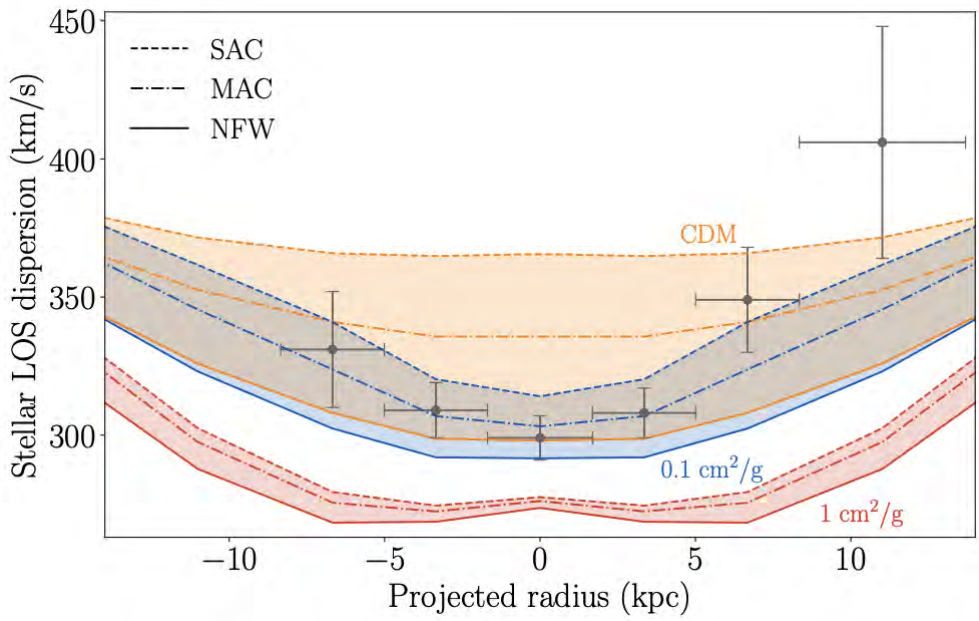

Figure 3.3: Group CSWA6 stellar velocity dispersion for CDM and SIDM for the same AC prescriptions and mass and concentration parameters as in Fig. 3.2.

the effect, I used the example of the galaxy group CSWA6 [100] in Fig. 3.2, fixing the mass, concentration, and stellar mass-to-light ratio.

As expected, for CDM, AC produces halos with steeper inner slopes and increased central densities compared to NFW profiles without AC. For SIDM, the effect of AC is more appreciable for a cross section of $0.1\,\mathrm{cm}^2/\mathrm{g}$ which has $r_1 \approx 30\,\mathrm{kpc}$, than for $1\,\mathrm{cm}^2/\mathrm{g}$ which $r_1 \approx 115\,\mathrm{kpc}$. This is because when the AC profile is matched onto the isothermal one so far out in the halo, the effect of the baryons (which dominate near the center) is nullified. I also found that AC heavily affects the velocity dispersions for smaller cross sections, which we demonstrate in Fig. 3.3, where we use the same parameters as in Fig. 3.2. I also found similarly that the convergence (defined in Eq. (A.8) in § A.1) is similarly affected, such that SAC increases the convergence the most, and MAC by a slightly smaller amount, compared to pure NFW. Smaller cross sections increase the spread between SAC, MAC, and NFW. This is a result of the fact that higher cross sections tend to wash out the effects of AC as r_1 is larger and thus encompasses the region in which the halo is affected by AC, which is why CDM is affected by AC the most.

3.5 Stellar mass-to-light ratio and Anisotropy

This part of the study was led by the lead author [124]. Modeling the stellar component of groups and clusters can be difficult because of the uncertainties in the initial mass function in stellar population synthesis (SPS). This makes the stellar mass-to-light ratio normalization $\Upsilon_\star$ difficult to pin down. Additionally, the stellar velocity dispersion anisotropy, β, is also fraught with uncertainty due to the limitation of our view of the universe being a 2-dimensional projection, thus only allowing us to measure objects along the line of sight. We thus allowed these parameters to vary in the MCMC placing weak priors on each

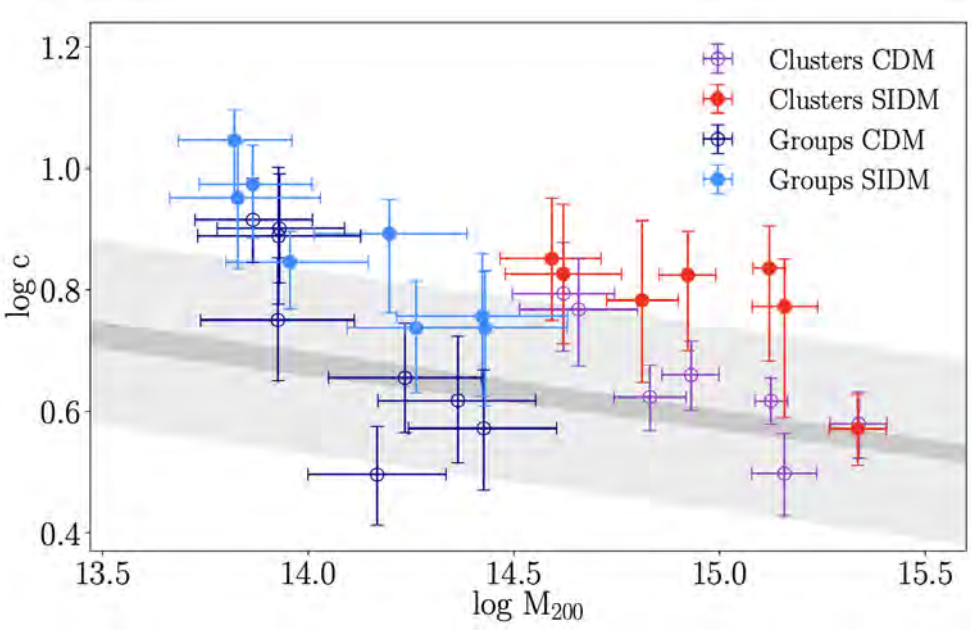

Figure 3.4: M_{200} versus c for the groups and clusters in our analysis for the cases of SIDM and CDM (without AC). The dark gray band is the median MCR from CDM-only simulations for $0.19 < z < 0.45$. The light gray band is a spread of ± 0.15 dex in the concentration.

quantity [124]. We found that $\Upsilon_\star/\Upsilon_\star^{\rm SPS}$ is larger for SIDM than for CDM. For β, there was no preferred range for groups, but clusters prefer a slightly negative β.

3.6 Mass-concentration relation

The mass-concentration relation (MCR) is a fundamental concept in cosmology that describes the relationship between the mass of a dark matter halo and its concentration [147, 23, 41, 40, 46]. The concentration parameter is a measure of how centrally concentrated the mass of a halo is, and it is typically defined as the ratio of the virial radius of the halo to the scale radius of the halo's density profile, $c = \frac{r_{200}}{r_s}$. The virial mass of a dark matter halo, M_{200}, is a measure of the total mass of the halo within its virial radius. The virial radius is the radius within which the average density of the halo is 200 times the critical density of the universe, $\rho_{\rm crit} = \frac{3H^2(z)}{8\pi G}$, at some redshift. We also used the concentration-mass

relation of [46]. The MCR is very important in the study of dark matter halos as it can tell us about its formation history, for example halos tend to be more concentrated if they have not experienced mergers in their recent history. In SIDM, interactions redistribute mass in a halo, which can thus affect the concentration. In this work, I examined how self-interactions (without AC) affect the MCR.

For SIDM, the outer halo beyond r_1 is expected to be nearly collisionless, thus the profile should coincide with the corresponding CDM profile in the absence of collisions. Thus we may expect that the values of (M_{200}, c) that we obtain from our Jeans modeling should generally obey the MCR. However, I found that the results from the MCMC fits for SIDM show a systematic shift towards higher concentrations compared to the median MCR; see Fig. 3.4. The CDM fits were in better agreement with the median MCR, as expected.

The central density of the halos in our study is constrained by observations. A higher concentration increases the central density, while collisions generally decrease it. Thus it is reasonable that turning on self-interactions would result in an increase in the concentration for a fixed central density as a result. It is also possible that this shift towards higher concentrations in SIDM fits could be representative of a bias in the Jeans model. Additionally, the groups and clusters in our work are all strong lenses, meaning they are susceptible to selection bias, where the orientation of a halo along our line of sight results in higher concentrations [129]. It is also worth noting that the MCR is a CDM-based prediction and may not be applicable to SIDM halos.

3.7 Comparison to simulations

We compare our methods to hydrodynamical simulations by [118]. This part of the study was lead by a coauthor [124]. We re-simulate two clusters from the Cluster-EAGLE (CE)

project [6, 11], the first to include baryons and self-interactions on cluster scales, with a self-interaction cross-section per unit mass of $\sigma/m = 1\,\mathrm{cm}^2/\mathrm{g}$ [124], and make mock observables from them and fit them with our Jeans model to extract the cross section.

We consider three realizations of the data sample, each for a different slit angle for the stellar kinematics. We find that the Jeans model gives robust predictions for the cross-section, independent of the exact values of M_{200}. We obtain values of σ/m in the range of 1–$1.7\,\mathrm{cm}^2/\mathrm{g}$, depending on various systematic assumptions, which is close to the actual cross section and thus confirms the Jeans model is robust.

I also looked at the MCR for the simulated clusters. I compared the values of (M_{200}, c) from our fits to the true values obtained from the CDM-only simulations for CE-05 and CE-12, using the equation

$$\log\left(h(z)\,M_{200}/M_\odot\right) = 13.98 + 2.75\log\left(\frac{\sigma_{\mathrm{LOS}}}{500\,\mathrm{km/s}}\right)\,, \tag{3.7}$$

where the dimensionless Hubble parameter is $h(z) = \frac{H(z)}{H_0}$. The results showed that the fits picked out larger values of c and smaller values of M_{200} compared to the true values. Because using priors on M_{200} from our fits for CE-12 returned large deviations from the true value, we also used the true value of M_{200} and ran the same analysis. The results for CE-05 did not change by much, while those for CE-12 shifted closer to the true M_{200}. These effects can clearly be seen in Fig. 3.5. However, I still observed a trend toward higher concentrations and smaller values of M_{200}, which was also found in the analysis of group and cluster observations. The effect of the choice of priors for M_{200} on the joint fit for σ/m was negligible, so that these results remain the same.

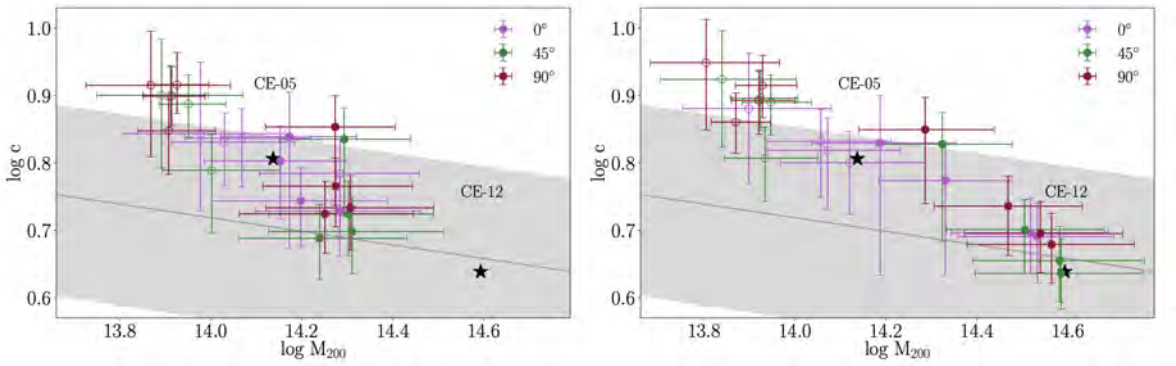

Figure 3.5: Fitted (M_{200}, c) values for the simulated clusters. The left panel centers a prior on the M_{200} derived from galaxy kinematics, while the right panel corresponds to a prior centered on the true M_{200}. The band is the MCR for $z = 0$ with a ± 0.15 dex spread in c.

3.8 Conclusion

In this work, we examined a set of strong lensing systems, drawing from the galaxy group samples of [100] and the massive clusters in [102, 101], with mass ranges spanning 4×10^{13} to $2 \times 10^{15}\, M_\odot$. We placed the first constraint on σ/m at an intermediate scale, bridging the gap between galaxies and massive clusters. Furthermore, we re-evaluated the cross-section constraint for massive clusters in [75]. By incorporating a broader range of systematic uncertainties, such as the unknown stellar mass-to-light ratio $\Upsilon_\star$, velocity dispersion anisotropy β, and the potential effect of adiabatic contraction on SIDM halos, our work improved prior constraints and made them more robust.

Our findings indicate a subtle preference for a non-zero cross-section compared to CDM for both groups and clusters. We derived constraints on the cross section, considering scenarios both with and without AC. Intriguingly, including AC systematically shifts the cross section to higher σ/m values. Our results for galaxy groups offer a new data point for the cross section as a function of velocity. Our findings for clusters are consistent with previous studies with values $\sim 0.1\,\mathrm{cm}^2/\mathrm{g}$ [75, 48]. Our work supports a velocity-dependent cross-section for

SIDM, that decreases as scattering velocity increases. This conclusion is consistent with expectations in well-founded SIDM models from a particle physics perspective.

To further validate our Jeans model, we used mock observations from high-resolution hydrodynamical SIDM cluster simulations with $\sigma/m = 1\,\mathrm{cm}^2/\mathrm{g}$ [118]. Our analysis yielded central values ranging in $1.1 - 1.7\,\mathrm{cm}^2/\mathrm{g}$. Though a little higher than the input cross section, the fact that our model returned a value close to the input value is encouraging that it is performing as it should.

Our results show that AC pushes the cross section to slightly larger values than CDM without AC. We also see that SIDM concentrations are higher than the CDM prediction, a result that comes from the model compensating for the interactions while holding the central density constant. Our results contribute to the growing body of evidence supporting a velocity-dependent SIDM cross-section that decreases with increasing scattering velocity.

Chapter 4

Gravothermal Collapse of Velocity Dependent SIDM Halos in the LMFP Regime

This chapter is based on the work in [106] to which I contributed significantly. The results are based on a gravothermal code to which I have contributed with maintaining and editing the code, and supplied some of the cross-section computations that have been incorporated into the code. In this work, the numerical work and results were performed by me, and the theoretical derivations were done by the lead author. I made all the figures which are all based on the numerical results I obtained (some figures in the Appendix include comparisons between the numerical work and the theoretical predictions of [106]), and contributed to writing the paper, but the bulk of it was written by the lead author [106]. To distinguish work that is not mine but required for context, I cite the paper and/or use "we" and "our".

4.1 Introduction

A particular area of interest in studying SIDM halos to learn about the particle physics of dark matter is the phenomenon of gravothermal evolution, in which scattering enables heat transfer between the inner and outer parts of the halo and drives the halo into core collapse [88]. SIDM was initially introduced to explain small scale problems observed in low mass halos [134] compared to CDM simulations [56, 94, 36, 104, 125, 62] such as the core-cusp problem by alleviating central densities via scattering of dark matter particles (see Appendix A.2 for more detail on the small scale problems). Given the observed diversity in rotation curves of low-surface-brightness galaxies, the core collapse stage of SIDM halos is particularly intriguing as it offers a new range of density profiles that exhibit central densities much higher than CDM, allowing for a more diverse set of halo profiles that better match observations [105, 72, 117].

In this chapter, I will describe our pivotal work in [106], where we focus on the gravothermal evolution of isolated SIDM halos, specifically in the LMFP regime where dark matter particles are able to make many orbits before scattering. We employ the spherically symmetric gravothermal equations and, for the first time, generalize our work to include velocity-dependent scattering cross sections.

We derive a new set of self-similar solutions in which the scattering cross-section is velocity dependent. This is a first of its kind, as previous works [8] considered velocity-independent cross-sections. These self-similar solutions offer an analytical framework that aids in understanding our numerical results and the gravothermal evolution of SIDM halos. We identify an approximate universality in the temporal evolution in the LMFP. These tools enable the mapping of velocity-dependent models onto those that are velocity-independent. The mapping is achieved through the scattering timescale, determined at core formation,

which is when the halo reaches its lowest central density. We find a form for the collapse time in which the velocity dependence is included.

Most of our halos begin their evolution in the LMFP regime and spend the bulk of their time here, and fall into the SMFP at the very late stages of the collapse. The predicted collapse time of a halo is fully determined by the scattering time-scale, and our numerical results show that there is only a small scatter due to the velocity dependence. Thus, given the mass and particle physics, we can effectively scale out the particle physics with minimal scatter and fully determine the entire evolution through its collapse time of any given halo.

Our work provides newly derived equations in the LMFP gravothermal evolution of SIDM halos with velocity-dependent cross-sections. The discovery of universality in temporal evolution and the derivation of new self-similar solutions are significant milestones that provide useful tools for research, allowing one to fully analytically characterize the evolution of any halo in the LMFP.

4.2 Gravothermal Evolution

The behavior of an isolated spherically symmetric, virialized halo can be described by the following gravothermal equations [88, 8, 103, 50]:

$$\begin{aligned} &\frac{\partial M}{\partial r} = 4\pi r^2 \rho \ , \quad \frac{\partial(\rho v^2)}{\partial r} = -\frac{GM\rho}{r^2} \ , \quad \frac{L}{4\pi r^2} = -\kappa \frac{\partial T}{\partial r} \ , \\ &\frac{\partial L}{\partial r} = -4\pi r^2 \rho v^2 \left(\frac{\partial}{\partial t}\right)_M \log\left(\frac{v^3}{\rho}\right), \end{aligned} \tag{4.1}$$

where ρ, M, L, and v represent the halo's density, the enclosed mass, luminosity, and one-dimensional velocity dispersion, respectively, and the dark matter temperature is given by $T_{\rm dm} = m_{\rm dm} v^2$, where $m_{\rm dm}$ is the dark matter particle mass. The heat conductivity term,

κ, which relates the luminosity to the temperature gradient, is where the particle physics information lies.

4.2.1 Heat Conductivity with Velocity Dependence

The conductivities for the LMFP and SMFP have unique forms, and we interpolate between them as follows [8]:

$$\frac{1}{\kappa} = \frac{1}{\kappa_{\text{LMFP}}} + \frac{1}{\kappa_{\text{SMFP}}}. \tag{4.2}$$

We use a differential cross-section that converges to a constant if velocities are significantly smaller than a velocity scale, $v \ll w$. This allows us to account for both velocity-dependent and constant cross sections. The form is as follows:

$$\lim_{v_{\text{rel}} \to 0} \frac{d\sigma(v_{\text{rel}})}{d\Omega} = \lim_{w \to \infty} \frac{d\sigma(v_{\text{rel}})}{d\Omega} = \frac{\sigma_0}{4\pi}, \tag{4.3}$$

where $v_{\text{rel}} = |\boldsymbol{v}_1 - \boldsymbol{v}_2|$ denotes the relative velocity between the colliding particles and σ_0 is a normalization prefactor [106].

The thermal properties of an SIDM halo in the SMFP do not depend on halo size, allowing for the thermal conductivity to be derived perturbatively via the Chapman-Enskog expansion [110, 25]. For hard-sphere scattering, the conductivity is given by $\kappa = 3bv/2\sigma_0$ where $b = 25\sqrt{\pi}/32$ (see, for example, [8, 83, 103]).

Generalizing for a cross-section that includes velocity dependence, the lead author [106] derived a new form for the conductivity that approaches $\kappa = 3bv/2\sigma_0$ in the limit where

$v \ll w$:

$$\kappa_{\rm SMFP} = \frac{3}{2}\frac{bv}{\sigma_0}\frac{1}{K_5} \quad , \quad K_p = \frac{\langle \sigma_{\rm visc} v_{\rm rel}^p \rangle}{\lim_{w\to\infty}\langle \sigma_{\rm visc} v_{\rm rel}^p \rangle}, \tag{4.4}$$

where we choose $p = 5$ in this work[1], and $\sigma_{\rm visc} = \int d\sigma \sin^2\theta$, and $\langle\cdot\rangle$ denotes the thermal average over velocities with a 3D Maxwell-Boltzmann distribution.

In contrast to the SMFP, the LMFP does depend on the halo size[2]. But the size of a halo is arbitrary and depends on definitions, since there is not a sharp cut-off where a halo "ends". Given this complication, definitions of the conductivity in the LMFP depend on N-body simulations. The derived conductivity is $\kappa = 3aC\sigma_0 v n^2 H^2/2$, where $a = 4/\sqrt{\pi}$ and $H = v/\sqrt{4\pi G\rho}$ is the Jeans scale. The value of C is calibrated to simulations [8, 83, 50, 88]. We adopt $C = 0.6$ as found in [50].

The lead author of our work in [106] used a similar rationale to that used in the derivation of the SMFP conductivity with a velocity dependence, leading to the following form for the LMFP heat conductivity:

$$\kappa_{\rm LMFP} = \frac{3aC}{8\pi G}\frac{\sigma_0}{m_{\rm dm}^2}\rho v^3 K_3, \tag{4.5}$$

where K_3 is defined in Eq. (4.4) for $p = 3$. The form allows for easy replacement of our averaging (which is $\langle\sigma_{\rm visc} v^3\rangle$) with any other form.

[1] We select $p = 5$ to reflect the cross section dependence given in $\kappa_{\rm SMFP} = F(v)\langle\sigma_{\rm visc} v_{\rm rel}^5\rangle^{-1}$, as given in problem 10 of §10 in Ch. 1 of [110].

[2] From the kinetic theory of gases, we know the LMFP of a gas is defined by the volume of the box the gas is in [25].

4.2.2 Long and Short Mean Free Path Regimes

Gravothermal evolution affects the core (central region) and outer halo differently. In this work, we delineate the core via $\rho(r_{\rm core}) = \rho_c/2$. As the core collapses, self-interactions transport heat and mass to the outer halo while its temperature and density shoot up rapidly. Because its rate of thermal evolution is very slow, the outer halo acts as a heat sink, while the core continues to contract and heat up.

The LMFP is the focus of this work. In the LMFP, dark matter particles are sparse enough to complete multiple orbits between collisions. The outer halo is almost always in this state, while the core may not be; for example, very large cross-sections can cause the core to begin in the SMFP. For the halos in this work, the cores generally evolve in the LMFP regime for the majority of the time. As mentioned above, the core transfers heat and mass to the outer halo which further cause the halo to contract and become rapidly denser and hotter, ultimately driving the core into the SMFP. We define the transition between the LMFP to the SMFP as the point where the conductivities are equal.

In the SMFP regime, particle collisions are frequent due to high density, which results in shielding heat and mass transfer. During this phase, the core's temperature and density escalate rapidly. The timescales for LMFP and SMFP evolution are markedly different; while most of the evolution occurs in the LMFP regime, the transition to the SMFP regime happens swiftly. At this stage, the core enters a phase of constant thermal energy, where the log-slope of central density relative to central velocity stabilizes over time, approaching a value of $\gamma = 10$. During this phase, the core's temperature and density escalate rapidly. However, the SMFP regime is omitted in this work, and is the focus of my work in Chapter 5.

4.2.3 Numerical Techniques for Gravothermal Equations

To solve the gravothermal equations, we start with an initial NFW profile, assuming that dark matter self-interactions are minimal during the formation of the halo. This allows the halo to initially evolve in the LMFP.

We employ numerical methods, following established works [112, 103], to solve the dimensionless form of the gravothermal equations in Eq. (4.1):

$$\begin{aligned}
&\frac{\partial \tilde{M}}{\partial \tilde{r}} = \tilde{r}^2 \tilde{\rho} \ , \ \frac{\partial (\tilde{\rho}\tilde{v}^2)}{\partial \tilde{r}} = -\frac{\tilde{M}\tilde{\rho}}{\tilde{r}^2} \ , \ \tilde{L} = -\tilde{r}^2 \tilde{\kappa} \frac{\partial \tilde{v}^2}{\partial \tilde{r}} \ , \\
&\frac{\partial \tilde{L}}{\partial \tilde{r}} = -\tilde{r}^2 \tilde{\rho} \tilde{v}^2 \left(\frac{\partial}{\partial \tilde{t}} \right)_{\tilde{M}} \log \left(\frac{\tilde{v}^3}{\tilde{\rho}} \right),
\end{aligned} \tag{4.6}$$

where the physical quantities $x = \{\rho, v, M, L, r, t, \kappa\}$ are scaled as $\tilde{x} \equiv x/x_N$. These scales are as follows:

$$\begin{aligned}
&\rho_N = \frac{M_N}{4\pi r_N^3} \ , \ v_N^2 = \frac{GM_N}{r_N} \ , \ L_N = \frac{M_N v_N^2}{t_N} \ , \\
&\kappa_N = \frac{M_N}{4\pi m_{\rm dm} r_N t_N},
\end{aligned} \tag{4.7}$$

where the subscript N denotes a scale quantity. The scattering timescale is:

$$t_N = \frac{2}{3aC} \left(\rho_N \frac{\sigma_0}{m_{\rm dm}} v_N K_3 \left(\frac{v_N}{w} \right) \right)^{-1}. \tag{4.8}$$

We can now write the dimensionless conductivity as

$$\tilde{\kappa} = \tilde{\rho}\tilde{v}^3 \tilde{K}_3 \left[1 + \hat{\sigma}^2 \tilde{\rho} \tilde{v}^2 \tilde{K}_3 \tilde{K}_5 \right]^{-1} \ , \ \tilde{K}_p = \frac{K_p(\tilde{v}/\hat{w})}{K_p(1/\hat{w})}, \tag{4.9}$$

where

$$\hat{\sigma}^2 = \frac{aC}{b} K_5\left(\frac{1}{\hat{w}}\right) K_5^{(2)}\left(\frac{1}{\hat{w}}\right) \frac{\rho_N}{4\pi G}\left(v_N \frac{\sigma_0}{m_{\rm dm}}\right)^2, \qquad \hat{w} = \frac{w}{v_N}. \tag{4.10}$$

The two dimensionless parameters, $\hat{\sigma}$ and $\hat{w}$, fully specify these equations. We also choose to express the cross-section in terms of its velocity dependence slope, n, defined through the LMFP heat conductivity equation as

$$n = -\frac{d\log K}{d\log v_N}. \tag{4.11}$$

We focus on Yukawa interactions between SIDM particles for our numerical calculations. The self-interaction differential cross-section is formulated under the Born approximation:

$$\frac{d\sigma}{d\Omega} = \frac{\sigma_0}{4\pi}\left(1 + \frac{v_{\rm rel}^2}{w^2}\sin^2\frac{\theta}{2}\right)^{-2}, \tag{4.12}$$

where we use K_p as a function of v/w.

Testing Numerical Convergence: We follow [112, 103] and numerically solve the dimensionless gravothermal equations in Eq. (4.6) whilst fixing the mass shells. We follow [103] to numerically calculate the heat conduction by taking small time steps with $\epsilon_t = 10^{-4}$ to ensure the density remains nearly constant. I set 400 logarithmically-spaced shells for the radius, holding the mass in each shell constant. We also conducted tests with 800 shells to confirm that our results have converged, and found that the minimum density changes by only 0.016%, the dispersion at minimum density by 0.023% and the collapse time by 0.1%. Our initial 400 shells are thus sufficient for this work.

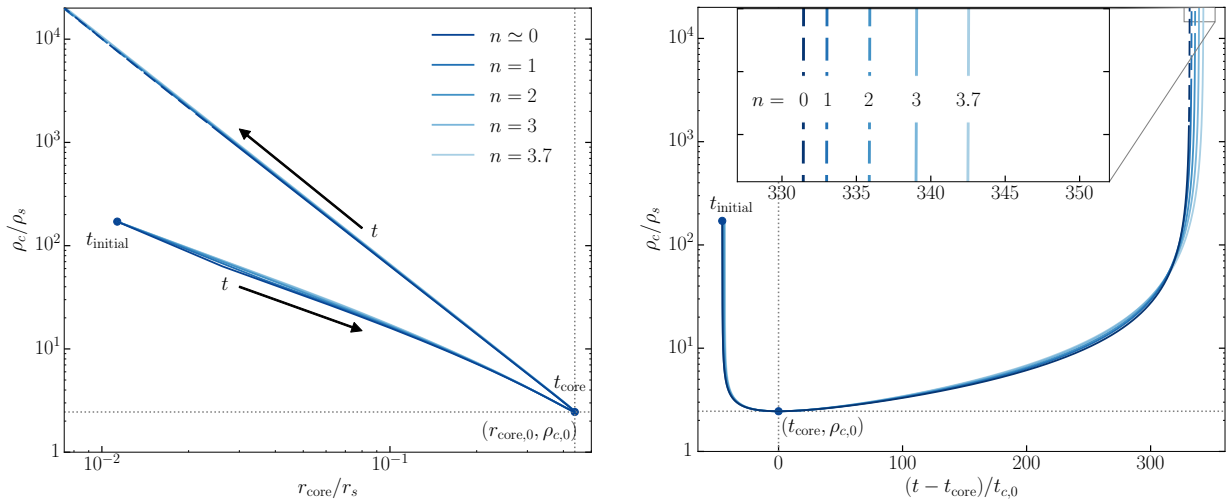

Figure 4.1: *(Left)* The central density as a function of the core radius, normalized by the NFW parameters ρ_s, r_s. The initial time step in our gravothermal code is denoted by $t_{\rm initial}$, while $t_{\rm core}$ is the time of core formation, when the central density hits a minimum. The flow of time (shown with arrows) reveals a stark increase in central density and corresponding shrinking of core radius after core formation. *(Right)* ρ_c/ρ_s with respect to shifted time, normalized by $t_{c,0}$ (Eq. (4.8)). We include an inset to make clear how the collapse times vary for each halo. When the halo transitions from LMFP to SMFP, we use dashed lines. Models in both panels are the same and are the main models of the paper (see the parameters in runs $1-5$ of Table 4.1).

4.3 Universal Evolution for Velocity-Dependent SIDM Halos

For the case of contact interactions (the limit $w \to \infty$ in Eq. (4.10)), the gravothermal equations are characterized by only one parameter, $\hat{\sigma}$. Then, for a constant cross-section, the LMFP universality of the gravothermal equations is an obvious result. However, including velocity dependent interactions introduces a new parameter, $\hat{w}$. My numerical results as shown in Figs. 4.1 and 4.2 show us that nevertheless, the LMFP solution is approximately universal with only minimal scatter due to the velocity dependence of the cross-section.

Despite the scatter, all halos converge to the same core radius $r_{\rm core,0}$ (where the core radius is defined via $\rho(r_{\rm core}) = \rho_c/2.$), central density $\rho_{c,0}$, and velocity dispersion $v_{c,0}$ when normalized

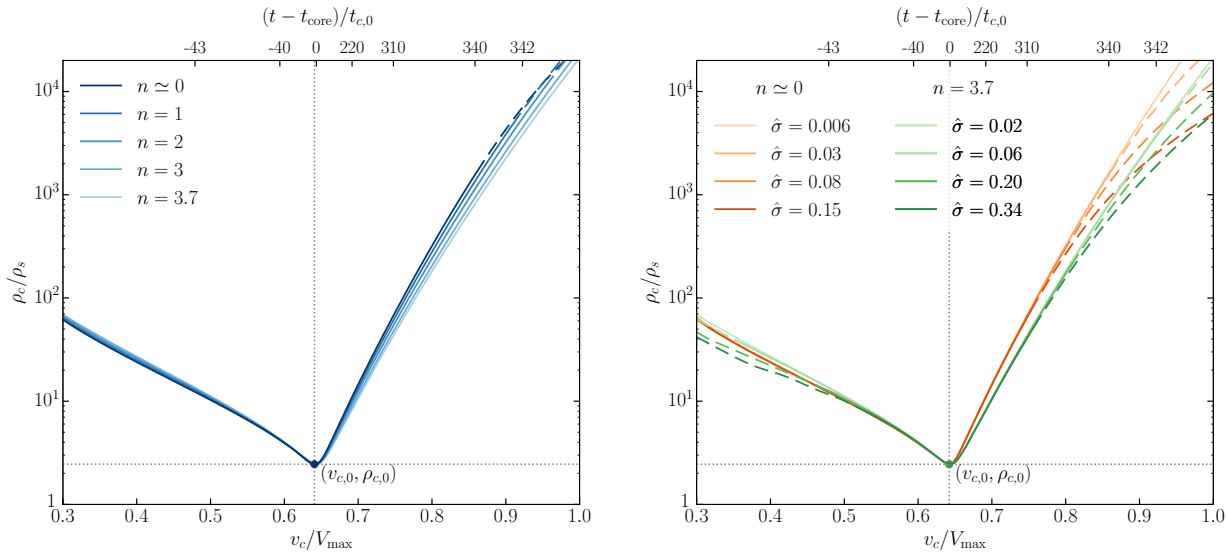

Figure 4.2: *(Left)* ρ_c/ρ_s, versus the central 1D velocity dispersion normalized by $V_{\rm max}$, with each run having $\sigma_{c,0}/m_{\rm dm} \simeq 5\,cm^2/g$ fixed for $n = 0, 1, 2, 3, 3.7$ for the main five models, as in Fig. 4.1. We have used the upper horizontal axis to show the shifted time to highlight the fact that most of the evolution is spent around core formation (for the time axis, we chose Run #5 of Table 4.1). Again, dashed lines indicate the core is in the SMFP. *(Right)* The same as the left panel, except here, we fix $n \simeq 0$ and $n = 3.7$ for various $\hat{\sigma}$ (details listed in Table 4.1).

by the halo NFW parameters, at the time of core formation, $t_{\rm core}$. We find direct relations between the core parameters and NFW parameters of $r_{\rm core,0} \simeq 0.45 r_s$, $\rho_{c,0} \simeq 2.4\rho_s$, and $v_{c,0} \simeq 0.64 V_{\rm max}$, with which all of my numerical results agree. This approximate universality suggests that we can effectively scale out all the particle physics and determine the entire LMFP evolution of any given halo.

Figs. 4.1 and 4.2 also highlight that gravitational evolution occurs in stages in halos, beginning with thermalizing until the halo reaches core formation, followed by a self-similar evolution that proceeds until collapse. My numerical results show that the collapse time occurs at a dimensionless time of $t_{\rm coll}/t_{c,0} \simeq 335$, which is universally consistent across all halos, within a minimal scatter due to the velocity dependence.

Rescaling the central density we obtained as $\rho_{c,0} \simeq 2.4\rho_s$ along with using $C = 0.61$, we [106] find the results agree.

4.4 Self-Similarity of Velocity-Dependent SIDM in the LMFP

In this section, I will outline the self-similar solutions in our work derived by the lead author [106]. The self-similar solutions elucidate key aspects of the LMFP behavior of halos, and the analytic handle allows us to characterize the collapse time.

Rather than using the initial time of our code as $t = 0$, we adopt $t_{\rm core} = 0$ so that the gravothermal evolution begins after core formation, as in [8]. In the LMFP regime, the dimensionless effective conductivity $\tilde{\kappa}$ is given by:

$$\tilde{\kappa}_{\rm eff} = \tilde{\rho}\tilde{v}^{3-n}, \tag{4.13}$$

where n is defined in Eq. (4.11), and Yukawa interactions imply $0 < n < 4$.

Much like [88], our goal is to find a self-similar solution with the following form:

$$\tilde{x}(\tilde{r},\tilde{t}) = \tilde{x}_c(\tilde{t})x_*(r_*) \ \ , \ \ r_* = \frac{\tilde{r}}{\tilde{r}_c(\tilde{t})}, \tag{4.14}$$

subject to the boundary conditions

$$\rho_*(0) = v_*(0) = 1 \ \text{ and } \ L_*(0) = M_*(0) = 0 \tag{4.15}$$

taken at $r = r_* = 0$ with initial condition $\tilde{x}_c(0) = 1$. This leads to relationships between temporal functions:

$$\tilde{M}_c = \tilde{r}_c^3\tilde{\rho}_c \ \ , \ \ \tilde{v}_c^2 = \frac{\tilde{M}_c}{\tilde{r}_c} \ \ , \ \ \tilde{L}_c = \tilde{\rho}_c\tilde{r}_c\tilde{v}_c^{5-n}. \tag{4.16}$$

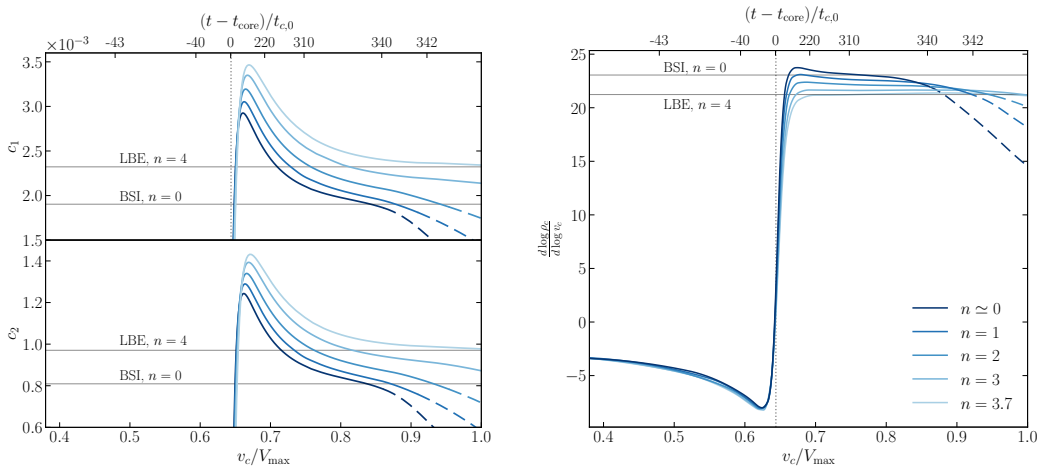

Figure 4.3: *(Left)* SOV constants c_1 and c_2 from Eq. (4.18) vs. $v_c/V_{\rm max}$. Horizontal gray lines are the predictions for $c_{1,2}$, with $c_1 = 2.322 \times 10^{-3}$, $c_2 = 9.704 \times 10^{-4}$ for $n = 4$ [88] and $c_1 = 1.903 \times 10^{-3}$, $c_2 = 8.092 \times 10^{-4}$ for $n = 0$ [8]. *(Right)* Log derivative of the central density vs. $v_c/V_{\rm max}$. Horizontal gray lines are predictions of $\alpha = 2.208$ for $n = 4$ [88] and $\alpha = 2.190$ for $n = 0$ [8] using Eq. (4.22). For both panels: dotted vertical line indicates time of core formation; top horizontal axis shows the shifted time normalized by $t_{c,0}$ (run 5 of Table 4.1 is used for the time in the figures); $\sigma_{c,0}/m_{\rm dm} \simeq 5cm^2/g$ is fixed for various n as shown in the legend. $\alpha = 2.192, 2.195, 2.199, 2.204, 2.207$ for $n = 0, 1, 2, 3, 3.7$ respectively.

Using separation of variables (SOV) and defining a new time variable $\tau_c(\tilde{t}) = t_{c,0}\tilde{\tau}_c = t_{c,0}\frac{\tilde{M}_c\tilde{v}_c^2}{\tilde{L}_c}$, the spatial forms can be recast as follows:

$$\frac{\partial M_*}{\partial r_*} = r_*^2\rho_* \;\;,\;\; \frac{\partial}{\partial r_*}\left(\rho_* v_*^2\right) = -\frac{M_*}{r_*^2}\rho_* \;\;,\;\; L_* = -r_*^2\rho_* v_*^{3-n}\frac{\partial v_*^2}{\partial r_*}$$
$$\frac{\partial L_*}{\partial r_*} = r_*^2\rho_* v_*^2\left[c_1 - c_2\frac{\partial\log\left(v_*^3/\rho_*\right)}{\partial\log M_*}\right] \;, \tag{4.17}$$

with our SOV constants being c_1 and c_2:

$$c_1 = -\tau_c\frac{\partial}{\partial t}\log\left(\frac{v_c^3}{\rho_c}\right) \;\;,\;\; c_2 = -\tau_c\frac{\partial}{\partial t}\log M_c\,. \tag{4.18}$$

While analogous to [8, 88], these are generalized to velocity-dependent interactions. And looking at Fig. 4.3, my numerical results show that our work agrees with [8] for $n = 0$, and [88] for $n = 4$, which are shown by the labeled horizontal lines in both panels.

4.4.1 Predictive Power and Validation

Here, I compare the self-similar derivations [106] against the numerical results I obtained. One important condition to ensure valid self-similar results from [88] requires that the density is time independent and scales as the following from the center of the halo, $r = 0$ all the way out to $r \to \infty$:

$$\frac{d\log\tilde{\rho}_c}{d\log\tilde{r}_c} = \lim_{r_*\to\infty}\frac{d\log\rho_*}{d\log r_*} = -\alpha, \tag{4.19}$$

where α must be in the range as per $[2, 2.5]$ [88]. This implies that $\tilde{\rho}_c = \tilde{r}_c^{-\alpha}$. We thus obtain the following central parameters using this and Eq. (4.16):

$$\tilde{\rho}_c = \tilde{r}_c^{-\alpha} \;\;,\;\; \tilde{M}_c = \tilde{r}_c^{3-\alpha}\;,\; \tilde{v}_c^2 = \tilde{r}_c^{2-\alpha}\;,\; \tilde{\tau}_c = \tilde{r}_c^{2+(n-3)\frac{2-\alpha}{2}}. \tag{4.20}$$

With Eq. (4.20) and Eq. (4.18), we find

$$\alpha = 6\frac{c_2 - c_1}{c_2 - 2c_1}. \tag{4.21}$$

Finally, we come to the following relation

$$\frac{d\log\tilde{\rho}_c}{d\log\tilde{v}_c} = \frac{2\alpha}{\alpha - 2}\,, \tag{4.22}$$

which I plot in the right panel of Fig. 4.3 using the form and my numerical results. Similarly to Fig. 4.2, the lines reach a constant at core formation, with a small scatter due to n. The horizontal gray lines underscore that our analytic forms plotted with my numerical results agree with the results of [88] ($n = 4$) and [8] ($n = 0$).

The collapse time was also analytically found [106] to be

$$\tilde{t}_{\rm coll} = \frac{1}{c_1}\frac{6-\alpha}{(3\alpha-2)-n(\alpha-2)}\,. \tag{4.23}$$

While the expression in Eq. (4.23) does not agree with my numerical results for the collapse times which I have shown in Fig. 4.1, it is a small discrepancy that likely stems from the fact that, although our results approximately agree with [88] and [8], the c_1 and α I show in Fig. 4.3 do not actually reach a constant value before the core falls into the SMFP. For example, Eq. (4.23) gives collapse times of $\tilde{t}_{\rm coll} \simeq 430$, while my numerical results yield $\tilde{t}_{\rm coll} \simeq 335$. For a more in-depth discussion on the validity of the LMFP self-similar predictions and how my numerical results differ in magnitude as well as behavior from our analytic results [106], see Appendix 4.A.

Some important analytical forms for parameters at the LMFP to SMFP transition were obtained in this work by [106], which I use in my first-author work in Ch. 5. They come from defining the time when $\kappa_{\rm LMFP} \simeq \kappa_{\rm SMFP}$ in the center of the halo as $\tilde{t}_{c,\rm LS}$. We end up with an important set of definitions:

$$1 \simeq \hat{\sigma}^2\tilde{\rho}\tilde{v}^2\tilde{K}_3\tilde{K}_5 \simeq \hat{\sigma}^2(\tilde{v}_{c,\rm LS})^{2\delta} \quad , \quad \tilde{v}_{c,\rm LS} = \hat{\sigma}^{-1/\delta} \quad , \quad \delta = 1 - \bar{n} + \frac{\alpha}{\alpha-2} \tag{4.24}$$

where $2\bar{n} = -\left.\frac{d\log \tilde{K}_3\tilde{K}_5}{d\log\tilde{v}}\right|_{\tilde{v}=1}$. For run 1 in Table 4.1, this gives $v_{\rm LS} \simeq 0.85 V_{\rm max}$, which agrees well with my numerical results, as I show in Fig. 4.4.

An interesting find from my numerical results shown in the right panel of Fig. 4.4 is that, in dimensionless time, larger $\hat{\sigma}$ results in a slightly delayed collapse time.

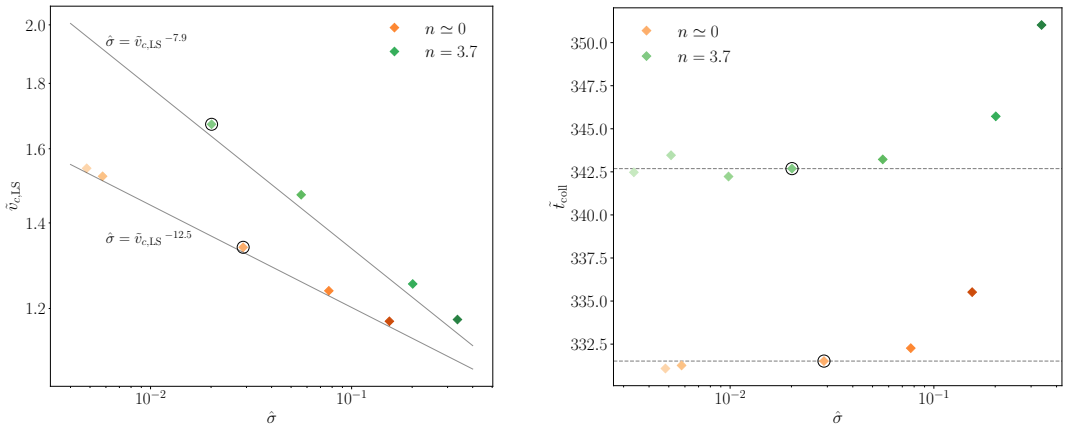

Figure 4.4: *(Left)* The central velocity dispersion at the LMFP to SMFP transition, normalized by $v_{c,0}$, with respect to $\hat{\sigma}$ for halos in our models with $n \simeq 0$ and $n = 3.7$. The predicted scale in Eq. (4.24) is plotted as solid gray lines. *(Right)* The collapse time, $\tilde{t}_{\mathrm{coll}}$, vs. $\hat{\sigma}$ for $n \simeq 0$ and $n = 3.7$. Dotted gray lines are the $\tilde{t}_{\mathrm{coll}}$ shown in Fig. 4.1. Collapse times become delayed for larger $\hat{\sigma}$. Circled diamonds are the models shown in the main text. For $n = 3.7$, points left of the circled diamond are halos that do not reach SMFP, thus are not shown in the left panel.

4.5 Discussion and Conclusion

In this study, we examined velocity-dependent self interactions of SIDM halos undergoing gravothermal evolution in the LMFP regime and found an approximate universality. This universality applies, for the first time, to generalized SIDM models with velocity dependence, and allows a mapping between velocity-dependent and velocity-independent models. We find that NFW halos reach core formation, the point at which the core radius is a maximum, at $r_{\mathrm{core},0} \approx 0.45 r_s$, $\rho_{\mathrm{c},0} \approx 2.4\rho_s$ and $v_{\mathrm{c},0} \approx 0.64 V_{\mathrm{max}}$. My numerical results show that all halos will eventually undergo core collapse and be driven into the SMFP regime. Our results are for generic cross-section models and can be recalculated for other models beyond the Yukawa interaction considered here. We demonstrate that the self-similar solutions in the LMFP regime apply for a broad range of velocity-dependent cross-sections. These approximations offer valuable insights into my numerical results, such as the core collapse timescale and the evolution of the inner density and dispersion profiles of the halo.

Our work implies that SIDM halos exhibit nearly universal gravothermal evolution, allowing for different cross-section models to yield similar halo evolution in the LMFP regime once the particle physics is scaled out, meaning that existing analytical models for constant cross-sections can be mapped onto velocity-dependent cases. We have presented our findings in terms of parameters typically used in simulations such as $V_{\rm max}$ and r_s, which facilitates easy validation of our work through N-body simulations in future works. Our work offers a robust framework for capturing average behaviors in terms of density, dispersion, and timescales, and constraining the interaction cross-section, once calibrated to N-body simulations.

4.A Caveats about the Self-Similar Solution

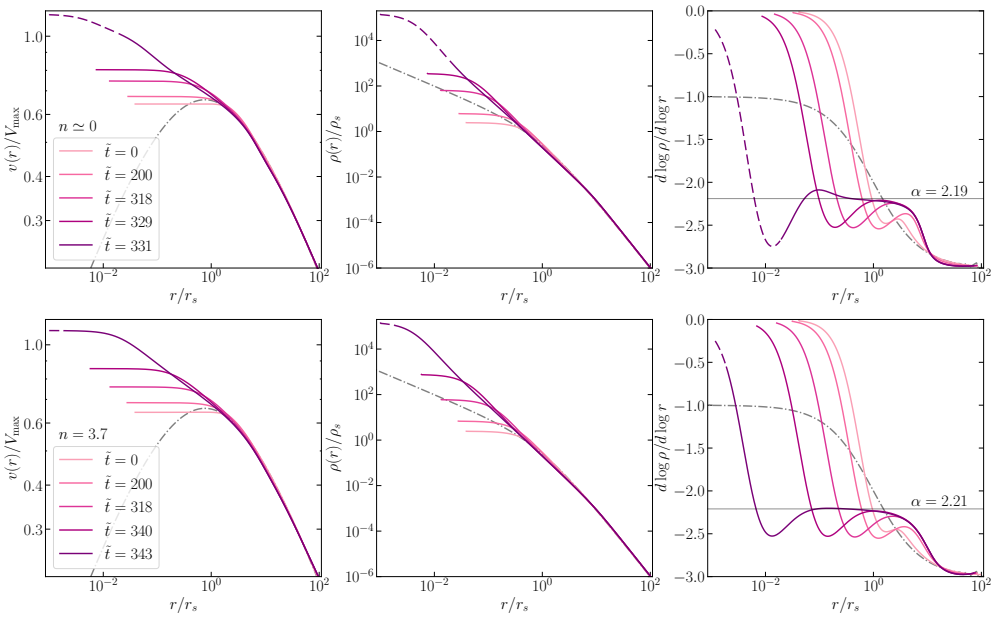

Figure 4.5: The velocity dispersion profiles, density profiles, and log slopes of these density profiles for $n \simeq 0$ in the top row and $n = 3.7$ in the bottom row. Time step of each profile plotted is listed in the legend ($\tilde{t} = (t - t_{\rm core})/t_{c,0}$). Dashed part of the curves represent the part of the halo that has entered the SMFP regime. We show the initial NFW profile in dashed-dotted gray. The dashed-dotted gray curves represent the initial NFW profiles. We show the α computed from Eq. (4.22) in the third column.

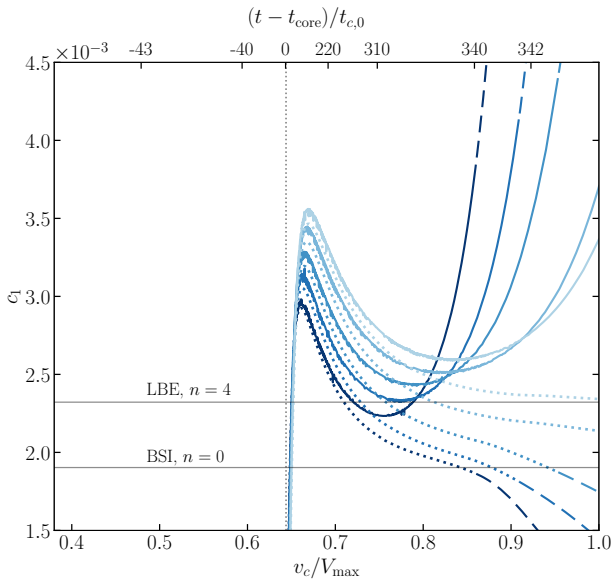

Figure 4.6: SOV constant c_1 vs $v_c/V_{\rm max}$. Dotted lines are computed the same way as those shown in Fig. 4.3, using Eq. (4.18), while solid lines come from Eq. (4.25). The figure highlights the deviations from the requirements for self-similarity of halos via the differences between the two methods.

In this section of the appendix, I will briefly outline how it is evident that there are departures from the self-similarity requirements as shown in my numerical results, and as compared to the analytic forms [106]. This is shown in Fig. 4.5, and in Fig. 4.6. Recall that a requirement for self-similarity is that the slope of the density profile scales as $r^{-\alpha}$, as in Eq. (4.19). We show the log-slope of the density profile, $d\log\rho/d\log r$, in Fig. 4.5, which shows that the halo reaches a slope of $-\alpha$ around $r \simeq r_s$, which is shown by the horizontal gray line (which comes from the right panel of Fig. 4.3). This is reassuring as it confirms the time and space components of the self-similar solution, Eq. (4.22). The self-similarity requirement that the density scales as Eq. (4.19) requires that α is constant between -2.5 and -2 [88, 8]. But as we see in the third column of Fig. 4.5, the outer profile of the halo for all time steps plotted is more like NFW, with a slope ~ -3. This implies that the self-similarity condition is broken. Of course this is expected since the outer halo is dilute and thus thermalizing is suppressed due to very low rates of self-interactions, which is why we can assume CDM for the outer parts of a halo.

We can also see that the self-similarity requirement breaks, and as such is approximate, in Fig. 4.6, in which I used two methods to plot the SOV constant c_1, one of which we show in the left panel of Fig. 4.3 (which correspond to the dotted lines in Fig. 4.6 computed with Eq. (4.18)). We can see that the dotted curves only nearly reach a constant for $n = 3.7$ and $n = 3$, while the other cases do not reach a constant. The second set of curves in Fig. 4.6 (solid) are plotted using [106]

$$\lim_{r\to 0}\left(\frac{d\log v^2}{d\log\rho}\right)_t = \lim_{r\to 0}\frac{(\partial\log v^2/\partial r)_t}{(\partial\log\rho/\partial r)_t} = \frac{c_1}{1-c_1} \simeq c_1\,, \tag{4.25}$$

which comes from $\rho_* \simeq 1 - \frac{1-c_1}{6}r_*^2$, $v_* \simeq 1 - \frac{c_1}{12}r_*^2$ [106]. The derivative in Eq. (4.25) is taken for a fixed time. Looking at Fig. 4.6, we see the agree up until $0.75 - 0.80\, v_c/V_{\rm max}$, after which the two methods diverge far before the halos fall into the SMFP. This is a clear indication that the self-similar solution is approximately valid for a limited amount of time, after which my numerical results clearly show they diverge from the self-similar solution.

Finally, the analytic result [106] for the collapse time shown in Eq. (4.23) predicts that the core collapses at $t_{\rm coll} \simeq 430$, however my numerical results show that the halo cores collapse at $t_{\rm coll} \simeq 330$. Additionally, an important thing my numerical results clearly indicate is that larger n return longer collapse times, as shown in Fig. 4.1. But Eq. (4.23) implies instead that smaller n result in later collapse times. Our assumption is that this discrepancy also comes from the fact that the self-similarity is only approximate, although it is not clear how the departure from self-similarity would affect the analytic results.

4.B Table of Parameters used in Gravothermal Code

In this section of the Appendix, I include a table with a list of the parameters from the halos I ran with the gravothermal code for our work. The input parameters are those I used to

define each halo I ran, which some spread in the mass and concentration, and the output parameters are those that are the results of the numerical runs.

Run	ρ_s $\left[10^7 \frac{M_\odot}{\mathrm{kpc}^3}\right]$	r_s [kpc]	$V_{\max}$ $[\frac{\mathrm{km}}{\mathrm{s}}]$	$\frac{\sigma_0}{m_{\mathrm{dm}}}$ $[\frac{\mathrm{cm}^2}{\mathrm{g}}]$	w $[\frac{\mathrm{km}}{\mathrm{s}}]$	$\rho_{c,0}$ $[10^7 \frac{M_\odot}{\mathrm{kpc}^3}]$	$v_{c,0}$ $[\frac{\mathrm{km}}{\mathrm{s}}]$	$\frac{\rho_{c,0}}{\rho_s}$	$\frac{v_{c,0}}{V_{\max}}$	$\frac{\sigma_c}{m_{\mathrm{dm}}}$ $[\frac{\mathrm{cm}^2}{\mathrm{g}}]$	$\frac{\sigma_{100}}{m_{\mathrm{dm}}}$ $[\frac{\mathrm{cm}^2}{\mathrm{g}}]$	n	$\hat{\sigma}$	$\hat{w}$
1	2.0	3.0	45.9	5.0	10^4	4.9	29.5	2.5	0.64	5.0	5.0	2.1×10^{-4}	0.029	339.5
2	2.0	3.0	45.9	10	95.1	4.9	29.5	2.5	0.6	4.9	0.64	1	0.025	3.2
3	2.0	3.0	45.9	40	40.2	4.9	29.5	2.5	0.64	5.3	0.24	2	0.023	1.4
4	2.0	3.0	45.9	1×10^3	10.8	4.9	29.5	2.5	0.64	4.60	0.09	3	0.019	0.37
5	2.0	3.0	45.9	4×10^6	1.0	4.9	29.51	2.45	0.64	5.6	0.06	3.7	0.020	0.034
6	4.0	4.0	86.5	5	10^4	9.8	55.5	2.45	0.64	5.0	5.0	7.4×10^{-6}	0.077	180.1
7	2.0	3.0	45.9	1.0	10^4	4.9	29.5	2.5	0.64	1.0	1.0	2.1×10^{-4}	0.0058	339.5
8	40	0.8	54.7	5	10^4	98.1	35.1	2.5	0.64	5.0	5.0	3.0×10^{-4}	0.15	284.7
9	40	0.8	54.7	4×10^6	1.0	98.0	35.2	2.5	0.64	5.6	0.06	3.7	0.056	0.028
10	2.0	3.0	45.9	4×10^7	1.0	4.9	29.5	2.5	0.64	55.4	0.60	3.7	0.20	0.034
11	2.0	3.0	45.9	6.7×10^7	1.0	4.9	29.5	2.5	0.64	92.9	1.0	3.7	0.34	0.034

Table 4.1: Table of input parameters (ρ_s, r_s, $V_{\max}$, σ_0/m_{dm}, and w) and output parameters ($\rho_{c,0}$, $v_{c,0}$, $\frac{\rho_{c,0}}{\rho_s}$, $\frac{v_{c,0}}{V_{\max}}$, $\frac{\sigma_c}{m_{\mathrm{dm}}}$, $\frac{\sigma_{100}}{m_{\mathrm{dm}}}$, n, $\hat{\sigma}$, and $\hat{w}$). Runs 1-5 are the main runs in this work. The parameter σ_{100} is defined as $\sigma_{100} = \sigma(v_{100}) = \sigma(100\,\mathrm{km/s})$.

Chapter 5

On the Late-Time Evolution of Velocity-Dependent Self-Interacting Dark Matter Halos

This chapter is based on the paper "On the Late-Time Evolution of Velocity-Dependent Self-Interacting Dark Matter Halos" written by Sophia Gad-Nasr, Kimberly K. Boddy, Manoj Kaplinghat, Nadav Joseph Outmezguine, and Laura Sagunski [58].

Abstract

We study the evolution of isolated self-interacting dark matter (SIDM) halos that undergo gravothermal collapse and are driven deep into the short-mean-free-path regime. We assume spherical Navarro-Frenk-White (NFW) halos as initial conditions and allow for elastic dark matter self-interactions. We discuss the structure of the halo core deep in the core-collapsed regime and how it depends on the particle physics properties of dark matter, in particular, the velocity dependence of the self-interaction cross section. We find an approximate universality deep in this regime that allows us to connect the evolution in the short- and long-mean-free-

path regimes, and approximately map the velocity-dependent self-interaction cross sections to constant ones for the full gravothermal evolution. We provide a semi-analytic prescription based on our numerical results for halo evolution deep in the core-collapsed regime. Our results are essential for estimating the masses of the black holes that are likely to be left in the core of SIDM halos.

5.1 Introduction

The nature of dark matter remains one of the most pressing questions in physics. We have a wealth of data that constrains the interactions of dark matter with the Standard Model (SM). However, less is known about the possible self-interactions of dark matter. Self-interactions arise generically in dark sector models of physics beyond the SM and astrophysics provides a way to constrain or measure its strength [139, 1]. Early models of SIDM featured contact interactions with constant cross sections [134], but it has become evident that the cross section must vary with velocity in order to match observations of cores in dwarf galaxies [47, 139, 141, 1] while avoiding constraints on cluster scales [21, 87, 109, 75, 49, 139, 124]. Viable velocity-dependent SIDM models also lead to a large diversity in the rotation curves of galaxies as observed [105] while maintaining all the successes of ΛCDM on large scales [72, 117].

A key feature of the evolution of SIDM halos is the possibility of gravothermal core collapse [8]. Core collapse is unlikely to occur in the vast majority of field halos, however the gravothermal evolution will be faster in some satellite galaxies and subhalos, which could result in core collapse [103, 157]. It has been argued that core collapse must occur in some of the satellite galaxies if SIDM is to explain the diversity in the halo densities of the Milky Way (MW) satellites [71, 76, 156, 33, 70, 141]. It seems clear from recent work comparing the densities of the MW satellites to SIDM models that do not allow for collapse

that such models cannot be viable [114, 143, 78, 130]. If the gravothermal collapse proceeds far enough in some halos, we expect the mean free path of dark matter particles to become significantly shorter than the core size. In this regime, we do not have accurate simulations or analytic framework. In this work, we explore the gravothermal core collapse phase in the short mean free path regime allowing us to extend existing analytic approximations to high core temperatures.

The evolution of an isolated, thermalized SIDM halo can be described by a set of gravothermal fluid equations. In the early stages of evolution, the halo is sufficiently dilute such that a dark matter particle completes many orbits before scattering with another dark matter particle. In this long-mean-free-path (LMFP) regime, the gravothermal evolution exhibits self-similar behavior, as demonstrated in our previous work ([106], hereafter referred to as O23) and other works (for example, [88, 8, 83]). The gravothermal evolution is unstable, leading to a runaway process in which the core of a halo collapses [89, 82, 8, 27, 83, 112, 126, 50, 156, 103, 33, 141]. Due to the self-similarity, all gravothermal halos undergo universal evolution leading to core collapse, and the physical timescale on which the collapse occurs depends on the particle physics of the halo, such as the SIDM cross section [8, 106], truncation of the NFW profile due to tidal effects [103, 33], the presence of baryons [120, 126, 54], and dissipative interactions [50, 151, 55].

As gravothermal evolution proceeds, the core of the halo is driven deep into the core-collapse phase, entering the short-mean-free path (SMFP) regime in which the high density of particles allows them to undergo numerous collisions along each orbit. The evolution of the core in the SMFP regime becomes distinct from that of the outer halo, which remains in the LMFP regime. The properties of the core change much more rapidly in the SMFP regime than in the LMFP regime; for example, the central density of the core increases many orders of magnitude in extremely short time periods, and the temperature increases much more rapidly, compared to the LMFP evolution. Thus, the universality of the core evolution

in the LMFP regime is not expected to hold in the SMFP regime. No previous studies have investigated the SMFP regime to see if the core maintains some form of universal evolution, even if approximate. If such a universality exists, the gravothermal evolution of any halo could be generically characterized from its initial stage to its gravothermal catastrophe, when the core is expected to reach a relativistic instability that produces a black hole.

Previous works have estimated black hole masses resulting from the relativistic instability (see for example [8, 83, 103, 91]). However, lacking accurate evolution characteristics of halos in the SMFP regime results in inaccurate estimates of the core mass at the relativistic instability. If black holes can be produced from the core collapse of dark matter halos, production always occurs deep in the SMFP regime. It is therefore imperative to understand the SMFP core evolution to determine the core properties in this regime.

In this paper, we explore the SMFP regime and study the evolution of the cores of initially NFW, isolated, virialized SIDM halos by solving the spherically symmetric gravothermal fluid equations. We show that the universality exhibited in O23 breaks down when the halo transitions from the LMFP to the SMFP regime. We discover a new, approximately universal solution to the gravothermal equations during the phase of evolution when the thermal energy of the core becomes constant with respect to the 1-dimensional (1D) velocity dispersion and time. The transition into this phase cannot be predicted analytically. Fortunately, we find that the transition point can be related to the LMFP-to-SMFP transition, which is analytically described in O23. We also quantify the scaling of the core mass as a function of the central velocity dispersion during this phase of approximate SMFP universality. We find more accurate relations for the core structure in the SMFP. As an application, we find the core mass at the relativistic instability, which would be the minimum mass available for black hole formation, and show that the mass loss is steeper than previously thought, resulting in smaller core masses at the relativistic instability. Finally, we present a recipe to easily compute the core properties of halos evolving deep in the SMFP regime.

This paper is organized as follows: In §5.2 we present the gravothermal equations and expressions for the heat conductivity, and we summarize our numerical procedure. In §5.3 we discuss the LMFP and SMFP evolution and formulate new designations for each stage of evolution. In §5.4 we present the analytic description of the new SMFP universality and validate it with our numerical solutions of the gravothermal equations in the SMFP regime. In §5.5 we implement a method to analytically determine the parameters in the constant-thermal-energy phase and outline a step-by-step recipe for obtaining the SMFP core mass and black hole mass. The implications and limitations of this work are summarized in the conclusions in §5.6. We include a derivation of the SMFP universal solution in Appendix 5.A, show the dependence of the new SMFP parameters on the concentration of the halo in Appendix 5.B, address issues of numerical resolution in Appendix 5.C, and discuss the validity of approximations used in this paper in Appendix 5.D.

5.2 Gravothermal Evolution

The gravothermal evolution for a spherically symmetric, isolated, virialized halo is given by the following relations for mass conservation, hydrostatic equilibrium, Fourier's Law, and the first law of thermodynamics [136, 88, 8, 103]:

$$\begin{aligned} &\frac{\partial M}{\partial r} = 4\pi r^2 \rho \ , \quad \frac{\partial(\rho v^2)}{\partial r} = -\frac{GM\rho}{r^2} \ , \quad \frac{L}{4\pi r^2} = -\kappa \frac{\partial T}{\partial r} \ , \\ &\frac{\partial L}{\partial r} = -4\pi r^2 \rho v^2 \left(\frac{\partial}{\partial t}\right)_M \log\left(\frac{v^3}{\rho}\right), \end{aligned} \tag{5.1}$$

where ρ is the halo density, M is the mass enclosed within radius r, L is the luminosity, and v is the 1D velocity dispersion. The entropy appears in the first law as $\log(v^3/\rho)$, and the temperature is related to the 1D velocity dispersion via $T = m_{\rm dm} v^2$ from the kinetic theory of gases, where $m_{\rm dm}$ is the dark matter particle mass.

Parameter	Definition
$r_{\rm core}$	Radius at which relation $\rho(r_{\rm core}) = \rho_c/2$ is satisfied for each snapshot in time
$t_{\rm core}$	Time at which the core size is a maximum (and central density is a minimum)
$t_{c,0}$	LMFP scattering timescale (see Eq. (5.19))
$X_c(t)$	Variables that describe the properties of the core (densest region in the halo) like mass ($M_c(t)$), density ($\rho_c(t)$) and velocity dispersion ($v_c(t)$)
$X_{c,0} \equiv X_c(t_{\rm core})$	Core properties at the time $t_{\rm core}$
$X_{c,\rm LS} \equiv X_c(t_{\rm LS})$	Core properties at the time when the scatterings in the core transition from being in the LMFP to SMFP regime
$X_{c,10} \equiv X_c(t_{10})$	Core properties at time the core enters a new phase in SMFP (Stage 3 in §5.3)
X_N	Scale quantities taken at some point N
$\sigma_{c,0}$, $\sigma_{c,\rm LS}$, $\sigma_{c,10}$	The value of the cross section, $\sigma_0 K_p$, with the velocity dependence taken at $v_{c,0}$, $v_{c,\rm LS}$, $v_{c,10}$ (see Eq. (5.4))
$n_{c,0}$, $n_{c,\rm LS}$, $n_{c,10}$	The log-slope of the cross section at the velocity scales $v_{c,0}$, $v_{c,\rm LS}$, $v_{c,10}$ (see Eq. (5.9))
$\hat{\sigma}_{c,0}$, $\hat{w}_{c,0}$	$\hat{\sigma}$ and $\hat{w}$ in Eq. (5.8) evaluated at the scattering timescale $t_{c,0}$

Table 5.1: Table of parameters and their definitions. The first block of parameters are the core radius $r_{\rm core}$, the time of core formation $t_{\rm core}$, and the scattering timescale $t_{c,0}$. In the second block, the variable X is a placeholder for all the physical quantities used in the paper. The quantities ρ_c, v_c are taken at the center of the halo (see Appendix 5.C.2 for details about how we address this numerically), while r_c, M_c, L_c are taken at the core radius, which is definition dependent. In the last block, we include definitions involving the scattering parameters σ_c, n_c, $\hat{\sigma}, \hat{w}$.

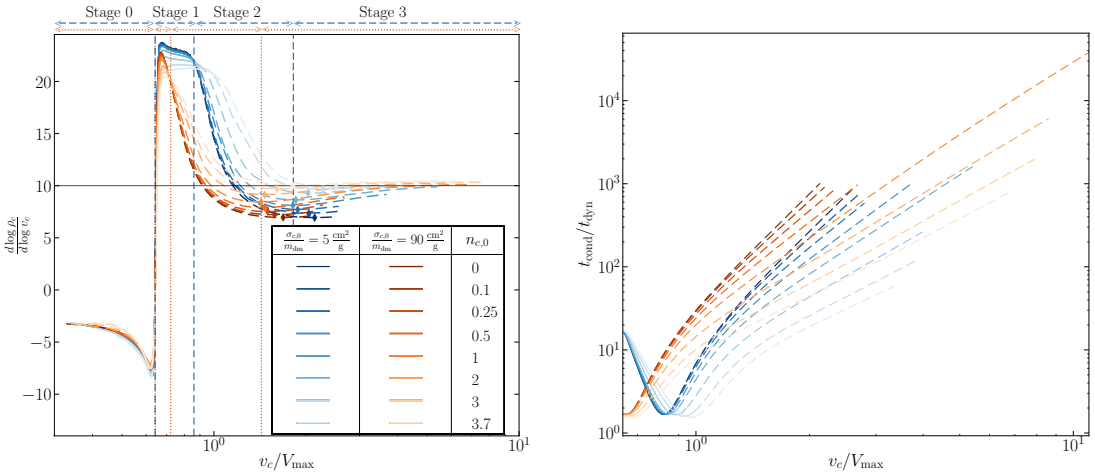

Figure 5.1: *(Left)* The log slope of the central density as a function of the central velocity, normalized by $V_{\rm max}$. Dashed lines represent the SMFP evolution of each halo. The black horizontal line shows the $\gamma = 10$ slope the halos asymptote to after the $\gamma = 10$ transition (indicated by diamonds). The stages of gravothermal evolution are labeled and described in Sec. 5.3. The orange curves have larger $\hat{\sigma}$ and thus transition into the SMFP regime earlier. We indicate the division of stages for each set of curves separately with vertical dashed (dotted) lines for the blue (orange) curves. *(Right)* The quantity $t_{\rm cond}/t_{\rm dyn}$ as a function of $v_c/V_{\rm max}$. The conduction timescale is $t_{\rm cond} = t_{\rm LMFP} + t_{\rm SMFP}$, where $t_{\rm LMFP} = t_{c,0}$ and $t_{\rm SMFP}$ is defined in Eq. (5.17). The dynamical timescale $t_{\rm dyn}$ is defined in Eq. (5.20).

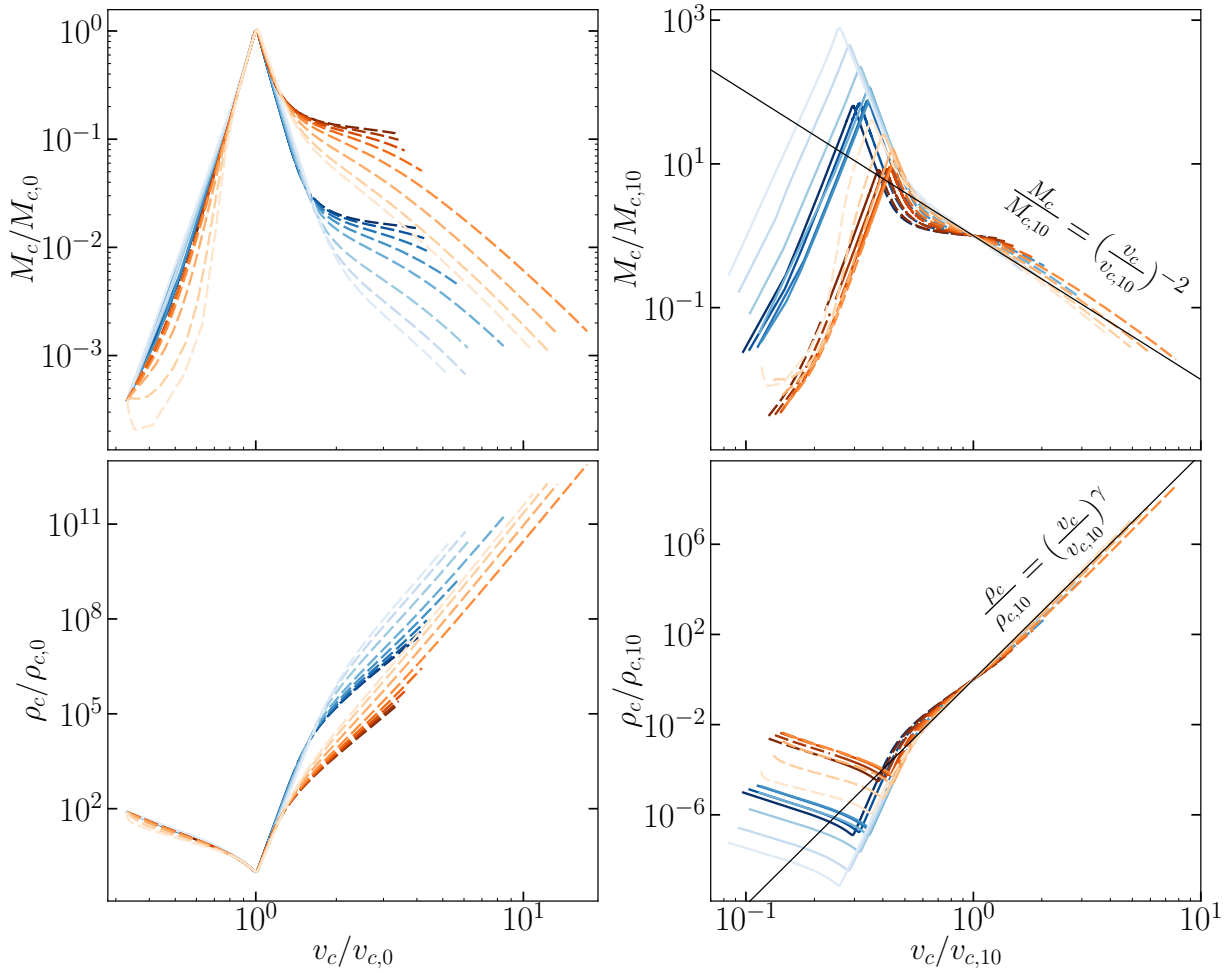

Figure 5.2: *(Upper Left)* The evolution of the core mass as a function of the central velocity, normalized by the LMFP scales as in O23, taken at core formation. The dashed lines represent the evolution in the SMFP regime, where for large v_c, the scatter in the halos is large. *(Upper Right)* Same as panels to the left, except here we normalize with the new scales in the SMFP, $M_{c,10}, v_{c,10}$, when the halos have reached the SMFP universal solution at the slope $\gamma = 10$. The scatter in the SMFP lines has decreased significantly and shows an approximate universality. *(Lower Left)* Same as figure above, but here it is the central density as a function of velocity. *(Lower Right)* Same as figure above, but here it is the central density vs. central velocity, both normalized by new scales $\rho_{c,10}, v_{c,10}$. A more detailed explanation of our parameter definitions and notations can be found in Table 5.1.

Run	Color	$\frac{\sigma_0}{m_{\rm dm}}$ $[\frac{\rm cm^2}{\rm g}]$	w $[\frac{\rm km}{\rm s}]$	$\rho_{\rm LS}$ $[10^{10}\,\frac{M_\odot}{\rm kpc^3}]$	$v_{\rm LS}$ $[\frac{\rm km}{\rm s}]$	ρ_{10} $[10^{14}\,\frac{M_\odot}{\rm kpc^3}]$	v_{10} $[\frac{\rm km}{\rm s}]$	$\frac{\sigma_c}{m_{\rm dm}}$ $[\frac{\rm cm^2}{\rm g}]$	$\frac{\sigma_{\rm LS}}{m_{\rm dm}}$ $[\frac{\rm cm^2}{\rm g}]$	$\frac{\sigma_{10}}{m_{\rm dm}}$ $[\frac{\rm cm^2}{\rm g}]$	$n_{c,0}$	$n_{\rm LS}$	n_{10}	$\hat{\sigma}_{c,0}$	$\hat{w}_{c,0}$
1		5.0	10^4	3.3	39.5	3.9	100.2	5.0	4.89	4.88	0.0003	0.0005	0.003	0.03	339
2		5.5	535	3.3	39.5	2.8	93.9	5.2	4.98	3.76	0.09	0.15	0.58	0.03	18.2
3		6	298	3.7	39.8	1.9	86.3	5.2	4.68	2.74	0.26	0.39	1.0	0.03	10.1
4		7	184.7	4.5	40.2	2.0	83.3	5.1	4.14	1.81	0.53	0.77	1.52	0.03	6.3
5		11	103.9	6.0	40.9	3.9	85.2	5.1	3.48	0.94	1.02	1.37	2.18	0.03	3.5
6		42	41.7	14.5	42.9	21.6	93.4	5.0	2.13	0.26	1.97	2.4	3.0	0.03	1.4
7		1050	11.8	40.0	45.5	144.2	104.5	5.1	1.15	0.07	3.01	3.3	3.5	0.03	0.4
8		5×10^6	1.0	92.3	47.7	666.7	115.3	5.0	0.71	0.03	3.67	3.7	3.8	0.03	0.03
9		90	10^4	0.016	31.4	0.016	77.4	90.0	88	87.9	0.0003	0.0003	0.002	0.5	339
10		96	535	0.016	31.4	0.011	72.6	91.6	89.4	74.5	0.09	0.1	0.4	0.5	18.2
11		105	298	0.017	31.5	0.009	68.8	91.2	88.5	59.3	0.26	0.27	0.82	0.5	10.1
12		125.4	184.7	0.017	31.5	0.009	67.2	90.8	87.2	44.0	0.53	0.56	1.29	0.5	6.3
13		195	103.9	0.017	31.6	0.01	65.6	91.1	84.7	28.5	1.02	1.09	1.9	0.5	3.5
14		770	41.7	0.021	31.9	0.02	67.3	92.3	76.2	12.1	1.97	2.1	2.8	0.5	1.4
15		1.9×10^4	11.8	0.029	32.6	0.09	73.8	92.0	60.8	4.12	3.01	3.1	3.4	0.5	0.4
16		9×10^7	1.0	0.041	33.2	0.44	83.3	90.8	48.8	1.58	3.67	3.7	3.8	0.5	0.03

Table 5.2: Table of parameters for all halo runs. Input parameters for the code are ρ_s, r_s, $\sigma_0/m_{\rm dm}$, and w. The parameters $\rho_{c,\rm LS}$, $v_{c,\rm LS}$, $\rho_{c,10}$, $v_{c,10}$ are obtained numerically, as are the parameters at core formation: $\rho_{c,0} \simeq 2.4\rho_s = 4.8\times10^7\,M_\odot/\rm kpc^3$, $v_{c,0} \simeq 0.64V_{\rm max} = 29.5\,\rm km/s$. All remaining parameters are derived. Runs $1-8$ all have $\sigma_{c,0} \approx 5\,\rm cm^2/g$, while runs $9-16$ have $\sigma_{c,0} \approx 90\,\rm cm^2/g$. All runs have $\rho_s = 2\times10^7\ M_\odot/\rm kpc^3$, $r_s = 3\,\rm kpc$, $V_{\rm max} \approx 1.65 r_s\sqrt{G\rho_s} = 45.9\,\rm km/s$. All $\hat{\sigma}_{c,\rm LS} = 1$ by definition. See Table 5.1 for the explanation of our notation.

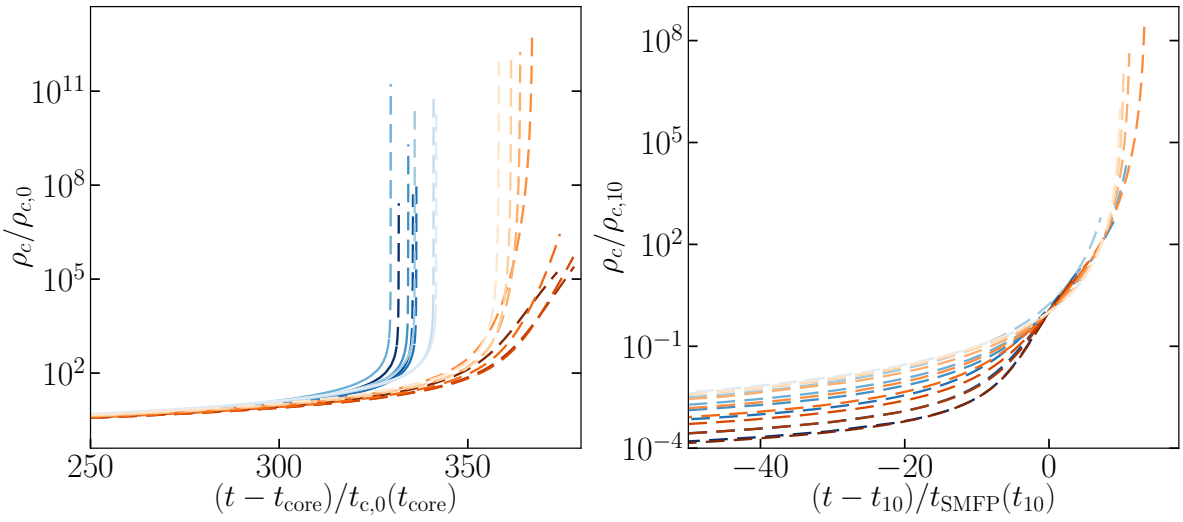

Figure 5.3: *(Left)* The evolution of the central density as a function of time, shifted and normalized to the time maximal core is reached as defined in O23. One can see that for different $\sigma_{c,0}$, the collapse times differ. *(Right)* Same as the left plot, except the time here is shifted and normalized to the time the halos enter the $\gamma = 10$ phase, where the curves line up relatively well as we are already in the self-similar solution. Note that here, the time the curves enter the $\gamma = 10$ phase is not analytically determined, thus resulting in the scatter.

5.2.1 Particle Physics via Conductivity

In this paper, we adopt the analogy of elastic Møller scattering in a Yukawa potential [63, 153]. As in [O23], we employ a velocity-dependent cross section through the differential cross section of the Born approximation:

$$\frac{d\sigma}{d\Omega} = \frac{1}{\pi}\frac{\sigma_0 w^4[(3\cos^2\theta + 1)v^4 + 4v^2w^2 + 4w^4]}{(\sin^2\theta v^4 + 4v^2w^2 + 4w^4)^2}. \tag{5.2}$$

where w is a scale velocity that is a measure of the ratio of the mediator mass to the dark matter mass, and σ_0 is a normalization prefactor, and θ is the scattering angle. This differential cross section allows us to examine velocity-dependent cross sections, as well as constant cross-sections, as it approaches a constant when the scale velocity w is taken to be very large. The particle physics model enters the equations only through the heat conductivity, κ, in Eq. (5.1).

An exact form for the conductivity exists in the SMFP regime, but the LMFP conductivity has only an approximate form and must be calibrated to simulations through a scaling parameter C. We follow the notation of O23 to parameterize the LMFP conductivity as

$$\kappa_{\rm LMFP} = \frac{3aC}{8\pi G}\frac{\sigma_0}{m_{\rm dm}^2}\rho v^3 K_5, \tag{5.3}$$

where $a = 4/\sqrt{\pi}$ and

$$K_p = \frac{\langle \sigma_{\rm visc} v_{\rm rel}^p \rangle}{\lim_{w\to\infty}\langle \sigma_{\rm visc} v_{\rm rel}^p \rangle}. \tag{5.4}$$

Here, $\sigma_{\rm visc} = \int d\sigma \sin^2\theta$ represents the viscosity cross section. We note that in O23, we used $p = 3$ in the LMFP conductivity. However, after we released our work, [154] released results of their N-body simulations of SIDM gravothermal collapse which showed that $p = 5$ is a better fit. We use their data to find that $C = 0.73$ matches best with $p = 5$. However,

in order to remain consistent with O23, we use $C = 0.6$, noting that the precise value of C does not impact our main, qualitative results. Moreover, the appropriate value of C for velocity-dependent SIDM requires comparison to simulations, which is beyond the scope of this work.

The SMFP conductivity computed in O23 is

$$\kappa_{\rm SMFP} = \frac{3}{2}\frac{bv}{\sigma_0}\frac{1}{K^{(2)}_{\rm eff}}, \tag{5.5}$$

where $b = 25\sqrt{\pi}/32$ and

$$K^{(2)}_{\rm eff} = \frac{28K_5^2 + 80K_5K_9 - 64K_7^2}{77K_5 - 112K_7 + 80K_9}. \tag{5.6}$$

As discussed in O23, we obtained $K_{\rm eff}$ from the Chapman-Enskog expansion [25, 110] at second order which provides up to a 20% correction to the SMFP heat conductivity. The next order correction results in sub-percent corrections, so we truncate the expansion at second order. Finally, we interpolate between the LMFP and SMFP regimes as follows:

$$\frac{1}{\kappa} = \frac{1}{\kappa_{\rm LMFP}} + \frac{1}{\kappa_{\rm SMFP}}. \tag{5.7}$$

5.2.2 Numerical Methods

Our numerical procedure closely follows our work in O23. We may recast Eq. (5.1) to be written in dimensionless form, which depends on only two dimensionless parameters:

$$\begin{aligned}\hat{\sigma}^2 &= \frac{aC}{b}K_5\left(\frac{1}{\hat{w}}\right)K^{(2)}_{\rm eff}\left(\frac{1}{\hat{w}}\right)\left(\frac{M_N}{4\pi r_N^2}\frac{\sigma_0}{m_{\rm dm}}\right)^2 \\ &= \frac{aC}{b}K_5\left(\frac{1}{\hat{w}}\right)K^{(2)}_{\rm eff}\left(\frac{1}{\hat{w}}\right)\frac{\rho_N}{4\pi G}\left(v_N\frac{\sigma_0}{m_{\rm dm}}\right)^2, \qquad \hat{w} = \frac{w}{v_N},\end{aligned} \tag{5.8}$$

where the scale parameters ρ_N, v_N, r_N, and M_N are related through $GM_N = r_N v_N^2$ and $M_N = 4\pi\rho_N r_N^3$. Instead of using the parameter $\hat{w}$, we can instead define the quantity n to characterize the velocity-dependent SIDM scattering. As in O23, we use the (positive) log-slope of the function K

$$n = -\frac{d\log K}{d\log v_N}, \tag{5.9}$$

where $K = K_5$ in the LMFP regime and $K = K_{\rm eff}^{(2)}$ in the SMFP regime.

We employ our gravothermal code used in O23 to evolve velocity-dependent SIDM halos according to the dimensionless form of Eq. (5.1). We assume halos initially have an NFW profile, and from O23, the NFW parameters are related to the central parameters at core formation as $\rho_{c,0} \simeq 2.4\rho_s$, $v_{c,0} \simeq 0.64 V_{\rm max}$ (see Table 5.1 for a description of our notation and definitions). We evolve 16 halos with the parameters listed in Table 5.2. For the purpose of maintaining numerical stability, we approximate fitted forms for Eq. (5.4), which we provide in Appendix 5.D.

We define the size of the core of a halo $r_{\rm core}$ via $\rho(r_{\rm core}) = \rho_c/2$. As the halo evolves, different regions of the halo may transition from the LMFP regime (for which $\kappa_{\rm LMFP} < \kappa_{\rm SMFP}$) to the SMFP regime (for which $\kappa_{\rm LMFP} > \kappa_{\rm SMFP}$). We use the condition

$$\left.\frac{\kappa_{\rm SMFP}}{\kappa_{\rm LMFP}}\right|_{r=r_{\rm core}} = 1 \tag{5.10}$$

to define the time when the core fully transitions from the LMFP to SMFP regime, and we refer to this time as the LS transition.

5.3 Long and Short Mean Free Path Evolution

We can delineate a halo undergoing gravothermal collapse into two regions: the outer halo and the central core. Gravothermal evolution leads to core collapse: the core contracts and heats up, leading to a high density and temperature, during which time dark matter self-interactions transport heat and mass to the outer halo. Meanwhile, the outer halo that surrounds the core remains relatively dilute and acts as a heat sink. The thermal evolution timescale of the outer halo is much longer than that of the core, so the outer halo changes temperature very slowly, while the core temperature increases rapidly. The outer halo remains in the LMFP regime, while the core can be in the LMFP, the SMFP, or an intermediate regime. The evolution in the two regimes differs substantially. In O23, we explored the LMFP regime in detail. In this paper, we focus on the SMFP regime. We provide a brief overview below of the two regimes.

In the LMFP regime, dark matter particles are sufficiently dilute such that particles can make many orbits before scattering. While the outer halo is always in the LMFP regime, for the core of a halo, this is not always the case. Given a large enough cross section, the core of a halo can begin in the SMFP regime. However at core formation, as we studied in depth in O23, the cores of halos evolve in the LMFP regime, and the LMFP solution represents the bulk of the time an isolated halo spends in its evolution. The self-scattering enables dark matter particles to transfer heat and mass between the inner and outer regions of the halo. Initially, heat is transferred inward from the hotter outer halo to the colder inner core, causing the core to expand until it reaches a maximum, or "maximal core." The core then transfers heat to the outer halo and shrinks, becoming denser and hotter. This runaway process inevitably drives the core into the SMFP regime and into the core collapse phase. The LMFP and SMFP regimes experience distinct evolution paths. This is illustrated in the curves of Figs. 5.1 (left panel) and 5.2 (all panels) where the dashed portions of the curves denote when the core is in the SMFP regime, whereas the solid portions indicate the LMFP

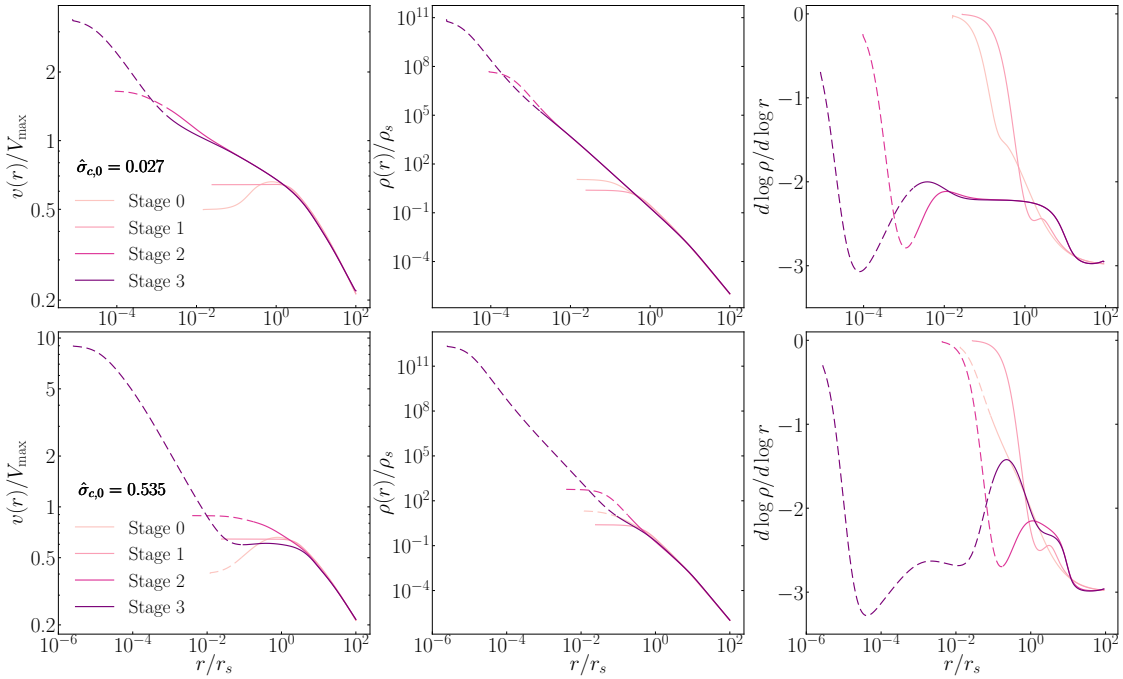

Figure 5.4: *(Left)* The velocity dispersion as a function of radius for Stages 0, 1, 2, and 3. The upper row is for a small $\hat{\sigma}$ with $n = 3.7$ corresponding to run 8 in Table 5.2, and the lower row is for large $\hat{\sigma}$ with $n = 1$ corresponding to run 13 in Table 5.2. *(Middle)* Density as a function of radius. *(Right)* Slope of the density profile with respect to radius.

regime. We delineate the LS transition as the point when the conductivities are equal, as in Eq. (5.10). Notably, the orange curves transition from SMFP (dashed) at low v_c values to LMFP (solid) and return to SMFP (dashed) at high v_c values. In contrast, the blue curves begin in the LMFP regime (solid) and switch to the SMFP regime (dashed) as v_c values increase. Thus, halos with substantial cross sections begin their evolution with their cores in the SMFP regime. Nonetheless, we assume NFW profiles as an initial condition, as we did in O23, noting that halo core formation causes the core to transition to the LMFP regime early in its evolution. It would be interesting to test other profiles with different inner slopes, for example, a roughly constant core. We know that profiles that are truncated in the outer regions due to tidal effects tend to speed up the onset of core collapse [126, 71, 103, 33], and thus it would be insightful to see how profiles with inner slopes that differ from $\sim r^{-1}$ may affect the evolution. We leave this interesting question to a future study.

In the SMFP regime, the core shrinks and drastically increases in density. In this regime, particles are so dense that collisions are very frequent. The dense core as a result hampers heat and mass transfer from the core to the outer halo [8, 2, 50]. After the shielding begins, the evolution paths of the outer and core become distinct, and the core can be treated approximately independently from the outer halo. Shortly after this transition, the core falls into a phase of constant thermal energy, where the log-slope of the central density with respect to central velocity dispersion becomes constant in time, approaching a slope of $\gamma = 10$; see Fig. 5.1. Here, the core heats up very quickly and the density shoots up by several orders of magnitude, which can be seen as a steady rise of the central density with respect to the central velocity in Fig. 5.2 (lower panels), as well as both panels of Fig. 5.3 where the central density shoots up during collapse. Looking at both Figs. 5.2 (lower panels) and 5.3, it is also evident that the timescale at which the LMFP and SMFP evolution proceeds is drastically different: while the bulk of the evolution resides in the LMFP, the SMFP evolution occurs very rapidly.

In the left panel of Fig. 5.1, we label each stage in the gravothermal evolution. We call the quantity $d\log\rho_c/d\log v_c$ as γ, given by

$$\frac{d\log\rho_c}{d\log v_c} = \gamma \tag{5.11}$$

where $\rho_c \propto v_c^\gamma$ with $\gamma \simeq 10$. Fig. 5.4 shows the density profiles for each of these stages. The outer halo remains largely unchanged throughout the evolution, but the core changes significantly. The stages are as follows:

- **Stage 0**: The Core Expansion Phase. During this initial phase, the halo's core undergoes an expansion process. While the core size increases, it experiences adiabatic heating and a concurrent gradual decrease in density.

- **Stage 1**: The Core Contraction Phase. This phase commences once the core reaches its maximal size and minimal central density, initiating a period of contraction. During this phase, the core decreases in size and increases in density. This marks the onset of the LMFP evolution phase, characterized by self-similarity and approximate LMFP universality, explored extensively in O23.

- **Stage 2**: The Unorganizable Phase. This phase signifies a departure from the self-similarity and universality found in the earlier stages. Here, the halo does not conform to any universally applicable solution. Despite this, we have developed semi-analytical formulae that effectively map the values of macroscopic parameters at the end of Stage 1 to those at the beginning of Stage 3. Detailed discussions on these formulae are provided in §5.4.

- **Stage 3**: The Constant Thermal Energy Phase. This phase represents the region beyond the $\gamma = 10$ transition where we identify a new SMFP universality. As depicted in the left panel of Fig. 5.1, all halos tend towards the slope $\gamma = 10$ during this stage, allowing us to fully characterize the evolution during Stage 3.

5.4 SMFP Approximate Universality

In the LMFP regime, the self-similar solution is most clearly seen by scaling the central (i.e., at the halo center) quantities ρ_c, $r_{\rm core}$, and v_c by their value at core formation, which we refer to as the instant of maximal core in O23. It represents the time at which the central density is at a minimum and the size of the core is at a maximum (see the left panels of Fig. 5.2). The approximate universality, however, breaks once the core enters the SMFP regime, as evident in the left columns of Figs. 5.2 and 5.3. As discussed in O23, the breakdown of universality at the LS transition is governed by the size of $\hat{\sigma}$.

In this section, we present a new approximate universality in the deep SMFP regime. This universality is evident upon scaling the central quantities by their respective values at the onset of Stage 3, as seen in the right column of Fig. 5.2 and 5.3. The onset of Stage 3 of the evolution is not as clear-cut as the LS transition and cannot be computed analytically; however, as previously stated, we approximate the point of the $\gamma = 10$ transition by taking the minimum of the curves in the SMFP regime in the left panel of Fig. 5.1. The evolution of the newly scaled quantities in the SMFP regime all align, as seen in the right panels of Figs. 5.2 and 5.3.

5.4.1 Analytic description of the Core Structure

We now show some analytical properties of the halo cores during Stage 3 in the deep SMFP regime. Detailed derivations are presented in Appendix 5.A.

We start by Taylor expanding the halo density and velocity dispersion profiles around the halo center:

$$\begin{aligned} \rho &= \rho_c \left(1 - x^2 + \mathcal{O}(x^4)\right), \\ v^2 &= v_c^2 \left(1 - \xi x^2 + \xi\beta x^4 + \mathcal{O}(x^6)\right), \end{aligned} \tag{5.12}$$

where $x = r/r_c$, and we have implicitly defined a core radius r_c as

$$r_c^{-2} = -\lim_{r\to 0} \left(\frac{\partial \log \rho}{\partial r^2}\right)_t . \tag{5.13}$$

We note that ξ can be calculated from our numerical results:

$$\xi = \lim_{r\to 0} \left(\frac{\partial \log v^2}{\partial \log \rho}\right)_t . \tag{5.14}$$

To leading order in x, mass conservation gives $M \simeq M_c x^3$, with $M_c = 4\pi\rho_c r_c^3/3$. Using the above expansion to the lowest order in the Jeans equation in Eq. (5.1), we find that the central quantities are related through

$$v_c^2 = \frac{GM_c}{2r_c(1+\xi)}. \tag{5.15}$$

As discussed earlier, we find that during Stage 3, $\rho_c \propto v_c^\gamma$ with $\gamma \simeq 10$. From the above relations, we see that $M_c \propto v_c^{3-\gamma/2} \simeq v_c^{-2}$, or

$$\frac{M_c}{M_{10}} = \left(\frac{v_c^2}{v_{10}^2}\right)^{-1}. \tag{5.16}$$

This scaling is nicely demonstrated in the bottom right panel of Fig. 5.2. It is important to point out that $\frac{d\log M_c}{d\log v_c^2}$ is not exactly -1, as a value of -1 indicates no core evolution [8]. But it is very close to -1 and so we use this approximation. We define the SMFP timescale as

$$t_{\rm SMFP} = \frac{\sigma_0 K_{\rm eff}^{(2)}(v_c)\, v_c}{2\pi b G m_{\rm dm}}, \tag{5.17}$$

and find in Appendix 5.A that

$$\lim_{r\to 0}\left(\frac{\partial \log(v^3/\rho)}{\partial t}\right)_r = -\frac{3}{t_{\rm SMFP}}\frac{\xi}{1+\xi}. \tag{5.18}$$

Note that through Eqs. (5.14) and (5.18), we obtain two different derivations of ξ: one through a temporal derivative and the other through spatial ones. The agreement between the two different derivations is demonstrated in Fig. 5.5.

It is not clear exactly why this approximate universality exists. Unlike the LMFP universality we found in O23, the SMFP universality does not have a simple analytic derivation, and we can only approximate the $\gamma = 10$ transition numerically. But once this approximation is

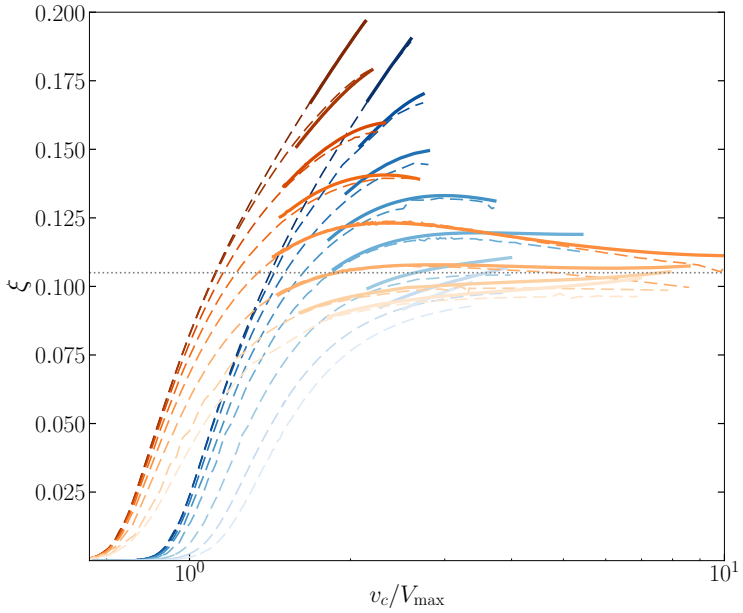

Figure 5.5: ξ as a function of $v_c/V_{\rm max}$. The dashed curves are obtained using Eq. (5.36) for ξ, and the solid ones obtained by using Eq. (5.14) for ξ. The dotted line indicates the line to which the curves tend to, which is $\xi \simeq 0.11$.

done, the universality does appear upon rescaling, and we produce analytic expressions for these parameters using the fits in Eq. (5.21).

Although the particle physics dependence (the velocity dependence of the cross-section) can be scaled out in Stage 1 (the LMFP) and Stage 3 ($\gamma = 10$ transition), Stage 2 (the drop from the LS transition to the $\gamma = 10$ transition in the left panel of Fig. 5.1) seems to have a non-trivial particle physics dependence. Accounting for this dependence is crucial to getting some analytic handle on the $\gamma = 10$ transition, which can be related to the LS transition, as shown in §5.5.1.

5.4.2 SMFP timescale and validity of the gravothermal equations

In the LMFP regime, changes in the evolution occur on the scattering timescale given by

$$t_N = \frac{2}{3aC}\left(\rho_N \frac{\sigma_0}{m_{\rm dm}} v_N K_5\left(\frac{v_N}{w}\right)\right)^{-1} \tag{5.19}$$

for which the core parameters are taken at core formation in the LMFP (see Table 5.1 for a full explanation of our definitions and notations at core formation, the LS transition, and $\gamma = 10$ transition). In the SMFP regime, the timescale is given in Eq. (5.17) where, as in Eq. (5.8), the core parameters can be taken at the LS or $\gamma = 10$ transitions depending on the stage of evolution. For the gravothermal equations to be valid, the relevant timescale must always be longer than the dynamical time

$$t_{\rm dyn} = \frac{1}{\sqrt{4\pi G \rho_N}}. \tag{5.20}$$

Note that $t_{\rm SMFP} \propto t_{\rm dyn}^2/t_{c,0}$, where $t_{c,0}$ is Eq. (5.19) taken at core formation. One may be concerned that the condition $t_{\rm SMFP} > t_{\rm dyn}$ is not fulfilled, because changes in the SMFP occur very rapidly. In the right panel of Fig. 5.1, note that $t_{\rm cond}/t_{\rm dyn} > 1$, and while it gets close to 1, it does so in the LMFP regime, which has been investigated in simulations that show the gravothermal equations are valid; see for example [154, 153]. Once the halos are in the SMFP regime (dashed lines), $t_{\rm cond}/t_{\rm dyn} > 1$ is always true. As long as the timescale of SMFP evolution is larger than the dynamical timescale, changes due to the evolution take longer than the dynamical time of the halo, allowing the halo to maintain hydrostatic equilibrium. Thus, the gravothermal equations remain valid.

5.5 Core mass at the Relativistic Instability

Previous works have made estimates of the core mass at the relativistic instability [8, 83, 103, 91]. However, lacking the properties of the halo in Stage 3 that we have found has led to overestimating this mass. The scaling used has been $\frac{d\log M_c}{d\log v_c^2} = -0.85$ [8, 83, 91] and extrapolating to the relativistic instability velocity, which is estimated to be $v_c \simeq c/3$ [55]. As we discuss next, this results in a substantial overestimation of the core mass. Examining the upper panels of Fig. 5.2, it becomes evident that the log slopes of the curves initially

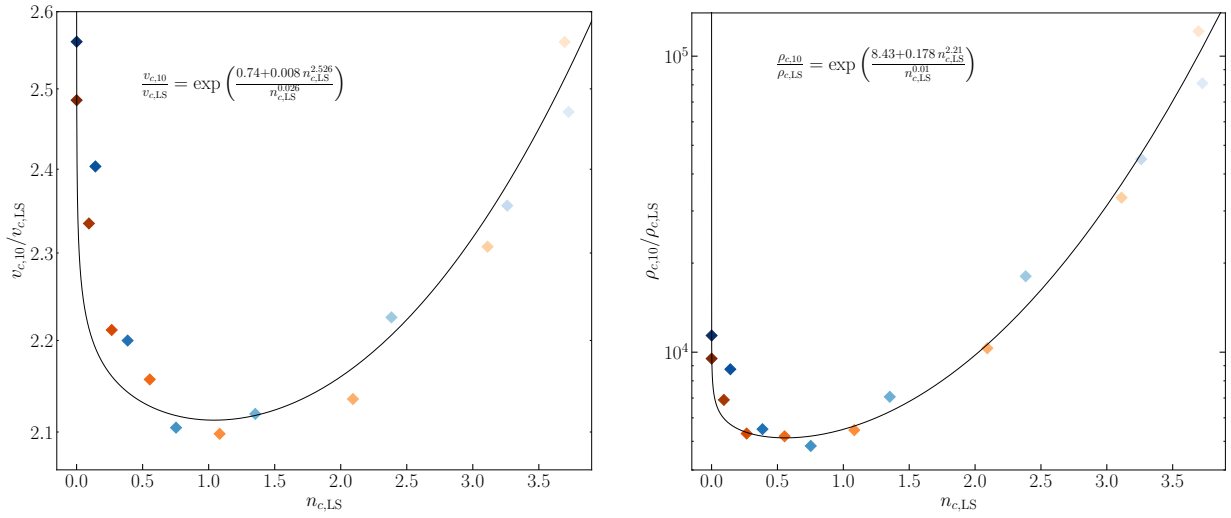

Figure 5.6: *(Left)* The $v_{c,10}/v_{c,\rm LS}$ to $n_{c,\rm LS}$ relation plotted as a black curve, fitted to our numerical results (diamonds). *(Right)* Same as the left, but for the $\rho_{c,10}/\rho_{c,\rm LS}$ to $n_{c,\rm LS}$ relation.

flatten to approximately -0.85 shortly after entering the SMFP regime (marked by dashed lines). This is followed by a steepening of the slopes, eventually converging to a log-slope of about -1. As we explained in §5.4.1, the slope cannot be exactly -1, but it is very close to it and steeper than -0.85.

In this section, we present a new, more rigorous, prescription in which we connect the core parameters at the LS transition to those in Stage 3 at the $\gamma = 10$ transition. This new prescription also affects the core mass obtained in the SMFP regime.

5.5.1 Relating the LS transition to the Stage 3 Parameters

As elaborated in Section 4, the onset of the newly identified universal phase—referred to as Stage 3—commences at the $\gamma = 10$ transition, for which we lack exact analytical predictions. In this section, we introduce empirical formulae that allow for the estimation of key halo core characteristics, starting from the core parameters at the LS transition. Given that these LS parameters can be analytically derived from the initial core characteristics, we essentially offer a semi-analytical framework to predict the core parameters at the $\gamma = 10$

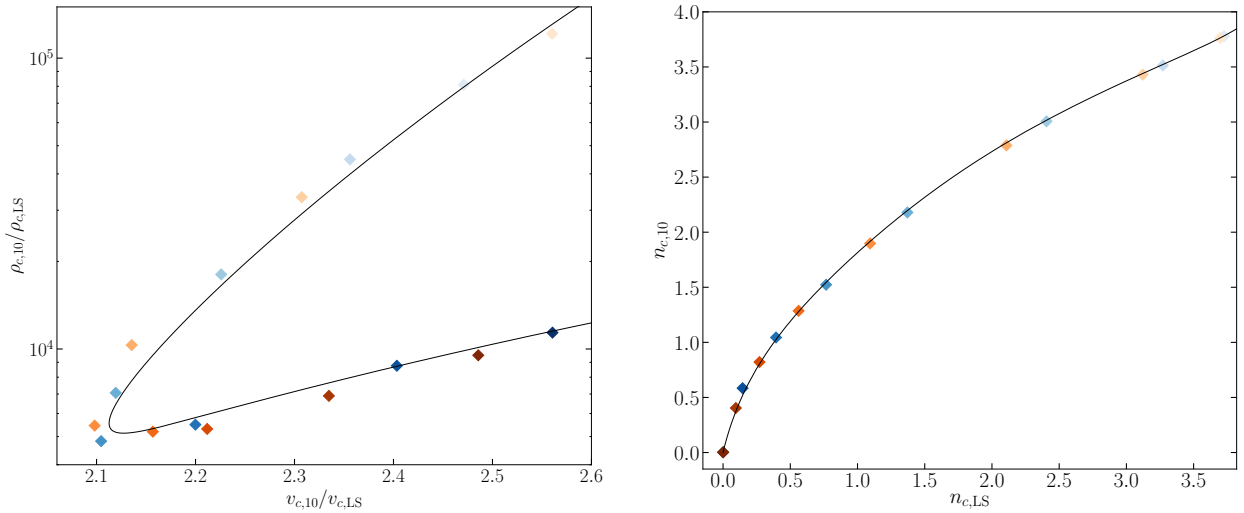

Figure 5.7: *(Left)* $\rho_{c,10}/\rho_{c,\mathrm{LS}}$ vs $v_{c,10}/v_{c,\mathrm{LS}}$ shown as a black curve fitted using the fits in Figs. 5.6, plotted over our numerical runs (diamonds). *(Right)* Plot of the $n_{c,10}$ to $n_{c,\mathrm{LS}}$ relation, fitted using the same relation as in the left panel of Fig. 5.6.

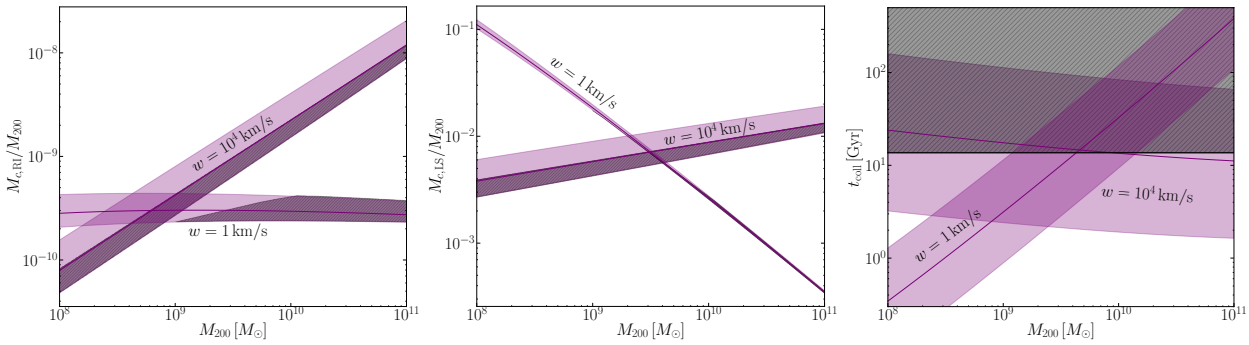

Figure 5.8: *(Left)* The ratio of $M_{c,\mathrm{RI}}/M_{200}$ with respect to the halo mass M_{200} for a cross section of $\sigma_0 K_p = 100\,\mathrm{cm}^2/\mathrm{g}$ at $v = 20\,\mathrm{km/s}$ with $w = 1\,\mathrm{km/s}$ and $w = 10^4\,\mathrm{km/s}$ (labeled). The band for the velocity independent model overtakes the velocity dependent one for masses larger than $10^9\,M_\odot$. The gray hatched shaded regions are those that do not collapse within the age of the universe (see right panel). *(Middle)* Same as the left panel, but for the core mass at the LS transition. *(Right)* Collapse time as a function of the halo mass for the same models as in the left panel, with the gray hatched shaded region above the line at (13.7 Gyr) indicating collapse times longer than the age of the universe. The bands for the cases of $w = 10^4\,\mathrm{km/s}$ and $w = 1\,\mathrm{km/s}$ are labeled in the figure. The purple shaded bands in all the figures cover a concentration of ± 0.3 dex around the median, represented by the dark purple line. In the first two figures, the upper (lower) bound of the bands correspond to higher (lower) concentration, while in the rightmost figure, the upper (lower) bound represents the lower (higher) concentration, indicating that higher concentration halos collapse faster.

transition based on the initial halo conditions and particle physics parameters. Using the approximate universality described in Section 4, this, in principle, allows for a semi-analytical halo evolution model throughout the different phases.

The relation between the LS and $\gamma = 10$ parameters is shown in Fig. 5.6, alongside the fitted lines given below:

$$\begin{aligned} \frac{v_{c,10}}{v_{c,\mathrm{LS}}} &= \exp\left(\frac{0.74 + 0.008 n_{c,\mathrm{LS}}^{2.5}}{n_{c,\mathrm{LS}}^{0.03}}\right) \\ \frac{\rho_{c,10}}{\rho_{c,\mathrm{LS}}} &= \exp\left(\frac{8.43 + 0.18 n_{c,\mathrm{LS}}^{2.21}}{n_{c,\mathrm{LS}}^{0.013}}\right) \end{aligned} \tag{5.21}$$

The fitted lines closely align with the behavior of the numerically calculated points. The above fits also introduce an implicit relation between $v_{c,10}/v_{c,\mathrm{LS}}$ and $\rho_{c,10}/\rho_{c,\mathrm{LS}}$, this implicit relation is the line shown on the left panel of Fig. 5.7. This line follows the numerical calculations quite accurately. Per the definition in Eq. (5.9), the log-slope, n, is a function of the central velocity dispersion, namely $n = n(v_c/w)$. Denoting the inverse relation by $v_c/w = f(n)$ we can express $v_{c,10}/v_{c,\mathrm{LS}} = f(n_{c,10})/f(n_{c,\mathrm{LS}})$, solving for $f(n_{c,\mathrm{LS}})$, and noting that $n[f(x)] = x$, we find that:

$$n_{c,\mathrm{LS}} = n\left[\frac{v_{c,\mathrm{LS}}}{v_{c,10}} f(n_{c,10})\right] . \tag{5.22}$$

The resulting line on the right panel of Fig. 5.7 validates this approach, as it closely matches our numerical calculations.

To complete our semi-empirical model, we need to provide a means for finding $n_{c,\mathrm{LS}}$, $v_{c,\mathrm{LS}}$ and $\rho_{c,\mathrm{LS}}$ from the initial halo parameters. In O23 we derived the scaling laws

$$\frac{v_{c,\mathrm{LS}}}{v_{c,0}} \simeq \hat{\sigma}_{c,0}^{-1/\delta} , \; \frac{\rho_{c,\mathrm{LS}}}{\rho_{c,0}} \simeq \left(\frac{v_{c,\mathrm{LS}}}{v_{c,0}}\right)^{\frac{2\alpha}{\alpha-2}} , \; \frac{M_{c,\mathrm{LS}}}{M_{c,0}} \simeq \left(\frac{v_{c,\mathrm{LS}}}{v_{c,0}}\right)^{\frac{6-2\alpha}{2-\alpha}} . \tag{5.23}$$

where $\delta \simeq 1 - n_{c,0} + \alpha/(\alpha - 2)$, and $\alpha \sim 2.2$ up to small but important scatter which is detailed in O23. With this at hand, we simply calculate $n_{c,\mathrm{LS}}$ by using Eq. (5.22). Having these relations allows us to have an analytic handle on the $\gamma = 10$ region, allowing one to obtain the parameters in the $\gamma = 10$ region by simply having the initial halo and cross-section model. Eq. (5.23) relies on the assumption that core formation occurs in the LMFP, which is satisfied when $\kappa_{\mathrm{SMFP}} \gg \kappa_{\mathrm{LMFP}}$ at the time of core formation, t_{core}. This implies that $\hat{\sigma} \ll 1$ [cf. Eqs. (5.3), (5.5), and (5.8)]. However, our numerical results demonstrate the effectiveness of Eq. (5.23) even in scenarios where $\hat{\sigma} \sim 1$, highlighting its applicability beyond its initial theoretical assumptions.

5.5.2 Obtaining the core mass at the relativistic instability from halo properties

Equipped with the results of the past section, we can derive updated predictions for the core mass at the onset of the relativistic instability. Before doing so, it is crucial to emphasize that the core mass at the point of relativistic instability, $M_{c,\mathrm{RI}}$, should be considered a lower limit for the mass that will ultimately collapse to form a black hole. We conjecture that the upper bound for black hole growth due to processes such as accretion is the mass within the region of the halo that is in the SMFP, and can be approximated as the core mass of the halo at the LS transition, $M_{c,\mathrm{LS}}$ (see App. 5.D, which outlines the validity of this approximation). The fraction of the mass that actually ends up in the black hole is a very interesting topic that requires relativistic treatment, and we leave this to a future study.

We express the core mass at LS transition through the relation in Eq. (5.23). Using Eq. (5.15) we express the core mass at the moment of $\gamma = 10$ as

$$M_{c,10} = \sqrt{\frac{6}{\pi}} \left(\frac{1+\xi}{G} \right)^{3/2} \frac{v_{c,10}^3}{\sqrt{\rho_{c,10}}}. \tag{5.24}$$

The mass at relativistic instability is thus approximately given by

$$M_{c,\mathrm{RI}} \simeq M_{c,10} \left(\frac{v_{c,10}}{v_{c,\mathrm{RI}}} \right)^2 , \tag{5.25}$$

where $v_{c,\mathrm{RI}} \simeq c/3$. To demonstrate the relevant mass scales, we use our analytic recipe (in §5.5.3) and focus on two example SIDM models, both having $\sigma_0 K_p = 100\ \mathrm{cm^2\,g^{-1}}$ at $v = 20\ \mathrm{km\,s^{-1}}$. The models demonstrate the two extremes of velocity dependence; the first has a velocity scale of $w = 1\ \mathrm{km\,s^{-1}}$ displaying strong velocity dependence, while the second, with $w = 10^4\ \mathrm{km\,s^{-1}}$, which is practically a constant cross section. We utilize the Python package COLOSSUS [39] for cosmological computations, along with a tight relation between the virial mass of a halo, and its concentration (where the concentration is defined as ratio of the virial radius to the scale radius of a halo) referred to as the concentration-mass relation (see for example [23, 45, 80] for a detailed account of the relation between concentration and mass of halos). We specifically use the concentration-mass relation from [40] to compute $M_{c,\mathrm{RI}}$, $M_{c,\mathrm{LS}}$ and t_{coll} using our recipe in §5.5.3 and illustrate our findings in Fig. 5.8.

The left panel of Fig. 5.8 shows the core mass at relativistic instability as a function of M_{200}, providing an estimated lower bound on the mass of the black hole formed from core collapse. The middle panel shows the core mass at the LS transition as a function of M_{200}, representing the estimated upper bound on the black hole mass. The right panel shows the collapse time (with the collapse time as defined in Eq. 29 of O23) of both models as a function of M_{200}, with the gray hatched shaded region representing timescales longer than the age of the universe, and thus, signifying halos that do not collapse in time. The width of the bands (shaded purple) in all three panels represents a spread around the median concentration (dark purple line) of 0.3 dex. For the left and middle panels of Fig. 5.8, the upper (lower) bound of the bands correspond to higher (lower) concentrations, while in the right panel, the upper (lower) bound of the bands represent lower (higher) concentrations, which is indicative of a more rapid collapse for halos with higher concentrations. The concentration dependence

of all these parameters (as well as the M_{200} dependence of $M_{c,\mathrm{LS}}$ and $M_{c,\mathrm{RI}}$) can be found in Appendix 5.B.

The left panel of Fig. 5.8 shows that higher $M_{c,\mathrm{RI}}$ are produced for all halo masses in the case of constant cross sections. What is particularly intriguing to note is that, given a high enough concentration, all halo masses with constant cross sections collapse within the age of the universe. Halos with highly velocity-dependent cross sections (namely $w = 1\,\mathrm{kms}^{-1}$) and masses over $\sim 10^9\,M_\odot$ do not collapse within the age of the universe, although a high concentration allows for halos up to $\sim 10^{10}\,M_\odot$ to collapse in time. In the case of a constant cross-section, halos of mass $M_{200} \sim 10^{10} - 10^{11}$ produce a minimum black hole mass ($M_{c,\mathrm{RI}}$) of order $1 - 10^3\,M_\odot$, while highly velocity-dependent ones of the same mass range do not collapse within the age of the universe. This shows that previous works have overestimated the core mass at the relativistic instability by about 2 orders of magnitude. One should keep in mind, however, that given the need for large cross sections on dwarf scales, constant cross sections have been ruled out by cluster constraints [75, 139, 124]. Another feature to note is that $M_{c,\mathrm{RI}}$ is almost linearly proportional to M_{200} in the highly velocity-dependent case, yielding a nearly straight band in the left panel of Fig. 5.8. This dependence on M_{200}, along with the relation in the middle panel, can be found in Appendix 5.B.

5.5.3 Recipe for analytically obtaining the core mass at the relativistic instability

With the tools presented in this paper, one can easily find the core mass of a halo using just the initial halo parameters and the particle physics of the halo. Here, we detail a step-by-step recipe for obtaining M_c at late times, and thus, an estimate for the core mass at the relativistic instability, the minimum mass available for black hole formation. As stated in

§5.5.2, although this procedure hinges upon relations that assume $\hat{\sigma} \ll 1$, we have tested it for halos with $\hat{\sigma} \sim 1$ and found that the predictions work remarkably well.

1. Find the maximal core parameters from the NFW halo parameters using the relations from O23:

$$\rho_{c,0} = 2.4\rho_s, \quad v_{c,0} = 0.64V_{\max}$$

2. Find the dispersion at LS transition, $v_{c,\mathrm{LS}}$.
   (a) Use Eq. (5.8) to obtain the dimensionless cross section.
   (b) Set $\alpha = 2.2$ and use Eq. (5.23) to find $v_{c,\mathrm{LS}}$. (α typically ranges from $2.19 - 2.22$ for $n_{c,0}$ from $0 - 3.7$, but 2.2 is a sufficient approximation.)
3. With the $v_{c,\mathrm{LS}}$ obtained in step (ii), use Eq. (5.9) to find $n_{c,\mathrm{LS}}$.
4. Use Eq. (5.23) to find the central density at the LS transition, $\rho_{c,\mathrm{LS}}$, and the core mass at LS transition, $M_{c,\mathrm{LS}}$.
5. With the $v_{c,\mathrm{LS}}$, $\rho_{c,\mathrm{LS}}$, $n_{c,\mathrm{LS}}$ found using the steps above, use our fit in Eq. (5.21) to obtain the central dispersion and density at the $\gamma = 10$ transition, $v_{c,10}$, $\rho_{c,10}$.
6. Find the core mass at the $\gamma = 10$ transition using our equation in Eq. (5.24).
7. Finally, using the second equation in Eq. (5.16), extrapolate to the relativistic instability at $v_c \sim c/3$, and find the minimum mass available for black hole formation using Eq. (5.25).

With these seven steps, one can determine the core mass at the relativistic instability, the minimum mass available for black hole formation, simply from knowing the NFW parameters and the assumptions for the particle physics model. See Fig. 5.8 for the band we obtained using the mass-concentration relation with Colossus [39] and this recipe.

5.6 Conclusions

We have examined the SMFP evolution of spherical, initially NFW, isolated halos for velocity-dependent SIDM with varied velocity dependence strength undergoing elastic scattering only. We show that in the SMFP regime, the core becomes distinct from the outer LMFP halo. For the first time, we discover a universality in the SMFP regime and the appropriate timescale in the SMFP evolution when the halo is deep in the core collapse. We find new scales that allow one to scale out the particle physics, specifically at the $\gamma = 10$ transition which leads into the constant thermal energy phase in Stage 3 of the halo evolution (see Fig. 5.1). It remains unclear why this universality exists, but we find this universality in all our runs for velocity-dependent SIDM halos. Although the $\gamma = 10$ transition point cannot be found analytically, we have determined a relation between the LS and $\gamma = 10$ transitions given in Eqs. (5.21) that allows to simply compute parameters in Stage 3 analytically given initial halo parameters and particle physics.

With these findings, we devise a recipe to estimate the core mass deep in the core collapse regime using the relation in Eq. (5.23), shown in Fig. 5.2, and our recipe in §5.5.3. We can use this recipe to compute the core mass at relativistic instability, which we expect would be the minimum mass available for black hole formation, given the initial halo parameters and particle physics. We find that previous works based on the gravothermal solutions have overestimated the core mass at relativistic instability by about 2 orders of magnitude. We find that the mass of the core reaches $\sim 10^3\, M_\odot$ at the relativistic instability only for $M_{200} \sim 10^{11}\, M_\odot$ and constant cross sections, while high velocity dependence prevents collapse from occurring in more massive halos. However, we note that other particle physics likely becomes important in this regime and may cause black hole formation to occur before the halo reaches $v_c \sim c/3$. Note that dissipation [50, 151, 55], halo truncation [103], and the presence of baryons [54] have been shown to cause halos to collapse faster, which could lead in larger black hole masses.

We compute the mass within the region of the halo that is in the SMFP regime as a function of time and show that it asymptotes to a constant value. We show that this constant mass can be estimated using the mass within the core when the core enters the SMFP regime to within an $\mathcal{O}(1)$ scatter (see App. 5.D. The core mass at the LS transition can be easily estimated given the analytic approximations derived in O23. We conjecture that this quantity is roughly the maximum mass available for black hole growth via other physical processes such as accretion.

The key takeaways are of our work are:

- *We have discovered, for the first time, a universal solution for halos in Stage 3 of the evolution (see Fig. 5.1).*
- *We have devised a method to analytically determine the* $\gamma = 10$ *transition parameters by relating them to the LS parameters defined in O23.*
- *We have outlined a step-by-step recipe to analytically determine the properties of the core deep in the core collapse regime, given the halo parameters and cross section for models with elastic scattering, without needing to run the gravothermal code. As an application, we determine the core mass at the relativistic instability, which serves as the minimum mass available for black hole formation.*

Coupled with our companion paper in O23, we now have appropriate relations to describe the entire gravothermal evolution of isolated halos, from the LMFP to SMFP regimes. This provides a simple way to analytically find the minimum core mass available for black hole growth after core collapse, given the initial halo parameters and assuming no physics other than elastic collisions. It is an interesting question to ask how these analytic predictions would change for tidally truncated halos and whether the universality based on the connection to the LMFP regime is retained to some extent. It would also be interesting

to extend our analysis to cases where baryons dominate the central potential well and where dissipative interactions are important.

Acknowledgements

MK and LS thank the Pollica Physics Center, where part of this research was carried out, for its warm hospitality. The Pollica Physics Center is supported by the Regione Campania, Università degli Studi di Salerno, Università degli Studi di Napoli "Federico I", the Physics Department "Ettore Pancini" and "E.R. Caianiello", and the Istituto Nazionale di Fisica Nucleare.

KB acknowledges support from the National Science Foundation (NSF) under Grant No. PHY-2112884. MK acknowledges support from the NSF under Grant no. PHY-2210283. The work of NJO was supported in part by the Zuckerman STEM Leadership Program and by the NSF under the grant No. PHY-1915314. The work of SGN was supported by the Departmental Dissertation Fellowship of the Department of Physics and Astronomy at the University of California, Irvine.

Data Availability

Our gravothermal code is available at `https://github.com/kboddy/GravothermalSIDM`. For a direct example of how to apply our recipe in §5.5.3, a sample script is available at `https://github.com/Nadav-out/Gravothermal-Instability-mass`. The data for all the runs in this paper are available from the corresponding author upon request.

5.A Semi-analytic Description of the Evolution of the Core

In this appendix, we derive some semi-analytical results, describing the central halo evolution in the deep SMFP regime. We start our derivation by focusing the short-distance behavior of the gravothermal solution. To do so, we Taylor expand near $r = 0$ the halo density and velocity dispersion profiles as[1]

$$\begin{aligned} \rho &= \rho_c \left(1 - x^2 + \mathcal{O}(x^4)\right), \\ v^2 &= v_c^2 \left(1 - \xi x^2 + \xi\beta x^4 + \mathcal{O}(x^6)\right), \end{aligned} \tag{5.26}$$

where $x = r/r_c$, and r_c is defined through

$$r_c^{-2} = -\lim_{r\to 0} \left(\frac{\partial \log \rho}{\partial r^2}\right)_t. \tag{5.27}$$

Note that ξ can be defined thorough

$$\xi = \lim_{r\to 0} \left(\frac{\partial \log v^2}{\partial \log \rho}\right)_t. \tag{5.28}$$

Mass conservation gives that

$$M = M_c \left(x^3 + \mathcal{O}(x^5)\right) \quad , \quad M_c = \frac{4\pi}{3}\rho_c r_c^3. \tag{5.29}$$

Using this in Jeans' equation we arrive at the relation

$$v_c^2 = \frac{GM_c}{2r_c(1+\xi)}. \tag{5.30}$$

[1] while the $\mathcal{O}(x^4)$ term in the expansion of ρ is of similar magnitude to that of v^2, we don't quote it here as it will not appear in any future steps.

To make use of the remaining gravothermal equations, we recall Eqs. (5.5) and (5.9), which allows us to write

$$\kappa_{\rm SMFP}(v) = \kappa_{\rm SMFP}(v_c)\left(1 - \frac{n+1}{2}\xi x^2 + \mathcal{O}(x^4)\right). \tag{5.31}$$

With this, the derivative of luminosity at short distances is given by

$$\frac{\partial L}{\partial r} \simeq 8\pi v_c^2 m_{\rm dm}\kappa_{\rm SMFP}(v_c)\xi x^2\left[3 - \frac{5}{2}x^2\left(4\beta + (n+1)\xi\right)\right]. \tag{5.32}$$

The above equation should be equated to the entropy conservation law of the gravothermal equations, Eq. (5.1). To do so, we first note that, using properties of partial derivative, we find that at small x the following holds true

$$\left(\frac{\partial f}{\partial t}\right)_M \simeq \left(\frac{\partial f}{\partial t}\right)_x - \frac{x}{3}\frac{d\log M_c}{dt}\left(\frac{\partial f}{\partial x}\right)_t. \tag{5.33}$$

Therefore

$$\left(\frac{\partial}{\partial t}\right)_M \log\frac{v^3}{\rho} \simeq D_1(t) - \frac{x^2}{3}(2-3\xi)D_2(t) \tag{5.34}$$

with $D_1 = d\log(v_c^3/\rho_c)/dt$ and $D_2 = d\log M_c/dt$. With this, entropy conservation gives

$$\frac{\partial L}{\partial r} \simeq -4\pi r_c^2\rho_c v_c^2 x^2\left\{D_1 - \frac{x^2}{3}\left[3(1+\xi)D_1 + (2-3\xi)D_2\right]\right\} \tag{5.35}$$

Equating to leading order the two expressions we have for dL/dr in Eqs. (5.32) and (5.35) we get

$$\frac{d\log v_c^3/\rho_c}{dt} = -\frac{3}{t_{\rm SMFP}}\frac{\xi}{1+\xi} \quad , \quad t_{\rm SMFP} = \frac{\sigma_0 K_{\rm eff}^{(2)}(v_c)v_c}{2\pi b G m_{\rm dm}}. \tag{5.36}$$

Moving to the next order in dL/dr we find

$$\left(\frac{2}{3}-\xi\right) t_{\rm SMFP}\frac{d\log M_c}{dt} = \left(3-10\beta+\frac{1-5n}{2}\xi\right)\frac{\xi}{1+\xi} \tag{5.37}$$

We recall that in the deep SMFP regime, we find that $\rho_c \propto v_c^\gamma$, with $\gamma \simeq 10$. Through Eq. (5.30), this also implies $M_c \propto v_c^{3-\gamma/2}$. With this in mind, the ratio of Eqs. (5.36) and (5.37) allows to relate γ to ξ, β and n

$$\xi = \frac{6+(20\beta-8)(\gamma-3)}{9-(2+5n)(\gamma-3)} \simeq \frac{10-28\beta}{1+7n} \tag{5.38}$$

5.B The dependence of the SMFP parameters on the concentration

In this section of the appendix, we outline the dependence of the SMFP parameters, such as the parameters at the LS transition, the $\gamma = 10$ transition, and the black hole mass, on the concentration, at fixed M_{200}.

To show how the parameters depend on the concentration, it is useful to outline these relations first:

$$\begin{aligned} &\frac{r_{200}}{r_s} = c_{200} \ , \\ &\frac{\rho_s}{\rho_{\rm crit}} = \frac{200}{3}\frac{c_{200}^3}{\log(1+c_{200})-\frac{c_{200}}{1+c_{200}}} \ . \end{aligned} \tag{5.39}$$

(see for example [97]). Given that our parameters depend on some combination of $\rho_s, V_{\rm max}$, we can go ahead and find the dependence on the concentration with fixed M_{200}.

It is right away useful to note that the dependence of ρ_s on c_{200} approaches c_{200}^3, but for the range of c_{200} we used in our spread, the power ranges between $p = 2.4 - 2.6$. We also note that $V_{\rm max} \propto \sqrt{\rho_s r_s^2}$ which allows us to find the dependence of $V_{\rm max}$ on c_{200}.

We now note that the LS transition parameters are related to $\rho_s, V_{\rm max}$ as follows:

$$
\begin{aligned}
v_{c,\rm LS} &= v_{c,0}\hat{\sigma}_{c,0}^{-1/\delta} \propto V_{\rm max}\hat{\sigma}_{c,0}^{-1/\delta} \ , \\
\rho_{c,\rm LS} &= \rho_{c,0}\frac{v_{c,\rm LS}}{v_{c,0}}^{\frac{2\alpha}{\alpha-2}} \propto \rho_s\left(\hat{\sigma}_{c,0}^{-1/\delta}\right)^{\frac{2\alpha}{\alpha-2}} \ , \\
\hat{\sigma} &\propto K_n\left(\frac{v_{c,0}}{w}\right) v_{c,0}\sqrt{\rho_{c,0}} \propto v_{c,0}^{n+1}\sqrt{\rho_{c,0}} \ , \\
v_{c,10} &\propto v_{c,\rm LS} \ , \ \rho_{c,10} \propto \rho_{c,\rm LS} \ , \\
M_{c,10} &\propto \frac{v_{c,10}^3}{\sqrt{\rho_{c,10}}} \ , \ M_{c,\rm RI} \propto M_{c,10}v_{c,10}^2 \ .
\end{aligned}
\tag{5.40}
$$

We now see how nicely all the SMFP parameters are related to $V_{\rm max}, \rho_s$, and we know how these parameters are related to c_{200}. This gives us the dependence on the concentration for these parameters, as compared to these parameters at the median concentration, as follows:

$$
\begin{aligned}
\log\left(\frac{v_{c,10}}{v_{c,10(\rm med)}}\right) &= d\left[q\left(1 - \left\{\frac{1-n}{\delta}\right\}\right) - \left\{\frac{q+1}{\delta}\right\}\right] \\
\log\left(\frac{\rho_{c,10}}{\rho_{c,10(\rm med)}}\right) &= 2d\left[-q\eta\left\{\frac{1-n}{\delta}\right\} + (\delta-\eta)\left\{\frac{q+1}{\delta}\right\}\right] \\
\log\left(\frac{M_{c,10}}{M_{c,10(\rm med)}}\right) &= d\left[q\left(3 + (\eta-3)\left\{\frac{1-n}{\delta}\right\}\right) - (3-\eta+\delta)\left\{\frac{q+1}{\delta}\right\}\right] \\
\log\left(\frac{M_{c,\rm RI}}{M_{c,\rm RI(med)}}\right) &= d\left[q\left(5 + (\eta-5)\left\{\frac{1-n}{\delta}\right\}\right) - (5-\eta+\delta)\left\{\frac{q+1}{\delta}\right\}\right] \\
\log\left(\frac{M_{c,\rm LS}}{M_{c,\rm LS(med)}}\right) &= d\left[q\left(3 - (3-2\eta)\left\{\frac{1-n}{\delta}\right\}\right) - (3-2\eta+\delta)\left\{\frac{q+1}{\delta}\right\}\right]
\end{aligned}
\tag{5.41}
$$

where here, $d = \pm 0.3$ for the spread in the concentration, $n = n_{c,0}$, δ is given by Eq. (5.23), we have set $\eta = \frac{\alpha}{\alpha-2}$ with $\alpha = 2.2$ being a good approximation and thus $\eta = 11$, $q = \frac{p}{2} - 1$

and $p = 2.4 - 2.6$ where the lower bound of c_{200} is $p = 2.4$, and the upper bound is $p = 2.6$ (but $p = 2.5$ is sufficient). This gives us the dependence on the concentration of the SMFP parameters *at fixed* M_{200}. One may also find the dependence on M_{200} by fixing c_{200}. For example, since $V_{\rm max} \propto M_{200}^{1/3} c_{200}^{p/2-1}$, we find that

$$\begin{aligned} \log\left(\frac{M_{c,\rm RI}}{M_{c,\rm RI(med)}}\right) &= \frac{1}{3}\left(5 + (\eta - 5)\left\{\frac{1-n}{\delta}\right\}\right) , \\ \log\left(\frac{M_{c,\rm LS}}{M_{c,\rm LS(med)}}\right) &= \frac{1}{3}\left(3 + (3 - 2\eta)\left\{\frac{n-1}{\delta}\right\}\right) , \end{aligned} \tag{5.42}$$

which easily explains the behavior we see in the left panel of Fig. 5.8 of the ratio $\frac{M_{c,\rm RI}}{M_{200}}$ where the $w = 1\,\mathrm{km/s}$ model (which has high n) appears to be relatively constant, and indeed this is because its dependence on M_{200} is such that $M_{c,\rm RI} \propto M_{200}$ as $n \to 3.7$, and closer to quadratic as $n \to 0$.

5.C Resolution

In this section, we discuss the numerical resolution issues encountered when probing the SMFP regime. In this regime, the central density increases drastically, while the core size shrinks significantly as well. This results in the core size becoming too small to be resolved late in the evolution. To address this while maintaining reasonable run times, we probe smaller radii than we did in O23 with some trade-off to maintain reasonable run times of the code, and increase the number of shells so as not to sacrifice the resolution of each profile. We also develop a method for finding where the central density is no longer resolved by finding the snapshot at which the core has become too small to resolve, and place a cutoff to exclude snapshots with profiles where the core can no longer be resolved.

5.C.1 Probing smaller radii and increasing shells

As halos evolve into the SMFP, the central density experiences a drastic increase while at the same time the size of the core shrinks significantly. This eventually will lead to the core shrinking to radii smaller than those we are probing. The solution is to examine smaller radii while maintaining reasonable run times. To accommodate this while maintaining reasonable run times for the code, we probed smaller radii in our runs ($\tilde{r}_{\rm min} = 0.005$ compared to $\tilde{r}_{\rm min} = 0.01$ in O23), and increased the resolution from 400 to 450 shells to ensure our shell resolution was not compromised.

Even with this increased resolution and probing smaller radii, the SMFP evolution will drive the cores of the halos to shrink beyond the resolution we set in our runs. The reason this becomes problematic is that we are not actually taking the density at the center of the halo ($r = 0$), and as such the central density ρ_c we obtain numerically is an approximation that depends on how small our innermost radial shell is. If the core of the halo is resolved, then the central region of the profile will be approximately flat, and thus our ρ_c can be trusted to be a good approximation. But as the core will shrink to a point where it can no longer be resolved, a test is required to ensure we only probe snapshots with resolved cores, and remove those that are not from the analysis.

5.C.2 Core resolution test

To address the issue of core resolution in our snapshots, we develop a test to determine whether or not the core is resolved, and thus, whether the approximate central density can be trusted. To do so we estimate the log-slope of the density profile at fixed mass $s[n] = (\ln(\rho[n+1]/\rho[n-1])/\ln(r[n+1]/r[n-1])$ from the $n+1$ and $n-1$ points. We place a stringent limit on the slope that determines when the snapshots are no longer resolved, such that if the slope at the nth point is steeper than -0.5, then we cannot assume the core

is resolved any longer and remove this and later snapshots from any analysis where the core density is required. We take n to be the fourth point in the density profile of a halo at each snapshot in time in order to avoid numerical artifacts in the initial points in the profile.

One of the quantities of interest for our analysis is the rate of change of the central density with the central velocity dispersion, i.e., $\gamma = d\ln(\rho_c)/d\ln(v_c)$. We estimate this as $\gamma_{\rm est}[n]$ using the density $\rho[n]$ and $v[n]$ at different snapshots in time. Note that the central velocity dispersion tends to a constant much faster than the density profile, and so $v[n]$ is close to v_c to a good approximation. Since our derivatives are computed at fixed mass, we can ascertain how good an approximation $\gamma_{\rm est}[n]$ is. Within the core, we can write $\rho[n] = \rho_c(1-(r[n]/r_c)^2)$ for $r[n] \ll r_c$, and this ansatz defines r_c. In this region, we write (approximately) the enclosed mass within $r[n]$ as $M[n] = (4\pi/3)\rho_c r[n]^3$. Within this set of approximations, we can show the following:

$$\gamma = \frac{\gamma_{\rm est}[n] - s[n]}{1 - s[n]/6}, \tag{5.43}$$

where $\gamma_{\rm est}[n]$ is shown in Fig. 5.1. By limiting to $s[n] > -0.5$, we can see that the error is only about 3.3% or less when $\gamma_{\rm est}[n] \approx 10$.

5.C.3 Stage 3 of the evolution

Stage 3, the region beyond the $\gamma = 10$ transition, cannot directly be obtained analytically. Because of this, we approximate the transition by selecting the minimum of the curve in Fig. 5.1 (left panel; diamonds correspond to the local minimum, which we call the $\gamma = 10$ transition). This is the point beyond which the slope begins to increase, during which the halos are in Stage 3. It is visible that the transition point is not where the curves reach the $\gamma = 10$ solution just yet; the models with weaker velocity dependence (or smaller n) take slightly longer to asymptote to the $\gamma = 10$ solution (i.e. Stage 3), as can be seen in the left

panel of Fig. 5.1. For smaller values of $n < 1$, we cannot numerically resolve much of Stage 3; in fact, these halos fall to $\gamma = 3$. However, for these models, we also observed that once in this $\gamma = 3$ region, the density of the shells just outside the core changes drastically from shell to shell; because the gravothermal equations have been discretized assuming changes from shell to shell are small, the results in this region cannot be trusted. We have also explicitly checked that in these cases where the halos fall to this $\gamma = 3$ region, energy is not conserved. This leads us to the conclusion that the $\gamma = 3$ region is numerical, and not an actual solution. It seems that the models with $n < 1$ suffer this issue because the core mass is the largest for these models. We hypothesize that numerical effects are larger for halos with larger cores (thus, those with models that have $n < 1$). A detailed analysis of this is beyond the scope of this paper, and we thus simply acknowledge that there are numerics involved here, but do not investigate further. We thus caution the reader that, for $n < 1$, we rely on assumptions and the evolution observed for the $n \geq 1$ cases, which indicate that the halos evolve to asymptote to the $\gamma = 10$ region in Stage 3.

Despite using the local minimum as the $\gamma = 10$ transition point (as opposed to, say, a point on the asymptote), we find that selecting $t_{\rm SMFP}(t_{10})$ scales the collapse times of the halos astonishingly well, as can be seen in the right panel of Fig. 5.3. Thus, this approximation works well enough to make predictions.

5.D Accuracy of Analytic Approximations

In this section, we discuss briefly our choice of using the analytic prediction for $v_{c,\rm LS}, \rho_{c,\rm LS}$ rather than our numerical results, we justify the truncation of the expansion of Eq. (5.6), we explain our definition of the mass at the transition from the LMFP to the SMFP regime, and we outline the use of a fitted function as an approximation in place of Eq. (5.4).

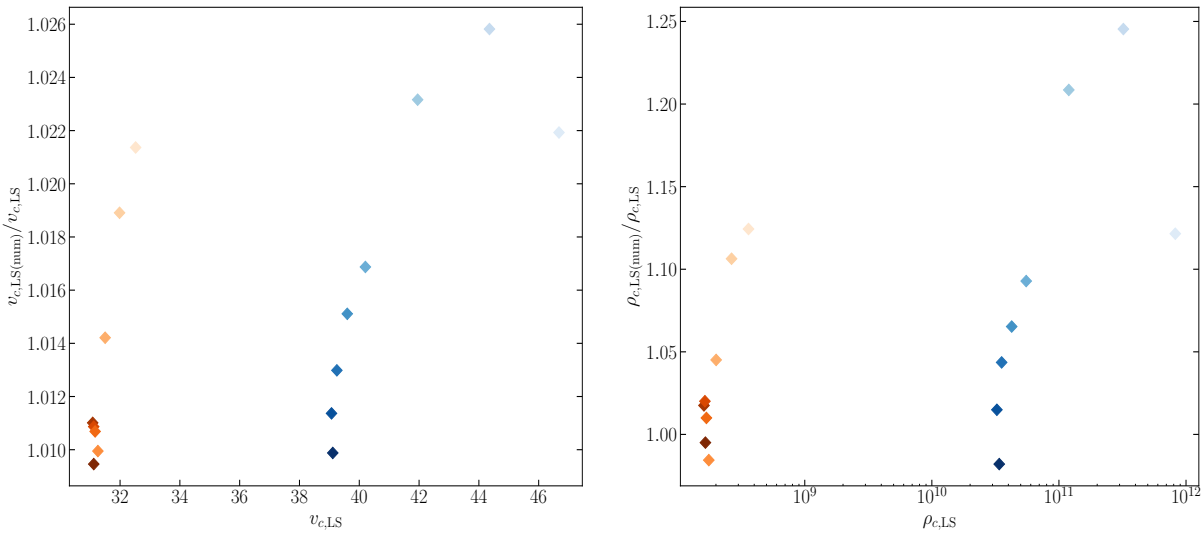

Figure 5.9: *(Left)* Comparison between the numerically obtained and analytically predicted central velocity at LS transition, plotted as a function of the analytic central velocity at the LS transition. The difference between them is very small, within $\sim 2.6\%$. *(Right)* Comparison between the numerically obtained and analytically predicted central density at LS transition, plotted as a function of the LS transition central density. Here the analytic and numerical values differ by at most $\sim 25\%$. It is unsurprising that the central density is a bit less accurate as it is the parameter that changes drastically.

A core aim of this paper is to provide a method to predict all parameters of a halo at both LS and $\gamma = 10$ transitions and black hole masses given only the initial halo parameters and the particle physics model used. To achieve this, it makes most sense to use the prediction for $v_{c,\mathrm{LS}}$ in Eq. (5.23) to show that the entirety of the halo evolution can be predicted without the need to solve the gravothermal equations. Comparing the numerically determined and theoretically predicted values, we find the $v_{c,\mathrm{LS}}$ prediction is within $\sim 2.6\%$ of the numerically determined value, while $\rho_{c,\mathrm{LS}}$ is within $\sim 25\%$, as seen in Fig. 5.9. The wider scatter in the central density can be attributed to the incredibly large changes it undergoes through the evolution. Given that the predictions agree with the numerical values to within 25%, we conclude that the analytic parameters are sufficiently close to the numerical values and use them throughout this work. In the case of the parameters at the $\gamma = 10$ transition, we use the numerically obtained values, followed by fitting a curve to provide an analytic method of obtaining the parameters.

Next, we justify the analytic approximation of our second order expansion in Eq. (5.6) and our choice for truncating the expansion of $K_{\rm eff}^{(2)}$ at the second order, where we show the difference between K_5 and $K_{\rm eff}^{(2)}$. One will note that the curves in Fig. 5.11 vary only slightly, and the largest variation occurs at high v_c when the halos are in the SMFP. As we said in subsection 5.2.1, the variation between K_5 and $K_{\rm eff}^{(2)}$ at second order is up to 20%, while the difference between the second order and the next expansion is only a sub percent correction. As seen in Fig. 5.11, the next order correction would not change the curves very much at all, thus truncating the expansion at second order is valid and sufficient.

Here, we discuss our definition of the mass that is roughly the maximum available for black hole growth. The mass within the LS transition radius (that is, the radius at which Eq. (5.10) is satisfied) as it evolves with time, $M_{\rm LS}$, is the mass of a halo that is within the SMFP regime. We conjecture that this would serve as an upper limit on the mass available for black hole growth. This is a mass that cannot be determined analytically. But we find that the core mass at the time the core transitions into the SMFP, $M_{c,\rm LS}$, offers a good approximation for this mass. This is desirable, as we can analytically determine the halo core properties at the LS transition using the relations derived in O23.

In Fig. 5.10, we plot both the ratio of the masses, $M_{\rm LS}/M_{c,\rm LS}$, and of the radius, $r_{\rm LS}/r_{c,\rm LS}$, as a function of the central velocity normalized by the central velocity at the LS transition. We also show the evolution of the mass profiles that are in the SMFP regime as a function of the kappa ratio $\frac{\kappa_{\rm SMFP}}{\kappa_{\rm LMFP}}$, and that are in Stage 3, for four cases that show a range in n and $\hat{\sigma}$ in Fig. 5.12. One can see that for higher n, generally the LS mass does not evolve as much as for lower n. In Fig. 5.10 we see that the ratio of the LS mass to the core mass at LS also tends to a constant in the later evolution in Stage 3 (the same is true for the radius). The ratio only differs by $\mathcal{O}(1)$, making the core mass at LS transition valid and more useful to use in place of the mass of a halo at the LS transition, as it can be determine analytically.

Finally, we mention the difference in the way we use Eq. (5.4) in the gravothermal code and in the analysis. In the gravothermal code, we used a fit approximation for the purpose of maintaining numerical stability. The approximation is given by

$$K_p \approx \left(1 + \frac{sp_0p_2}{1.5\log[1 + (sp_1)^{p_2}]}\right)^{-1/p_3}, \tag{5.44}$$

where we have set $s = x^4 + \varepsilon$ with $x = v/w$ and $\varepsilon = 10^{-8}$, and p_0, p_1, p_2, p_3 are just quantities from the fits that vary for different p. For $p = 3, 5, 7, 9$, we have, for (p_0, p_1, p_2, p_3), the following:

$$p = 3: \ (8, 0.339848, 0.37, 0.63),$$

$$p = 5: \ (24, 0.251115, 0.41, 0.71),$$

$$p = 7: \ (48, 0.682602, 0.42, 0.74),$$

$$p = 9: \ (80, 1.32953, 0.43, 0.76).$$

We find that the fitted approximation does very well compared to the exact form, as is shown in Fig. 5.13, where we plot the ratio of the exact form of K_p (Eq. (5.4)) to the approximation given in Eq. (5.44), both functions of v/w, plotted with respect to v/w. The fit differs from the exact form by at most 2%.

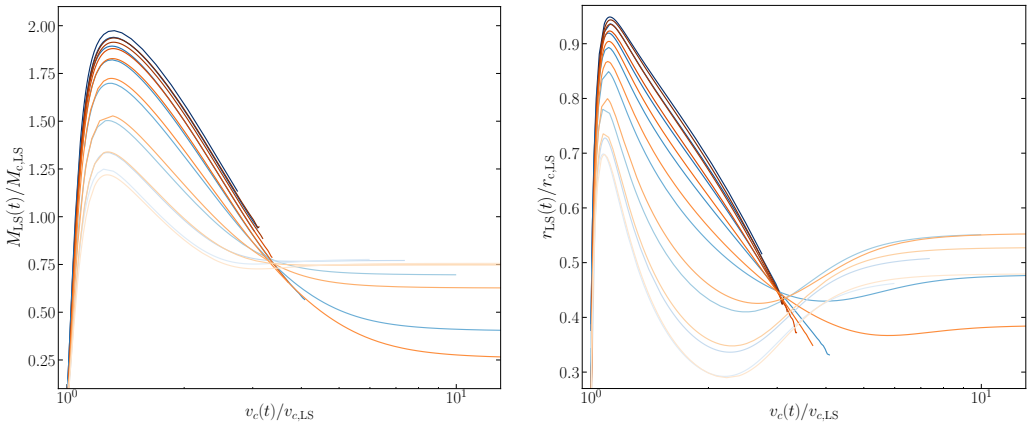

Figure 5.10: *(Left)* The LS transition mass normalized by the core mass at LS transition as a function of central velocity. *(Right)* The LS transition radius normalized by the core radius at LS transition as a function of central velocity.

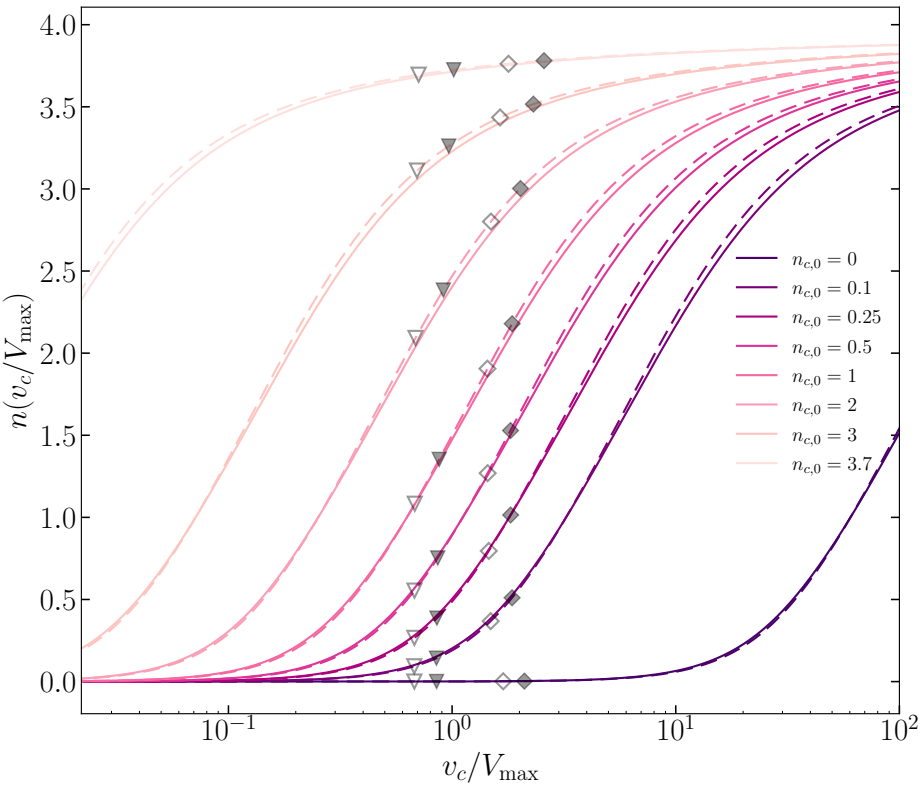

Figure 5.11: Plot of n as a function of v_c, plotted by holding the corresponding w constant for each curve. The triangles show the n_c and v_c for the LS transition, and the diamonds are for the $\gamma = 10$ transition, obtained analytically. In both cases, the solid markers are for runs 1-8 (lower $\hat{\sigma}$, and open markers for runs 9-16 (higher $\hat{\sigma}$), as shown in Table 5.2. The solid lines are plotted using K_5, while the dashed lines use $K^{(2)}_{\rm eff}$.

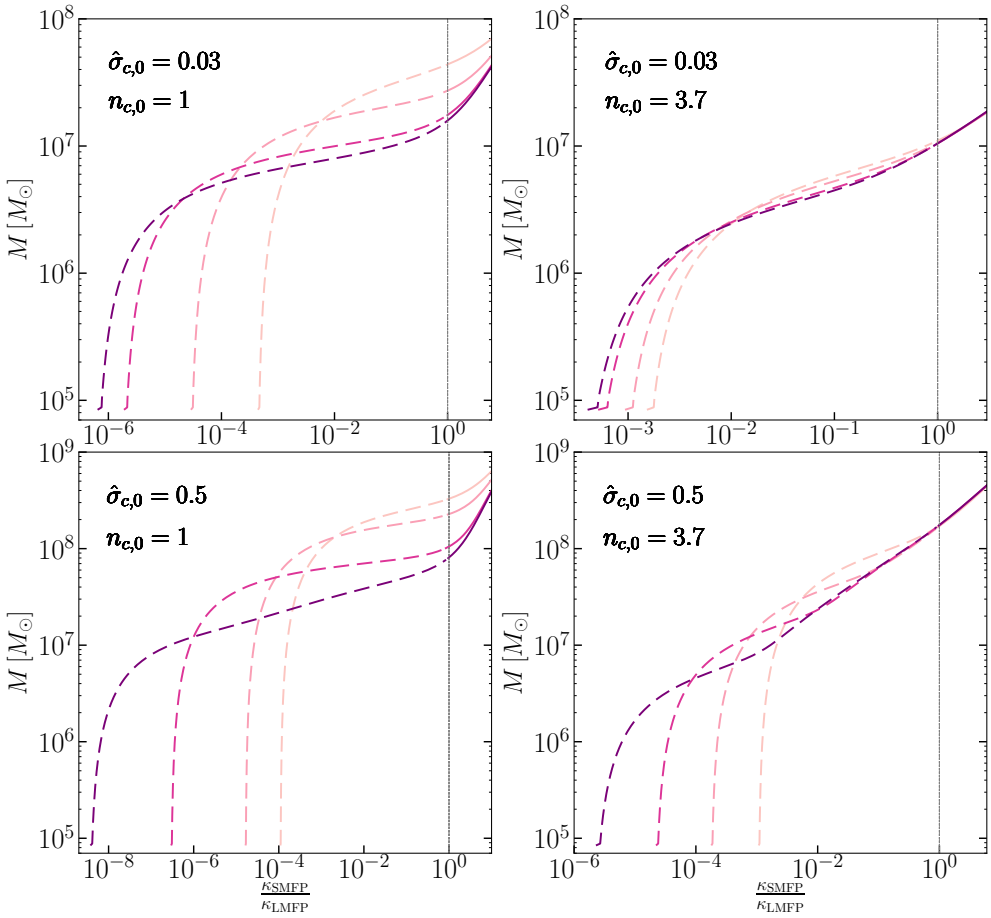

Figure 5.12: Mass at LS transition as a function of $\frac{\kappa_{\rm SMFP}}{\kappa_{\rm LMFP}}$ for 4 cases, corresponding to Runs 5, 8, 13, 16. The curves each correspond to profiles that are in Stage 3 of the evolution.

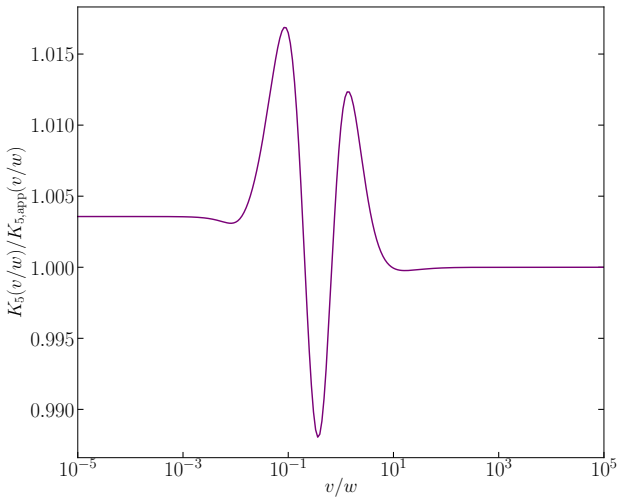

Figure 5.13: The ratio of the exact K_5 function as in Eq. (5.4) to the K_5 approximation given in Eq. (5.44) with respect to v/w. The functions differ by less than 2%.

Chapter 6

Conclusions

The ΛCDM paradigm has long been the cornerstone of our understanding of the large-scale structure in the universe. It offers robust predictions for phenomena such as the CMB anisotropies and large-scale distribution of galaxies. Its limitations on small scales, however, have catalyzed the exploration of alternative dark matter models, particularly igniting interest in the dark sector.

The SIDM model has emerged as a strong, viable contender for dark matter, elegantly reconciling discrepancies with observations by modifying halos only on small scales, while maintaining the successes of ΛCDM on large scales. A velocity-dependent cross-section for dark matter self-interactions is the keystone of this model, allowing for significant interactions within dwarf galaxies while remaining negligible in massive galaxy clusters. Moreover, the dark matter self-interactions lead the halo to undergo gravothermal evolution, culminating in core collapse on timescales shorter than the age of the universe.

In [92], we presented an intriguing study of the dark substructure in the gravitational lens SDSSJ0946+1006. Using observables such as the projected mass within the perturbation radius, and the slope of the projected density between 0.75–1.25 kpc, allowed for a

comparison to the CDM IllustrisTNG simulations. After examining the TNG100-1 simulations in both hydrodynamical and DMO, we found that the extreme concentration of this substructure is difficult to reconcile within a CDM universe.

In [124], we placed novel constraints on the cross section for both groups and clusters of galaxies. We examined adiabatic contractions and found that they are significant only for very small cross-sections. Having studied two mass scales allowed us to probe SIDM interactions at different collision velocities, revealing a preference for a velocity dependence in the interaction cross section.

In [106], we developed a new framework for the universal and self-similar solutions of SIDM halos undergoing gravothermal evolution in the LMFP regime, extending the framework to generic SIDM models with velocity-dependent cross sections. With this framework, we found that the universal behavior exhibited by our halos allows for determining the entire LMFP evolution of any halo.

In my latest first-author paper [58], I extended the study of gravothermal collapse of isolated SIDM halos deep into the SMFP regime. The SMFP is important to understand and characterize because evolution in this regime occurs on much more rapid timescales than in the LMFP, and this is the regime in which core collapse of dark matter halos may result in black hole formation. Our work unveiled, for the first time, a newfound SMFP universality through which we can characterize the entire SMFP evolution of halos. A significant achievement of this work is that we related the core properties in this new universal phase in the SMFP, to core characteristics in the LMFP. The LMFP core parameters can be analytically determined, as we showed in [106]. Having found a relation between the core properties in the LMFP and the SMFP, I devised a semi-analytic methodology to determine the core properties of halos deep in the SMFP, using only the initial NFW parameters and particle physics of any halo. Our semi-analytic model can potentially streamline the process of determining the core properties of halos in the SMFP, circumventing the need

for computationally demanding numerical methods. Furthermore, our semi-analytic model provides more accurate estimates of the minimum mass of the black holes that form from core collapse. The results of this work [58] coupled with our work in [106] allow for the prediction of the entire gravothermal evolution of any halo, from the LMFP to SMFP regime.

Looking ahead, I aim to further leverage simulations to probe the depths of SIDM and the potential formation of supermassive black holes (SMBH) within this framework. The potential for SIDM gravothermal collapse to elucidate the origins of SMBH seeds in the early universe is an exciting avenue for further exploration that may also provide a better understanding of the particle nature of dark matter. This research bridges the gap between particle physics and astrophysics, allowing us to learn about the particle properties of dark matter through astrophysical observations, while possibly solving the astrophysical mystery of the existence of SMBHs so early in the universe's history that it challenges our standard models of black hole growth.

Bibliography

[1] S. Adhikari, A. Banerjee, K. K. Boddy, F.-Y. Cyr-Racine, H. Desmond, C. Dvorkin, B. Jain, F. Kahlhoefer, M. Kaplinghat, A. Nierenberg, A. H. G. Peter, A. Robertson, J. Sakstein, and J. Zavala. Astrophysical tests of dark matter self-interactions, 2022.

[2] P. Agrawal, F.-Y. Cyr-Racine, L. Randall, and J. Scholtz. Make dark matter charged again. *Journal of Cosmology and Astroparticle Physics*, 2017(5):022, May 2017.

[3] K. Ahn and P. R. Shapiro. Formation and evolution of self-interacting dark matter haloes. *Monthly Notices of the Royal Astronomical Society*, 363(4):1092–1110, Nov. 2005.

[4] K. E. Andrade, Q. Minor, A. Nierenberg, and M. Kaplinghat. Detecting dark matter cores in galaxy clusters with strong lensing. *Monthly Notices of the Royal Astronomical Society*, 487(2):1905–1926, Aug 2019.

[5] E. Aprile, J. Aalbers, F. Agostini, M. Alfonsi, F. D. Amaro, M. Anthony, F. Arneodo, P. Barrow, L. Baudis, B. Bauermeister, M. L. Benabderrahmane, T. Berger, P. A. Breur, A. Brown, A. Brown, E. Brown, S. Bruenner, G. Bruno, R. Budnik, L. Bütikofer, J. Calvén, J. M. R. Cardoso, M. Cervantes, D. Cichon, D. Coderre, A. P. Colijn, J. Conrad, J. P. Cussonneau, M. P. Decowski, P. de Perio, P. di Gangi, A. di Giovanni, S. Diglio, G. Eurin, J. Fei, A. D. Ferella, A. Fieguth, W. Fulgione, A. Gallo Rosso, M. Galloway, F. Gao, M. Garbini, R. Gardner, C. Geis, L. W. Goetzke, L. Grandi, Z. Greene, C. Grignon, C. Hasterok, E. Hogenbirk, J. Howlett, R. Itay, B. Kaminsky, S. Kazama, G. Kessler, A. Kish, H. Landsman, R. F. Lang, D. Lellouch, L. Levinson, Q. Lin, S. Lindemann, M. Lindner, F. Lombardi, J. A. M. Lopes, A. Manfredini, I. Mariş, T. Marrodán Undagoitia, J. Masbou, F. V. Massoli, D. Masson, D. Mayani, M. Messina, K. Micheneau, A. Molinario, K. Morâ, M. Murra, J. Naganoma, K. Ni, U. Oberlack, P. Pakarha, B. Pelssers, R. Persiani, F. Piastra, J. Pienaar, V. Pizzella, M. C. Piro, G. Plante, N. Priel, L. Rauch, S. Reichard, C. Reuter, B. Riedel, A. Rizzo, S. Rosendahl, N. Rupp, R. Saldanha, J. M. F. Dos Santos, G. Sartorelli, M. Scheibelhut, S. Schindler, J. Schreiner, M. Schumann, L. Scotto Lavina, M. Selvi, P. Shagin, E. Shockley, M. Silva, H. Simgen, M. V. Sivers, A. Stein, S. Thapa, D. Thers, A. Tiseni, G. Trinchero, C. Tunnell, M. Vargas, N. Upole, H. Wang, Z. Wang, Y. Wei, C. Weinheimer, J. Wulf, J. Ye, Y. Zhang, T. Zhu, and Xenon Collaboration. First Dark Matter Search Results from the XENON1T Experiment. *Physical Review Letters*, 119(18):181301, Nov. 2017.

[6] Y. M. Bahé, D. J. Barnes, C. Dalla Vecchia, S. T. Kay, S. D. M. White, I. G. McCarthy, J. Schaye, R. G. Bower, R. A. Crain, T. Theuns, A. Jenkins, S. L. McGee, M. Schaller, P. A. Thomas, and J. W. Trayford. The Hydrangea simulations: galaxy formation in and around massive clusters. *Monthly Notices of the Royal Astronomical Society*, 470(4):4186–4208, Oct. 2017.

[7] S. Balberg and S. L. Shapiro. Gravothermal Collapse of Self-Interacting Dark Matter Halos and the Origin of Massive Black Holes. *Physical Review Letters*, 88(10):101301, Mar. 2002.

[8] S. Balberg, S. L. Shapiro, and S. Inagaki. Selfinteracting dark matter halos and the gravothermal catastrophe. *Astrophys. J.*, 568:475–487, 2002.

[9] E. A. Baltz, P. Marshall, and M. Oguri. Analytic models of plausible gravitational lens potentials. *Journal of Cosmology and Astroparticle Physics*, 1:015, Jan. 2009.

[10] A. Barnacka. Gravitational lenses as high-resolution telescopes. *Physics Report*, 778:1–46, Dec. 2018.

[11] D. J. Barnes, S. T. Kay, Y. M. Bahé, C. Dalla Vecchia, I. G. McCarthy, J. Schaye, R. G. Bower, A. Jenkins, P. A. Thomas, M. Schaller, R. A. Crain, T. Theuns, and S. D. M. White. The Cluster-EAGLE project: global properties of simulated clusters with resolved galaxies. *Monthly Notices of the Royal Astronomical Society*, 471(1):1088–1106, Oct. 2017.

[12] G. Bertone and D. Hooper. History of dark matter. *Reviews of Modern Physics*, 90(4):045002, Oct. 2018.

[13] G. Bertone, D. Hooper, and J. Silk. Particle dark matter: evidence, candidates and constraints. *Physics Report*, 405:279–390, Jan. 2004.

[14] J. Binney and S. Tremaine. *Galactic Dynamics*. Princeton University Press, 1988.

[15] G. R. Blumenthal, S. M. Faber, R. Flores, and J. R. Primack. Contraction of Dark Matter Galactic Halos Due to Baryonic Infall. *Astrophys. J.*, 301:27, 1986.

[16] K. K. Boddy, J. L. Feng, M. Kaplinghat, and T. M. P. Tait. Self-interacting dark matter from a non-Abelian hidden sector. *Physical Review D*, 89(11):115017, June 2014.

[17] K. K. Boddy, M. Kaplinghat, A. Kwa, and A. H. G. Peter. Hidden sector hydrogen as dark matter: Small-scale structure formation predictions and the importance of hyperfine interactions. *Physical Review D*, 94(12):123017, Dec. 2016.

[18] J. Bovy. *Dynamics and Astrophysics of Galaxies*. Princeton University Press, Princeton, NJ, 2023. In preparation.

[19] M. Boylan-Kolchin, J. S. Bullock, and M. Kaplinghat. Too big to fail? The puzzling darkness of massive Milky Way subhaloes. *Monthly Notices of the Royal Astronomical Society*, 415(1):L40–L44, July 2011.

[20] U. G. Briel and J. P. Henry. An X-ray temperature map of Coma. In A. Mazure, F. Casoli, F. Durret, and D. Gerbal, editors, *Untangling Coma Berenices: A New Vision of an Old Cluster*, page 170, Jan. 1998.

[21] M. R. Buckley and P. J. Fox. Dark matter self-interactions and light force carriers. *Physical Review D*, 81(8):083522, Apr. 2010.

[22] J. S. Bullock and M. Boylan-Kolchin. Small-Scale Challenges to the ΛCDM Paradigm. *Annual Review of Astronomy and Astrophysics*, 55(1):343–387, Aug. 2017.

[23] J. S. Bullock, T. S. Kolatt, Y. Sigad, R. S. Somerville, A. V. Kravtsov, A. A. Klypin, J. R. Primack, and A. Dekel. Profiles of dark haloes: evolution, scatter and environment. *Monthly Notices of the Royal Astronomical Society*, 321(3):559–575, Mar. 2001.

[24] S. G. Carlsten, J. E. Greene, A. H. G. Peter, J. P. Greco, and R. L. Beaton. Radial Distributions of Dwarf Satellite Systems in the Local Volume. *The Astrophysical Journal*, 902(2):124, Oct. 2020.

[25] S. Chapman, T. Cowling, D. Burnett, and C. Cercignani. *The Mathematical Theory of Non-uniform Gases: An Account of the Kinetic Theory of Viscosity, Thermal Conduction and Diffusion in Gases*. Cambridge Mathematical Library. Cambridge University Press, 1990.

[26] D. Clowe, M. Bradač, A. H. Gonzalez, M. Markevitch, S. W. Randall, C. Jones, and D. Zaritsky. A Direct Empirical Proof of the Existence of Dark Matter. *The Astrophysical Journal Letters*, 648(2):L109–L113, Sept. 2006.

[27] P. Colín, V. Avila-Reese, O. Valenzuela, and C. Firmani. Structure and Subhalo Population of Halos in a Self-interacting Dark Matter Cosmology. *The Astrophysical Journal*, 581(2):777–793, Dec. 2002.

[28] I. Collins, G. W. *The virial theorem in stellar astrophysics*. Pachart Publishing House, 1978.

[29] B. Colquhoun, S. Heeba, F. Kahlhoefer, L. Sagunski, and S. Tulin. Semiclassical regime for dark matter self-interactions. *Physical Review D*, 103(3):035006, Feb. 2021.

[30] A. B. Congdon and C. R. Keeton. *Principles of Gravitational Lensing: Light Deflection as a Probe of Astrophysics and Cosmology*. Springer, 2018.

[31] C. Conroy, P. G. van Dokkum, and A. Villaume. The Stellar Initial Mass Function in Early-type Galaxies from Absorption Line Spectroscopy. IV. A Super-Salpeter IMF in the Center of NGC 1407 from Non-parametric Models. *The Astrophysical Journal*, 837(2):166, Mar. 2017.

[32] J. Cooley, T. Lin, W. H. Lippincott, T. R. Slatyer, T.-T. Yu, D. S. Akerib, T. Aramaki, D. Baxter, T. Bringmann, R. Bunker, D. Carney, S. Cebrián, T. Y. Chen, P. Cushman, C. E. Dahl, R. Essig, A. Fan, R. Gaitskell, C. Galbiati, G. B. Gelmini, G. K. Giovanetti,

G. Giroux, L. Grandi, J. P. Harding, S. Haselschwardt, L. Hsu, S. Horiuchi, Y. Kahn, D. Kim, G.-B. Kim, S. Kravitz, V. A. Kudryavtsev, N. Kurinsky, R. F. Lang, R. K. Leane, B. V. Lehmann, C. Levy, S. Li, B. Loer, A. Manalaysay, C. J. Martoff, G. Mohlabeng, M. E. Monzani, A. S. J. Murphy, R. Neilson, H. N. Nelson, C. A. J. O'Hare, K. J. Palladino, A. Parikh, J.-C. Park, K. Perez, S. Profumo, N. Raj, B. M. Roach, T. Saab, M. Luísa Sarsa, R. Schnee, S. Shaw, S. Shin, K. Sinha, K. Stifter, A. Suzuki, M. Szydagis, T. M. P. Tait, V. Takhistov, Y.-D. Tsai, S. E. Vahsen, E. Vitagliano, P. von Doetinchem, G. Wang, S. Westerdale, D. A. Williams, X. Xiang, and L. Yang. Report of the Topical Group on Particle Dark Matter for Snowmass 2021. *arXiv e-prints*, page arXiv:2209.07426, Sept. 2022.

[33] C. A. Correa. Constraining velocity-dependent self-interacting dark matter with the milky way's dwarf spheroidal galaxies. *Monthly Notices of the Royal Astronomical Society*, 503(1):920–937, Feb 2021.

[34] F. Courbin, P. Saha, and P. L. Schechter. Quasar Lensing. In F. Courbin and D. Minniti, editors, *Gravitational Lensing: An Astrophysical Tool*, volume 608, page 1. Springer, 2002.

[35] W. J. G. de Blok. The Core-Cusp Problem. *Advances in Astronomy*, 2010:789293, Jan. 2010.

[36] W. J. G. de Blok, S. S. McGaugh, A. Bosma, and V. C. Rubin. Mass density profiles of low surface brightness galaxies. *The Astrophysical Journal*, 552(1):L23–L26, May 2001.

[37] G. Despali and S. Vegetti. The impact of baryonic physics on the subhalo mass function and implications for gravitational lensing. *ArXiv e-prints*, Aug. 2016.

[38] G. Despali, S. Vegetti, S. D. M. White, C. Giocoli, and F. C. van den Bosch. Modelling the line-of-sight contribution in substructure lensing. *Monthly Notices of the Royal Astronomical Society*, 475(4):5424–5442, Apr. 2018.

[39] B. Diemer. COLOSSUS: A Python Toolkit for Cosmology, Large-scale Structure, and Dark Matter Halos. *The Astrophysical Journal Supplement Series*, 239(2):35, Dec. 2018.

[40] B. Diemer and M. Joyce. An Accurate Physical Model for Halo Concentrations. *The Astrophysical Journal*, 871(2):168, Feb. 2019.

[41] B. Diemer and A. V. Kravtsov. A Universal Model for Halo Concentrations. *The Astrophysical Journal*, 799(1):108, Jan. 2015.

[42] S. Dodelson and F. Schmidt. *Modern Cosmology*. Academic Press, 2020.

[43] W. Du, C. Cheng, Z. Zheng, and H. Wu. Stellar Mass and Stellar Mass-to-light Ratio-Color Relations for Low Surface Brightness Galaxies. *The Astronomical Journal*, 159(4):138, Apr. 2020.

[44] J. Dubinski. The effect of dissipation on the shapes of dark halos. *The Astrophysical Journal*, 431:617, Aug 1994.

[45] A. R. Duffy, J. Schaye, S. T. Kay, and C. Dalla Vecchia. Dark matter halo concentrations in the Wilkinson Microwave Anisotropy Probe year 5 cosmology. *Monthly Notices of the Royal Astronomical Society*, 390(1):L64–L68, Oct. 2008.

[46] A. A. Dutton and A. V. Macciò. Cold dark matter haloes in the Planck era: evolution of structural parameters for Einasto and NFW profiles. *Monthly Notices of the Royal Astronomical Society*, 441(4):3359–3374, July 2014.

[47] O. D. Elbert, J. S. Bullock, S. Garrison-Kimmel, M. Rocha, J. Oñorbe, and A. H. G. Peter. Core formation in dwarf haloes with self-interacting dark matter: no fine-tuning necessary. *Monthly Notices of the Royal Astronomical Society*, 453(1):29–37, Oct. 2015.

[48] O. D. Elbert, J. S. Bullock, M. Kaplinghat, S. Garrison-Kimmel, A. S. Graus, and M. Rocha. A Testable Conspiracy: Simulating Baryonic Effects on Self-Interacting Dark Matter Halos. *Astrophys. J.*, 853(2):109, 2018.

[49] O. D. Elbert, J. S. Bullock, M. Kaplinghat, S. Garrison-Kimmel, A. S. Graus, and M. Rocha. A Testable Conspiracy: Simulating Baryonic Effects on Self-interacting Dark Matter Halos. *The Astrophysical Journal*, 853(2):109, Feb. 2018.

[50] R. Essig, S. D. McDermott, H.-B. Yu, and Y.-M. Zhong. Constraining Dissipative Dark Matter Self-Interactions. *Physical Review Letters*, 123(12):121102, Sept. 2019.

[51] B. Famaey and S. S. McGaugh. Modified Newtonian Dynamics (MOND): Observational Phenomenology and Relativistic Extensions. *Living Reviews in Relativity*, 15(1):10, Sept. 2012.

[52] S. G. Fedosin. The virial theorem and the kinetic energy of particles of a macroscopic system in the general field concept. *Continuum Mechanics and Thermodynamics*, 29(2):361–371, Mar. 2017.

[53] J. L. Feng. Dark Matter Candidates from Particle Physics and Methods of Detection. *Annual Review of Astronomy and Astrophysics*, 48:495–545, Sept. 2010.

[54] W.-X. Feng, H.-B. Yu, and Y.-M. Zhong. Seeding supermassive black holes with self-interacting dark matter: A unified scenario with baryons. *The Astrophysical Journal Letters*, 914(2):L26, Jun 2021.

[55] W.-X. Feng, H.-B. Yu, and Y.-M. Zhong. Dynamical instability of collapsed dark matter halos. *Journal of Cosmology and Astroparticle Physics*, 2022(5):036, May 2022.

[56] R. A. Flores and J. R. Primack. Observational and theoretical constraints on singular dark matter halos. *The Astrophysical Journal*, 427:L1, May 1994.

[57] K. Freese. Status of dark matter in the universe. *International Journal of Modern Physics D*, 26(6):1730012–223, Jan. 2017.

[58] S. Gad-Nasr, K. K. Boddy, M. Kaplinghat, N. J. Outmezguine, and L. Sagunski. On the late-time evolution of velocity-dependent self-interacting dark matter halos. To be submitted to MNRAS (will be on arXiv early December), 2023.

[59] R. Gavazzi, T. Treu, L. V. E. Koopmans, A. S. Bolton, L. A. Moustakas, S. Burles, and P. J. Marshall. The Sloan Lens ACS Survey. VI. Discovery and Analysis of a Double Einstein Ring. *The Astrophysical Journal*, 677(2):1046–1059, Apr 2008.

[60] M. Geha, T. M. Brown, J. Tumlinson, J. S. Kalirai, J. D. Simon, E. N. Kirby, D. A. Vand enBerg, R. R. Muñoz, R. J. Avila, P. Guhathakurta, and H. C. Ferguson. The Stellar Initial Mass Function of Ultra-faint Dwarf Galaxies: Evidence for IMF Variations with Galactic Environment. *The Astrophysical Journal*, 771(1):29, July 2013.

[61] M. Gennaro, M. Geha, K. Tchernyshyov, T. M. Brown, R. J. Avila, C. Conroy, R. R. Muñoz, J. D. Simon, and J. Tumlinson. The Initial Mass Function in the Coma Berenices Dwarf Galaxy from Deep Near-infrared HST Observations. *The Astrophysical Journal*, 863(1):38, Aug. 2018.

[62] G. Gentile, P. Salucci, U. Klein, D. Vergani, and P. Kalberla. The Cored distribution of dark matter in spiral galaxies. *Mon. Not. Roy. Astron. Soc.*, 351:903, 2004.

[63] S. Girmohanta and R. Shrock. Cross section calculations in theories of self-interacting dark matter. *Phys. Rev. D*, 106(6):063013, 2022.

[64] O. Y. Gnedin, D. Ceverino, N. Y. Gnedin, A. A. Klypin, A. V. Kravtsov, R. Levine, D. Nagai, and G. Yepes. Halo Contraction Effect in Hydrodynamic Simulations of Galaxy Formation. *Submitted to: Astrophys. J.*, 2011.

[65] O. Y. Gnedin, A. V. Kravtsov, A. A. Klypin, and D. Nagai. Response of dark matter halos to condensation of baryons: Cosmological simulations and improved adiabatic contraction model. *Astrophys. J.*, 616:16–26, 2004.

[66] D. Green, J. T. Ruderman, B. R. Safdi, J. Shelton, A. Achúcarro, P. Adshead, Y. Akrami, M. Baryakhtar, D. Baumann, A. Berlin, N. Blinov, K. K. Boddy, M. Buschmann, G. Cabass, R. Caldwell, E. Castorina, T. Y. Chen, X. Chen, W. Coulton, D. Croon, Y. Cui, D. Curtin, F.-Y. Cyr-Racine, C. Dessert, K. R. Dienes, P. Draper, P. Du, S. A. R. Ellis, R. Essig, R. Flauger, C. S. Fong, J. W. Foster, J. Fumagalli, K. Harigaya, S. Horiuchi, M. M. Ivanov, Y. Kahn, S. Knapen, R. K. Leane, H. Lee, E. W. Lentz, M. Lewandowski, M. Lisanti, A. J. Long, M. Loverde, A. Maleknejad, L. McAllister, S. D. McDermott, R. McGehee, P. D. Meerburg, J. Meyers, A. Moradinezhad Dizgah, M. Münchmeyer, N. J. Outmezguine, E. Pajer, G. A. Palma, A. Parikh, J.-C. Park, A. H. G. Peter, G. L. Pimentel, S. Renaux-Petel, N. L. Rodd, B. Shakya, G. Shiu, E. Silverstein, M. Simonovic, R. Singh, C. Sleight, V. Takhistov, P. Tanedo, M. Taronna, B. Thomas, N. Toro, Y.-D. Tsai, E. Vitagliano, M. Vogelsberger, B. Wallisch, B. D. Wandelt, R. H. Wechsler, C. Weniger, W. L. Kimmy Wu, W. L. Xu, M. Yamada, H.-B. Yu, Z. Zhang, Y.-M. Zhong, and K. Zurek.

Snowmass Theory Frontier: Astrophysics and Cosmology. *arXiv e-prints*, page arXiv:2209.06854, Sept. 2022.

[67] A. H. Guth. Inflationary universe: A possible solution to the horizon and flatness problems. *Physical Review D*, 23(2):347–356, Jan. 1981.

[68] D. W. Hogg. Distance measures in cosmology. *arXiv e-prints*, pages astro–ph/9905116, May 1999.

[69] M. Ibe and H.-B. Yu. Distinguishing dark matter annihilation enhancement scenarios via halo shapes. *Physics Letters B*, 692(2):70–73, Aug. 2010.

[70] F. Jiang, M. Kaplinghat, M. Lisanti, and O. Slone. Orbital evolution of satellite galaxies in self-interacting dark matter models, 2021.

[71] F. Kahlhoefer, M. Kaplinghat, T. R. Slatyer, and C.-L. Wu. Diversity in density profiles of self-interacting dark matter satellite halos. *Journal of Cosmology and Astroparticle Physics*, 2019(12):010–010, Dec 2019.

[72] A. Kamada, M. Kaplinghat, A. B. Pace, and H.-B. Yu. Self-Interacting Dark Matter Can Explain Diverse Galactic Rotation Curves. *Physical Review Letters*, 119(11):111102, Sept. 2017.

[73] M. Kaplinghat, R. E. Keeley, T. Linden, and H.-B. Yu. Tying Dark Matter to Baryons with Self-interactions. *Phys. Rev. Lett.*, 113:021302, 2014.

[74] M. Kaplinghat, S. Tulin, and H.-B. Yu. Direct detection portals for self-interacting dark matter. *Physical Review D*, 89(3):035009, Feb. 2014.

[75] M. Kaplinghat, S. Tulin, and H.-B. Yu. Dark Matter Halos as Particle Colliders: Unified Solution to Small-Scale Structure Puzzles from Dwarfs to Clusters. *Physical Review Letters*, 116(4):041302, Jan. 2016.

[76] M. Kaplinghat, M. Valli, and H.-B. Yu. Too big to fail in light of Gaia. *Monthly Notices of the Royal Astronomical Society*, 490(1):231–242, Nov. 2019.

[77] S. Kazantzidis, A. V. Kravtsov, A. R. Zentner, B. Allgood, D. Nagai, and B. Moore. The Effect of Gas Cooling on the Shapes of Dark Matter Halos. *The Astrophysical Journal Letters*, 611(2):L73–L76, Aug. 2004.

[78] S. Y. Kim and A. H. G. Peter. The Milky Way satellite velocity function is a sharp probe of small-scale structure problems. *arXiv e-prints*, page arXiv:2106.09050, June 2021.

[79] A. Klypin, A. V. Kravtsov, O. Valenzuela, and F. Prada. Where Are the Missing Galactic Satellites? *The Astrophysical Journal*, 522(1):82–92, Sept. 1999.

[80] A. A. Klypin, S. Trujillo-Gomez, and J. Primack. Dark Matter Halos in the Standard Cosmological Model: Results from the Bolshoi Simulation. *The Astrophysical Journal*, 740(2):102, Oct. 2011.

[81] J.-P. Kneib and P. Natarajan. Cluster lenses. *The Astronomy and Astrophysics Review*, 19:47, Nov. 2011.

[82] C. S. Kochanek and M. White. A Quantitative Study of Interacting Dark Matter in Halos. *The Astrophysical Journal*, 543(2):514–520, Nov. 2000.

[83] J. Koda and P. R. Shapiro. Gravothermal collapse of isolated self-interacting dark matter haloes: N-body simulation versus the fluid model. *Monthly Notices of the Royal Astronomical Society*, 415(2):1125–1137, Aug. 2011.

[84] R. Kuzio de Naray, S. S. McGaugh, W. J. G. de Blok, and A. Bosma. High-Resolution Optical Velocity Fields of 11 Low Surface Brightness Galaxies. *The Astrophysical Journal Supplement Series*, 165(2):461–479, Aug. 2006.

[85] R. Li, C. S. Frenk, S. Cole, Q. Wang, and L. Gao. Projection effects in the strong lensing study of subhaloes. *Monthly Notices of the Royal Astronomical Society*, 468:1426–1432, June 2017.

[86] A. R. Liddle. *An introduction to modern cosmology, Third Edition*. Wiley, 2015.

[87] A. Loeb and N. Weiner. Cores in Dwarf Galaxies from Dark Matter with a Yukawa Potential. *Physical Review Letters*, 106(17):171302, Apr. 2011.

[88] D. Lynden-Bell and P. P. Eggleton. On the consequences of the gravothermal catastrophe. *Monthly Notices of the Royal Astronomical Society*, 191:483–498, May 1980.

[89] D. Lynden-Bell and R. Wood. The Gravo-Thermal Catastrophe in Isothermal Spheres and the Onset of Red-Giant Structure for Stellar Systems. *Mon. Not. Roy. Astron. Soc.*, 138:495, 1968.

[90] N. F. Martin, J. T. A. de Jong, and H.-W. Rix. A Comprehensive Maximum Likelihood Analysis of the Structural Properties of Faint Milky Way Satellites. *The Astrophysical Journal*, 684(2):1075–1092, Sept. 2008.

[91] T. Meshveliani, J. Zavala, and M. R. Lovell. Gravothermal collapse of self-interacting dark matter halos as the origin of intermediate mass black holes in Milky Way satellites. *Physical Review D*, 107(8):083010, Apr. 2023.

[92] Q. Minor, S. Gad-Nasr, M. Kaplinghat, and S. Vegetti. An unexpected high concentration for the dark substructure in the gravitational lens SDSSJ0946+1006. *Monthly Notices of the Royal Astronomical Society*, 507(2):1662–1683, Oct. 2021.

[93] Q. E. Minor, M. Kaplinghat, and N. Li. A Robust Mass Estimator for Dark Matter Subhalo Perturbations in Strong Gravitational Lenses. *The Astrophysical Journal*, 845(2):118, Aug 2017.

[94] B. Moore, T. Quinn, F. Governato, J. Stadel, and G. Lake. Cold collapse and the core catastrophe. *Monthly Notices of the Royal Astronomical Society*, 310(4):1147–1152, Dec. 1999.

[95] J. A. Muñoz, C. S. Kochanek, and C. R. Keeton. Cusped Mass Models of Gravitational Lenses. *The Astrophysical Journal*, 558:657–665, Sept. 2001.

[96] V. F. Mukhanov, H. A. Feldman, and R. H. Brandenberger. Theory of cosmological perturbations. *Physics Report*, 215(5-6):203–333, June 1992.

[97] J. F. Navarro, C. S. Frenk, and S. D. M. White. The Structure of Cold Dark Matter Halos. *The Astrophysical Journal*, 462:563, May 1996.

[98] J. F. Navarro, C. S. Frenk, and S. D. M. White. A Universal Density Profile from Hierarchical Clustering. *The Astrophysical Journal*, 490(2):493–508, Dec. 1997.

[99] D. Nelson, V. Springel, A. Pillepich, V. Rodriguez-Gomez, P. Torrey, S. Genel, M. Vogelsberger, R. Pakmor, F. Marinacci, R. Weinberger, L. Kelley, M. Lovell, B. Diemer, and L. Hernquist. The IllustrisTNG simulations: public data release. *Computational Astrophysics and Cosmology*, 6(1):2, May 2019.

[100] A. B. Newman, R. S. Ellis, and T. Treu. Luminous and Dark Matter Profiles from Galaxies to Clusters: Bridging the Gap with Group-scale Lenses. *The Astrophysical Journal*, 814(1):26, Nov. 2015.

[101] A. B. Newman, T. Treu, R. S. Ellis, and D. J. Sand. The Density Profiles of Massive, Relaxed Galaxy Clusters. II. Separating Luminous and Dark Matter in Cluster Cores. *The Astrophysical Journal*, 765(1):25, Mar. 2013.

[102] A. B. Newman, T. Treu, R. S. Ellis, D. J. Sand, C. Nipoti, J. Richard, and E. Jullo. The Density Profiles of Massive, Relaxed Galaxy Clusters. I. The Total Density Over Three Decades in Radius. *The Astrophysical Journal*, 765(1):24, Mar. 2013.

[103] H. Nishikawa, K. K. Boddy, and M. Kaplinghat. Accelerated core collapse in tidally stripped self-interacting dark matter halos. *Physical Review D*, 101(6):063009, Mar. 2020.

[104] S.-H. Oh, W. J. G. de Blok, E. Brinks, F. Walter, and R. C. Kennicutt. Dark and luminous matter in things dwarf galaxies. *The Astronomical Journal*, 141(6):193, May 2011.

[105] K. A. Oman, J. F. Navarro, A. Fattahi, C. S. Frenk, T. Sawala, S. D. M. White, R. Bower, R. A. Crain, M. Furlong, M. Schaller, J. Schaye, and T. Theuns. The unexpected diversity of dwarf galaxy rotation curves. *Monthly Notices of the Royal Astronomical Society*, 452(4):3650–3665, Oct. 2015.

[106] N. J. Outmezguine, K. K. Boddy, S. Gad-Nasr, M. Kaplinghat, and L. Sagunski. Universal gravothermal evolution of isolated self-interacting dark matter halos for velocity-dependent cross sections. *Monthly Notices of the Royal Astronomical Society*, June 2023.

[107] E. Papastergis, R. Giovanelli, M. P. Haynes, and F. Shankar. Is there a "too big to fail" problem in the field? *Astronomy and Astrophysics*, 574:A113, Feb. 2015.

[108] D. Paraficz, J. P. Kneib, J. Richard, A. Morandi, M. Limousin, E. Jullo, and J. Martinez. The Bullet cluster at its best: weighing stars, gas, and dark matter. *Astronomy and Astrophysics*, 594:A121, Oct. 2016.

[109] A. H. G. Peter, M. Rocha, J. S. Bullock, and M. Kaplinghat. Cosmological simulations with self-interacting dark matter - II. Halo shapes versus observations. *Monthly Notices of the Royal Astronomical Society*, 430(1):105–120, Mar. 2013.

[110] L. Pitaevskii and E. Lifshitz. *Physical Kinetics*. Elsevier Science, 2012.

[111] Planck Collaboration, N. Aghanim, Y. Akrami, M. Ashdown, J. Aumont, C. Baccigalupi, M. Ballardini, A. J. Banday, R. B. Barreiro, N. Bartolo, S. Basak, R. Battye, K. Benabed, J. P. Bernard, M. Bersanelli, P. Bielewicz, J. J. Bock, J. R. Bond, J. Borrill, F. R. Bouchet, F. Boulanger, M. Bucher, C. Burigana, R. C. Butler, E. Calabrese, J. F. Cardoso, J. Carron, A. Challinor, H. C. Chiang, J. Chluba, L. P. L. Colombo, C. Combet, D. Contreras, B. P. Crill, F. Cuttaia, P. de Bernardis, G. de Zotti, J. Delabrouille, J. M. Delouis, E. Di Valentino, J. M. Diego, O. Doré, M. Douspis, A. Ducout, X. Dupac, S. Dusini, G. Efstathiou, F. Elsner, T. A. Enßlin, H. K. Eriksen, Y. Fantaye, M. Farhang, J. Fergusson, R. Fernandez-Cobos, F. Finelli, F. Forastieri, M. Frailis, A. A. Fraisse, E. Franceschi, A. Frolov, S. Galeotta, S. Galli, K. Ganga, R. T. Génova-Santos, M. Gerbino, T. Ghosh, J. González-Nuevo, K. M. Górski, S. Gratton, A. Gruppuso, J. E. Gudmundsson, J. Hamann, W. Handley, F. K. Hansen, D. Herranz, S. R. Hildebrandt, E. Hivon, Z. Huang, A. H. Jaffe, W. C. Jones, A. Karakci, E. Keihänen, R. Keskitalo, K. Kiiveri, J. Kim, T. S. Kisner, L. Knox, N. Krachmalnicoff, M. Kunz, H. Kurki-Suonio, G. Lagache, J. M. Lamarre, A. Lasenby, M. Lattanzi, C. R. Lawrence, M. Le Jeune, P. Lemos, J. Lesgourgues, F. Levrier, A. Lewis, M. Liguori, P. B. Lilje, M. Lilley, V. Lindholm, M. López-Caniego, P. M. Lubin, Y. Z. Ma, J. F. Macías-Pérez, G. Maggio, D. Maino, N. Mandolesi, A. Mangilli, A. Marcos-Caballero, M. Maris, P. G. Martin, M. Martinelli, E. Martínez-González, S. Matarrese, N. Mauri, J. D. McEwen, P. R. Meinhold, A. Melchiorri, A. Mennella, M. Migliaccio, M. Millea, S. Mitra, M. A. Miville-Deschênes, D. Molinari, L. Montier, G. Morgante, A. Moss, P. Natoli, H. U. Nørgaard-Nielsen, L. Pagano, D. Paoletti, B. Partridge, G. Patanchon, H. V. Peiris, F. Perrotta, V. Pettorino, F. Piacentini, L. Polastri, G. Polenta, J. L. Puget, J. P. Rachen, M. Reinecke, M. Remazeilles, A. Renzi, G. Rocha, C. Rosset, G. Roudier, J. A. Rubiño-Martín, B. Ruiz-Granados, L. Salvati, M. Sandri, M. Savelainen, D. Scott, E. P. S. Shellard, C. Sirignano, G. Sirri, L. D. Spencer, R. Sunyaev, A. S. Suur-Uski, J. A. Tauber, D. Tavagnacco, M. Tenti, L. Toffolatti, M. Tomasi, T. Trombetti, L. Valenziano, J. Valiviita, B. Van Tent, L. Vibert, P. Vielva, F. Villa, N. Vittorio, B. D. Wandelt, I. K. Wehus, M. White, S. D. M. White, A. Zacchei, and A. Zonca. Planck 2018 results. VI. Cosmological parameters. *Astronomy and Astrophysics*, 641:A6, Sept. 2020.

[112] J. Pollack, D. N. Spergel, and P. J. Steinhardt. Supermassive Black Holes from Ultra-strongly Self-interacting Dark Matter. *The Astrophysical Journal*, 804(2):131, May 2015.

[113] S. W. Randall, M. Markevitch, D. Clowe, A. H. Gonzalez, and M. Bradac. Constraints on the Self-Interaction Cross-Section of Dark Matter from Numerical Simulations of the Merging Galaxy Cluster 1E 0657-56. *Astrophys. J.*, 679:1173–1180, 2008.

[114] J. I. Read, M. G. Walker, and P. Steger. The case for a cold dark matter cusp in Draco. *Monthly Notices of the Royal Astronomical Society*, 481(1):860–877, Nov. 2018.

[115] D. Reed, F. Governato, L. Verde, J. Gardner, T. Quinn, J. Stadel, D. Merritt, and G. Lake. Evolution of the density profiles of dark matter haloes. *Monthly Notices of the Royal Astronomical Society*, 357(1):82–96, Feb. 2005.

[116] J. D. Remolina González, K. Sharon, B. Reed, N. Li, G. Mahler, L. E. Bleem, M. Gladders, A. Niemiec, A. Acebron, and H. Child. Efficient Mass Estimate at the Core of Strong Lensing Galaxy Clusters Using the Einstein Radius. *The Astrophysical Journal*, 902(1):44, Oct. 2020.

[117] T. Ren, A. Kwa, M. Kaplinghat, and H.-B. Yu. Reconciling the Diversity and Uniformity of Galactic Rotation Curves with Self-Interacting Dark Matter. *Physical Review X*, 9(3):031020, July 2019.

[118] A. Robertson et al. The diverse density profiles of galaxy clusters with self-interacting dark matter plus baryons. *Mon. Not. Roy. Astron. Soc.*, 476(1):L20–L24, 2018.

[119] A. Robertson, R. Massey, and V. Eke. Cosmic particle colliders: simulations of self-interacting dark matter with anisotropic scattering. *Monthly Notices of the Royal Astronomical Society*, 467(4):4719–4730, June 2017.

[120] V. H. Robles, T. Kelley, J. S. Bullock, and M. Kaplinghat. The Milky Way's halo and subhaloes in self-interacting dark matter. *Monthly Notices of the Royal Astronomical Society*, 490(2):2117–2123, Dec. 2019.

[121] M. Rocha, A. H. G. Peter, J. S. Bullock, M. Kaplinghat, S. Garrison-Kimmel, J. Oñorbe, and L. A. Moustakas. Cosmological simulations with self-interacting dark matter - I. Constant-density cores and substructure. *Monthly Notices of the Royal Astronomical Society*, 430(1):81–104, Mar. 2013.

[122] V. C. Rubin and J. Ford, W. Kent. Rotation of the Andromeda Nebula from a Spectroscopic Survey of Emission Regions. *The Astrophysical Journal*, 159:379, Feb. 1970.

[123] B. Ryden. *Introduction to cosmology*. Cambridge University Press, 2003.

[124] L. Sagunski, S. Gad-Nasr, B. Colquhoun, A. Robertson, and S. Tulin. Velocity-dependent self-interacting dark matter from groups and clusters of galaxies. *Journal of Cosmology and Astroparticle Physics*, 2021(1):024, Jan. 2021.

[125] P. Salucci. The distribution of dark matter in galaxies. *Astron. Astrophys. Rev.*, 27(1):2, 2019.

[126] O. Sameie, P. Creasey, H.-B. Yu, L. V. Sales, M. Vogelsberger, and J. Zavala. The impact of baryonic discs on the shapes and profiles of self-interacting dark matter haloes. *Monthly Notices of the Royal Astronomical Society*, 479(1):359–367, Sept. 2018.

[127] P. Schneider. Part 1: Introduction to gravitational lensing and cosmology. In G. Meylan, P. Jetzer, P. North, P. Schneider, C. S. Kochanek, and J. Wambsganss, editors, *Saas-Fee Advanced Course 33: Gravitational Lensing: Strong, Weak and Micro*, pages 1–89. Springer, Jan. 2006.

[128] P. Schneider, J. Ehlers, and E. E. Falco. *Gravitational Lenses*. Springer, 1992.

[129] M. Sereno, C. Giocoli, S. Ettori, and L. Moscardini. The mass–concentration relation in lensing clusters: the role of statistical biases and selection effects. *Mon. Not. Roy. Astron. Soc.*, 449(2):2024–2039, 2015.

[130] M. Silverman, J. S. Bullock, M. Kaplinghat, V. H. Robles, and M. Valli. Motivations for a large self-interacting dark matter cross-section from Milky Way satellites. *Monthly Notices of the Royal Astronomical Society*, 518(2):2418–2435, Jan. 2023.

[131] J. Smolinsky and P. Tanedo. Dark photons from captured inelastic dark matter annihilation: Charged particle signatures. *Physical Review D*, 95(7):075015, Apr. 2017.

[132] A. Sonnenfeld, T. Treu, R. Gavazzi, P. J. Marshall, M. W. Auger, S. H. Suyu, L. V. E. Koopmans, and A. S. Bolton. Evidence for Dark Matter Contraction and a Salpeter Initial Mass Function in a Massive Early-type Galaxy. *The Astrophysical Journal*, 752(2):163, Jun 2012.

[133] L. S. Sparke and I. Gallagher, John S. *Galaxies in the Universe: An Introduction*. Cambridge University Press, 2007.

[134] D. N. Spergel and P. J. Steinhardt. Observational evidence for self-interacting cold dark matter. *Physical Review Letters*, 84(17):3760–3763, Apr 2000.

[135] D. N. Spergel, L. Verde, H. V. Peiris, E. Komatsu, M. R. Nolta, C. L. Bennett, M. Halpern, G. Hinshaw, N. Jarosik, A. Kogut, M. Limon, S. S. Meyer, L. Page, G. S. Tucker, J. L. Weiland, E. Wollack, and E. L. Wright. First-Year Wilkinson Microwave Anisotropy Probe (WMAP) Observations: Determination of Cosmological Parameters. *The Astrophysical Journal Supplement Series*, 148(1):175–194, Sept. 2003.

[136] L. Spitzer. *Dynamical evolution of globular clusters*. Princeton University Press, 1987.

[137] V. Springel, S. D. M. White, A. Jenkins, C. S. Frenk, N. Yoshida, L. Gao, J. Navarro, R. Thacker, D. Croton, J. Helly, J. A. Peacock, S. Cole, P. Thomas, H. Couchman, A. Evrard, J. Colberg, and F. Pearce. Simulations of the formation, evolution and clustering of galaxies and quasars. *Nature*, 435(7042):629–636, June 2005.

[138] Y.-D. Tsai, R. McGehee, and H. Murayama. Resonant Self-Interacting Dark Matter from Dark QCD. *Physical Review Letters*, 128(17):172001, Apr. 2022.

[139] S. Tulin and H.-B. Yu. Dark matter self-interactions and small scale structure. *Physics Report*, 730:1–57, Feb. 2018.

[140] S. Tulin, H.-B. Yu, and K. M. Zurek. Beyond collisionless dark matter: Particle physics dynamics for dark matter halo structure. *Physical Review D*, 87(11):115007, June 2013.

[141] H. C. Turner, M. R. Lovell, J. Zavala, and M. Vogelsberger. The onset of gravothermal core collapse in velocity-dependent self-interacting dark matter subhaloes. *Monthly Notices of the Royal Astronomical Society*, 505(4):5327–5339, Jun 2021.

[142] K. Umetsu. Cluster Weak Gravitational Lensing. *arXiv e-prints*, page arXiv:1002.3952, Feb. 2010.

[143] M. Valli and H.-B. Yu. Dark matter self-interactions from the internal dynamics of dwarf spheroidals. *Nature Astronomy*, 2(11):907–912, Aug 2018.

[144] S. Vegetti, L. V. E. Koopmans, A. Bolton, T. Treu, and R. Gavazzi. Detection of a dark substructure through gravitational imaging. *Monthly Notices of the Royal Astronomical Society*, 408:1969–1981, Nov. 2010.

[145] M. Vogelsberger, J. Zavala, F.-Y. Cyr-Racine, C. Pfrommer, T. Bringmann, and K. Sigurdson. ETHOS - an effective theory of structure formation: dark matter physics as a possible explanation of the small-scale CDM problems. *Monthly Notices of the Royal Astronomical Society*, 460(2):1399–1416, Aug. 2016.

[146] M. Vogelsberger, J. Zavala, and A. Loeb. Subhaloes in self-interacting galactic dark matter haloes. *Monthly Notices of the Royal Astronomical Society*, 423(4):3740–3752, July 2012.

[147] R. H. Wechsler, J. S. Bullock, J. R. Primack, A. V. Kravtsov, and A. Dekel. Concentrations of Dark Halos from Their Assembly Histories. *The Astrophysical Journal*, 568(1):52–70, Mar. 2002.

[148] D. H. Weinberg, J. S. Bullock, F. Governato, R. Kuzio de Naray, and A. H. G. Peter. Cold dark matter: Controversies on small scales. *Proceedings of the National Academy of Science*, 112(40):12249–12255, Oct. 2015.

[149] J. Woo, S. Courteau, and A. Dekel. Scaling relations and the fundamental line of the local group dwarf galaxies. *Monthly Notices of the Royal Astronomical Society*, 390(4):1453–1469, Nov. 2008.

[150] R. L. Workman, V. D. Burkert, V. Crede, E. Klempt, U. Thoma, L. Tiator, K. Agashe, G. Aielli, B. C. Allanach, C. Amsler, M. Antonelli, E. C. Aschenauer, D. M. Asner, H. Baer, S. Banerjee, R. M. Barnett, L. Baudis, C. W. Bauer, J. J. Beatty, V. I. Belousov, J. Beringer, A. Bettini, O. Biebel, K. M. Black, E. Blucher, R. Bonventre, V. V. Bryzgalov, O. Buchmuller, M. A. Bychkov, R. N. Cahn, M. Carena, A. Ceccucci, A. Cerri, R. S. Chivukula, G. Cowan, K. Cranmer, O. Cremonesi, G. D'Ambrosio, T. Damour, D. de Florian, A. de Gouvêa, T. DeGrand, P. de Jong, S. Demers, B. A.

Dobrescu, M. D'Onofrio, M. Doser, H. K. Dreiner, P. Eerola, U. Egede, S. Eidelman, A. X. El-Khadra, J. Ellis, S. C. Eno, J. Erler, V. V. Ezhela, W. Fetscher, B. D. Fields, A. Freitas, H. Gallagher, Y. Gershtein, T. Gherghetta, M. C. Gonzalez-Garcia, M. Goodman, C. Grab, A. V. Gritsan, C. Grojean, D. E. Groom, M. Grünewald, A. Gurtu, T. Gutsche, H. E. Haber, M. Hamel, C. Hanhart, S. Hashimoto, Y. Hayato, A. Hebecker, S. Heinemeyer, J. J. Hernández-Rey, K. Hikasa, J. Hisano, A. Höcker, J. Holder, L. Hsu, J. Huston, T. Hyodo, A. Ianni, M. Kado, M. Karliner, U. F. Katz, M. Kenzie, V. A. Khoze, S. R. Klein, F. Krauss, M. Kreps, P. Križan, B. Krusche, Y. Kwon, O. Lahav, J. Laiho, L. P. Lellouch, J. Lesgourgues, A. R. Liddle, Z. Ligeti, C. J. Lin, C. Lippmann, T. M. Liss, L. Littenberg, C. Lourenço, K. S. Lugovsky, S. B. Lugovsky, A. Lusiani, Y. Makida, F. Maltoni, T. Mannel, A. V. Manohar, W. J. Marciano, A. Masoni, J. Matthews, U. G. Meißner, I. A. Melzer-Pellmann, M. Mikhasenko, D. J. Miller, D. Milstead, R. E. Mitchell, K. Mönig, P. Molaro, F. Moortgat, M. Moskovic, K. Nakamura, M. Narain, P. Nason, S. Navas, A. Nelles, M. Neubert, P. Nevski, Y. Nir, K. A. Olive, C. Patrignani, J. A. Peacock, V. A. Petrov, E. Pianori, A. Pich, A. Piepke, F. Pietropaolo, A. Pomarol, S. Pordes, S. Profumo, A. Quadt, K. Rabbertz, J. Rademacker, G. Raffelt, M. Ramsey-Musolf, B. N. Ratcliff, P. Richardson, A. Ringwald, D. J. Robinson, S. Roesler, S. Rolli, A. Romaniouk, L. J. Rosenberg, J. L. Rosner, G. Rybka, M. G. Ryskin, R. A. Ryutin, Y. Sakai, S. Sarkar, F. Sauli, O. Schneider, S. Schönert, K. Scholberg, A. J. Schwartz, J. Schwiening, D. Scott, F. Sefkow, U. Seljak, V. Sharma, S. R. Sharpe, V. Shiltsev, G. Signorelli, M. Silari, F. Simon, T. Sjöstrand, P. Skands, T. Skwarnicki, G. F. Smoot, A. Soffer, M. S. Sozzi, S. Spanier, C. Spiering, A. Stahl, S. L. Stone, Y. Sumino, M. J. Syphers, F. Takahashi, M. Tanabashi, J. Tanaka, M. Taševský, K. Terao, K. Terashi, J. Terning, R. S. Thorne, M. Titov, N. P. Tkachenko, D. R. Tovey, K. Trabelsi, P. Urquijo, G. Valencia, R. Van de Water, N. Varelas, G. Venanzoni, L. Verde, I. Vivarelli, P. Vogel, W. Vogelsang, V. Vorobyev, S. P. Wakely, W. Walkowiak, C. W. Walter, D. Wands, D. H. Weinberg, E. J. Weinberg, N. Wermes, M. White, L. R. Wiencke, S. Willocq, C. G. Wohl, C. L. Woody, W. M. Yao, M. Yokoyama, R. Yoshida, G. Zanderighi, G. P. Zeller, O. V. Zenin, R. Y. Zhu, S.-L. Zhu, F. Zimmermann, P. A. Zyla, and Particle Data Group. Review of Particle Physics. *Progress of Theoretical and Experimental Physics*, 2022(8):083C01, Aug. 2022.

[151] H. Xiao, X. Shen, P. F. Hopkins, and K. M. Zurek. SMBH seeds from dissipative dark matter. *Journal of Cosmology and Astroparticle Physics*, 2021(7):039, July 2021.

[152] D. D. Xu, S. Mao, A. P. Cooper, L. Gao, C. S. Frenk, R. E. Angulo, and J. Helly. On the effects of line-of-sight structures on lensing flux-ratio anomalies in a ΛCDM universe. *Monthly Notices of the Royal Astronomical Society*, 421(3):2553–2567, Apr. 2012.

[153] D. Yang and H.-B. Yu. Gravothermal evolution of dark matter halos with differential elastic scattering. *Journal of Cosmology and Astroparticle Physics*, 2022(9):077, Sept. 2022.

[154] S. Yang, X. Du, Z. C. Zeng, A. Benson, F. Jiang, E. O. Nadler, and A. H. G. Peter. Gravothermal Solutions of SIDM Halos: Mapping from Constant to Velocity-dependent Cross Section. *The Astrophysical Journal*, 946(1):47, Mar. 2023.

[155] D. G. York, J. Adelman, J. Anderson, John E., S. F. Anderson, J. Annis, N. A. Bahcall, J. A. Bakken, R. Barkhouser, S. Bastian, E. Berman, W. N. Boroski, S. Bracker, C. Briegel, J. W. Briggs, J. Brinkmann, R. Brunner, S. Burles, L. Carey, M. A. Carr, F. J. Castander, B. Chen, P. L. Colestock, A. J. Connolly, J. H. Crocker, I. Csabai, P. C. Czarapata, J. E. Davis, M. Doi, T. Dombeck, D. Eisenstein, N. Ellman, B. R. Elms, M. L. Evans, X. Fan, G. R. Federwitz, L. Fiscelli, S. Friedman, J. A. Frieman, M. Fukugita, B. Gillespie, J. E. Gunn, V. K. Gurbani, E. de Haas, M. Haldeman, F. H. Harris, J. Hayes, T. M. Heckman, G. S. Hennessy, R. B. Hindsley, S. Holm, D. J. Holmgren, C.-h. Huang, C. Hull, D. Husby, S.-I. Ichikawa, T. Ichikawa, Ž. Ivezić, S. Kent, R. S. J. Kim, E. Kinney, M. Klaene, A. N. Kleinman, S. Kleinman, G. R. Knapp, J. Korienek, R. G. Kron, P. Z. Kunszt, D. Q. Lamb, B. Lee, R. F. Leger, S. Limmongkol, C. Lindenmeyer, D. C. Long, C. Loomis, J. Loveday, R. Lucinio, R. H. Lupton, B. MacKinnon, E. J. Mannery, P. M. Mantsch, B. Margon, P. McGehee, T. A. McKay, A. Meiksin, A. Merelli, D. G. Monet, J. A. Munn, V. K. Narayanan, T. Nash, E. Neilsen, R. Neswold, H. J. Newberg, R. C. Nichol, T. Nicinski, M. Nonino, N. Okada, S. Okamura, J. P. Ostriker, R. Owen, A. G. Pauls, J. Peoples, R. L. Peterson, D. Petravick, J. R. Pier, A. Pope, R. Pordes, A. Prosapio, R. Rechenmacher, T. R. Quinn, G. T. Richards, M. W. Richmond, C. H. Rivetta, C. M. Rockosi, K. Ruthmansdorfer, D. Sandford, D. J. Schlegel, D. P. Schneider, M. Sekiguchi, G. Sergey, K. Shimasaku, W. A. Siegmund, S. Smee, J. A. Smith, S. Snedden, R. Stone, C. Stoughton, M. A. Strauss, C. Stubbs, M. SubbaRao, A. S. Szalay, I. Szapudi, G. P. Szokoly, A. R. Thakar, C. Tremonti, D. L. Tucker, A. Uomoto, D. Vanden Berk, M. S. Vogeley, P. Waddell, S.-i. Wang, M. Watanabe, D. H. Weinberg, B. Yanny, N. Yasuda, and SDSS Collaboration. The Sloan Digital Sky Survey: Technical Summary. *The Astronomical Journal*, 120(3):1579–1587, Sept. 2000.

[156] J. Zavala, M. R. Lovell, M. Vogelsberger, and J. D. Burger. Diverse dark matter density at sub-kiloparsec scales in milky way satellites: Implications for the nature of dark matter. *Physical Review D*, 100(6), Sep 2019.

[157] Z. C. Zeng, A. H. G. Peter, X. Du, A. Benson, S. Kim, F. Jiang, F.-Y. Cyr-Racine, and M. Vogelsberger. Core-collapse, evaporation, and tidal effects: the life story of a self-interacting dark matter subhalo. *Mon. Not. Roy. Astron. Soc.*, 513(4):4845–4868, 2022.

[158] A. Zentner, S. Dandavate, O. Slone, and M. Lisanti. A critical assessment of solutions to the galaxy diversity problem. *Journal of Cosmology and Astroparticle Physics*, 2022(7):031, July 2022.

[159] F. Zwicky. Die Rotverschiebung von extragalaktischen Nebeln. *Helvetica Physica Acta*, 6:110–127, Jan. 1933.

[160] F. Zwicky. On the Masses of Nebulae and of Clusters of Nebulae. *The Astrophysical Journal*, 86:217, Oct. 1937.

Appendix A

Appendix

A.1 Gravitational Lensing

Gravitational lensing is a phenomenon predicted by Einstein's theory of general relativity, whereby photons deviate from their original trajectories as they travel through locally curved space-time due to a massive object. It has become an indispensable tool in astrophysics and cosmology, offering insights into the distribution of dark matter, the study of distant galaxies, and the properties of the early universe. Gravitational lenses act as cosmic magnifying glasses, allowing the study of objects otherwise too faint or distant to observe. The material in this section mainly comes from the following sources [10, 81, 34, 116, 127, 30, 18].

A.1.1 Deflection Angle

The amount by which light is deflected due to bending of spacetime can be quantified in a deflection angle. The deflection angle determines how the background source appears to us. For strong gravitational fields, it can lead to multiple images, arcs, or even complete

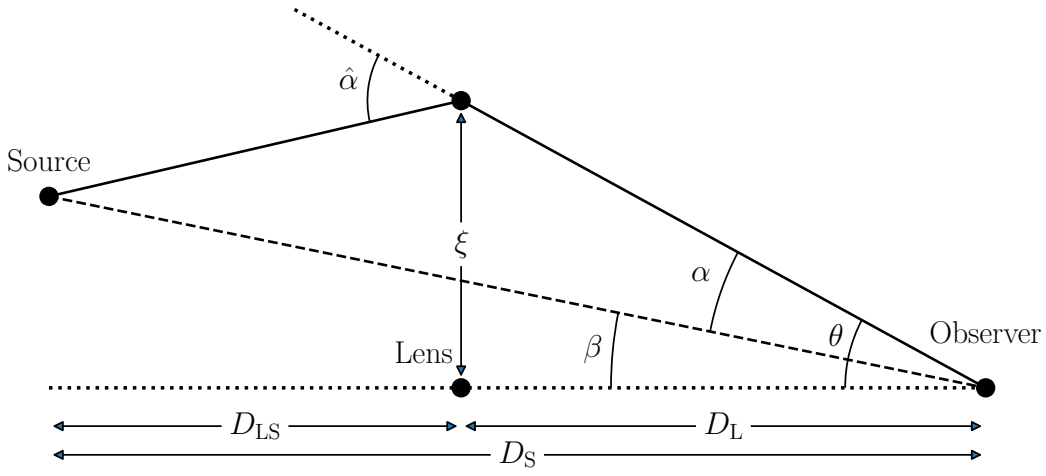

Figure A.1: Lens diagram showing the trajectory of a light ray (the solid line) emitted by a source S in a weak gravitational field and bent by a lens L. This effect produces an image labeled I which is seen by some observer O. The angle β is the angle of the position of the actual source S while θ is the angle of the position of the image I. The angle α is the angle between S and I measured by the observer at O, while the deflection angle is $\hat{\alpha}$. D_L, D_S, D_{LS} are the angular diameter distance to the lens, distance to the source, and distance between the source and lens respectively. Made with code snippet from [18].

rings known as Einstein rings, of the source. The deflection angle can be derived from the Schwarzschild metric describing a spherically symmetric mass. For light passing by this mass with an impact parameter that is much larger than the Schwarzschild radius, $\xi \gg R_s \equiv \frac{2GM}{c^2}$, the deflection angle is given by

$$\hat{\alpha} = \frac{4GM}{c^2 \xi} \tag{A.1}$$

where M is the mass of the lens, ξ is the impact parameter, and G and c are the gravitational constant and speed of light, respectively. This condition implies that the deflection angle will be small.

Figure A.2: Strong lensing luminous red galaxy LRG 3-757 distorting the light of a distant background galaxy. The lensing system is in nearly perfect alignment with our line of sight such that it has created an Einstein ring. Credit: ESA/Hubble and NASA

A.1.2 Lens Equation

Using the small angle approximation ($\tan\theta \simeq \sin\theta \simeq \theta$) in Fig. A.1, we find the relation:

$$D_{\mathrm{S}}\boldsymbol{\beta} = D_{\mathrm{S}}\boldsymbol{\theta} - D_{\mathrm{LS}}\hat{\boldsymbol{\alpha}}(\boldsymbol{\xi})\,. \tag{A.2}$$

Defining the reduced deflection angle as $\boldsymbol{\alpha}(\boldsymbol{\theta}) = \frac{D_{\mathrm{LS}}}{D_{\mathrm{S}}}\hat{\boldsymbol{\alpha}}(\boldsymbol{\theta})$ where $\hat{\boldsymbol{\alpha}}$ is a function of $\boldsymbol{\theta}$ because $\boldsymbol{\xi} = D_{\mathrm{L}}\boldsymbol{\theta}$, we arrive at the following form of the lens equation:

$$\boldsymbol{\beta} \equiv \boldsymbol{\theta} - \boldsymbol{\alpha}(\boldsymbol{\theta})\,. \tag{A.3}$$

If we have a perfect alignment, we can get an Einstein ring, as seen in Fig. A.2. In this case we arrive at the following expression:

$$\theta_{\mathrm{E}} = \sqrt{\frac{4GM}{c^2}\frac{D_{\mathrm{LS}}}{D_{\mathrm{L}}D_{\mathrm{S}}}}\,, \tag{A.4}$$

which gives us the Einstein radius via $R_{\rm E} = D_{\rm L}\theta_{\rm E}$. The size of the Einstein ring depends on the mass of the lens as well as its geometry.

A.1.3 Surface Density and Convergence

When observing cosmic structures such as gravitational lenses, an understanding of their three-dimensional density profile would be invaluable. Unfortunately, our observations are limited to two-dimensional projections of these mass profiles. To circumvent this limitation, we project the three-dimensional density onto a two-dimensional plane, yielding a surface mass density. We define the two-dimensional mass, or projected mass, as

$$M(R) = \int_0^R 2\pi R' \Sigma(R') dR' \,, \tag{A.5}$$

where $\Sigma(R)$ is the surface density and is given by

$$\Sigma(R) = \int_{-\infty}^{+\infty} \rho(r) dz \,, \tag{A.6}$$

with $r = \sqrt{R^2 + z^2}$. Essentially, this equation integrates the mass density along the line of sight. The surface mass density is critical in determining the gravitational lensing strength.

A pivotal quantity in gravitational lensing is the critical surface density, $\Sigma_{\rm crit}$. This is the threshold surface density required for a lens to produce multiple images of a background source. It is mathematically expressed as:

$$\Sigma_{\rm crit} = \frac{c^2}{4\pi G} \frac{D_{\rm S}}{D_{\rm L} D_{\rm LS}} \,. \tag{A.7}$$

Building on this, we introduce the convergence, κ, given by:

$$\kappa = \frac{\Sigma}{\Sigma_{\rm crit}} \,. \tag{A.8}$$

This dimensionless quantity gauges the strength of the lensing. It describes the local mass distribution within the lens and is directly related to the deflection of light rays. A convergence greater than 1, $\kappa > 1$, indicates strong lensing, capable of producing multiple images or Einstein rings, whereas $\kappa < 1$ signifies weak lensing, resulting in only minor distortions of the background source. The left panel of Fig. A.3 illustrates how the alignment of a lensing cluster and a background galaxy along our line of sight affects the lensing strength. The right panel showcases the strong lensing cluster, Abell 2218.

Further, we define the lensing potential, $\psi(\boldsymbol{\theta})$, as:

$$\psi(\boldsymbol{\theta}) = \frac{D_{\rm LS}}{D_{\rm L} D_{\rm S}} \frac{2}{c^2} \int dz, \Phi(D_{\rm L}\boldsymbol{\theta}, z) \,. \tag{A.9}$$

Taking the Laplacian of the lensing potential, we find its relationship to the convergence:

$$\nabla^2 \psi = 2\kappa(\boldsymbol{\theta}) \,, \tag{A.10}$$

which is simply the two-dimensional Poisson equation.

A.1.4 Magnification

One of the key effects of gravitational lensing is magnification, which refers to the change in the observed brightness of the source due to lensing effects. The Jacobian magnification matrix describes how the image of a source is deformed by the lens. The magnification

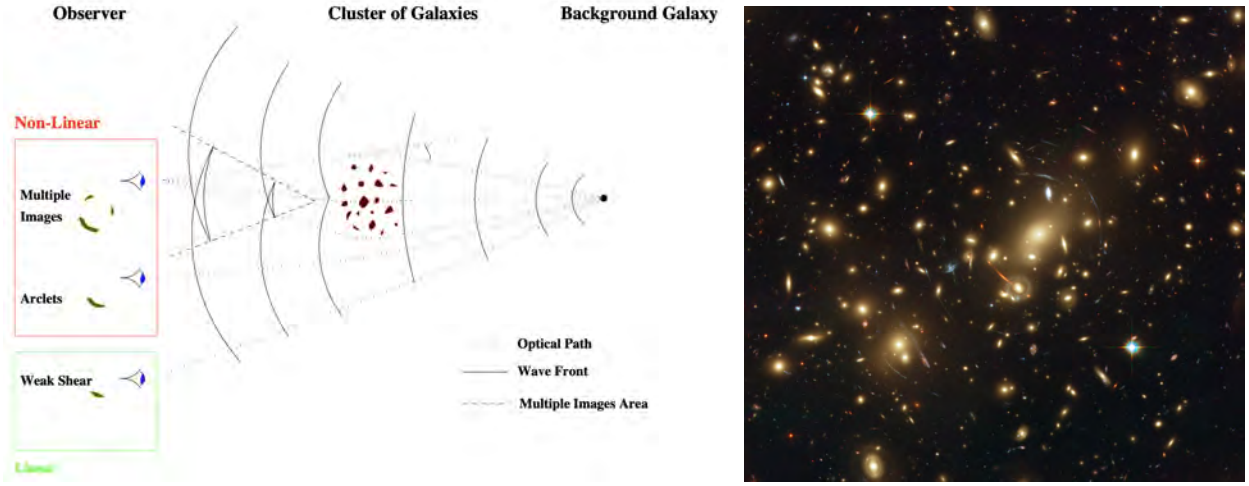

Figure A.3: Right: Depiction of a lensing cluster and a background galaxy, delineating regions of strong, intermediate, and weak lensing, resulting in multiple images, arclets, and weak shear. From [81]. Left: Hubble Space Telescope image of the strong lensing cluster Abell 2218, featuring multiple images and arcs of background galaxies. Credit: ESA/Hubble, Johan Richard (Caltech, USA).

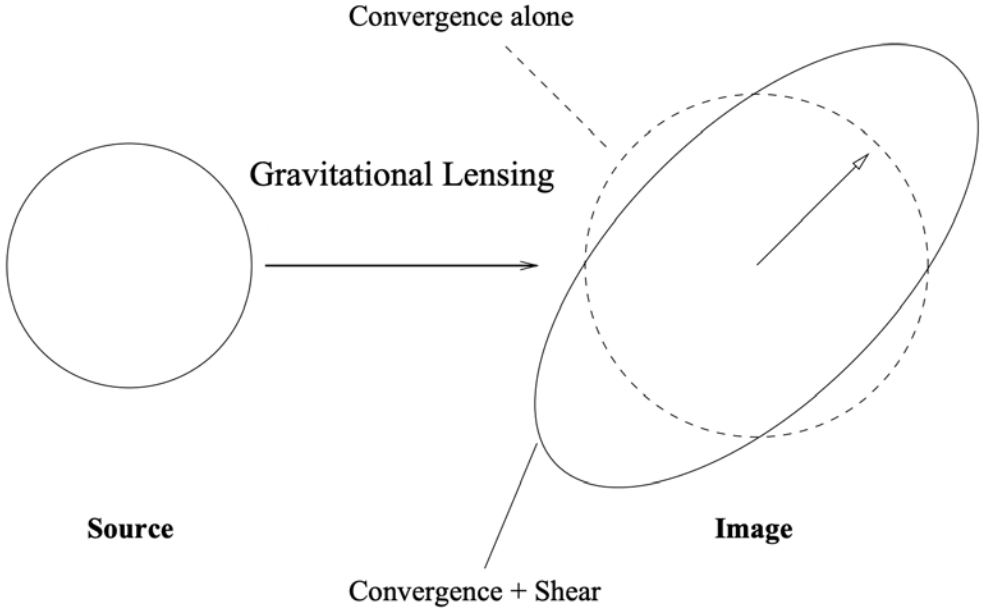

Figure A.4: Illustration of the impact of convergence, with and without shear, on the distortion of the lensed image. From [142].

matrix $\mathcal{A}$ is given by

$$\mathcal{A}(\boldsymbol{\theta}) = \frac{\partial \boldsymbol{\beta}}{\partial \boldsymbol{\theta}} = \left(\delta_{ij} - \frac{\partial^2 \psi(\boldsymbol{\theta})}{\partial \theta_i \partial \theta_j}\right) = \begin{pmatrix} 1-\kappa-\gamma_1 & -\gamma_2 \\ -\gamma_2 & 1-\kappa+\gamma_1 \end{pmatrix} \tag{A.11}$$

where $\gamma \equiv \gamma_1 + i\gamma_2$ is the shear, $\gamma_1 = \frac{1}{2}(\psi_{,11} - \psi_{,22})$ and $\gamma_2 = \psi_{,12}$, and κ is the convergence as defined in Eq. (A.8). The shear describes the tangential stretching distortion in the image, whereas the term with the convergence represents the magnification of the image. See Fig. A.4 to see how the convergence alone, compared to the convergence with shear, distort a lensed image.

The magnification μ is given by

$$\mu^{-1} = (\det \mathcal{A})^{-1} = (1-\kappa)^2 - \gamma^2\,, \tag{A.12}$$

where $|\gamma|^2 = \gamma_1^2 + \gamma_2^2$. The magnification quantifies how much brighter the lensed image is compared to the actual source. It provides insight into the mass distribution of the lensing object through the convergence and shear.

A.1.5 Critical Curves and Caustics

In certain configurations, the magnification can become theoretically infinite, or $\det(\mathcal{A}) = 0$. The points at which this occurs are called critical curves, which are in the image plane. The corresponding features of the critical curves mapped onto the source plane via Eq. (A.3) are called caustics. Caustics are where light from a source is highly focused, leading to dramatic increases in brightness and the formation of multiple images or arcs. Examples of such formations can be found in Fig. A.5.

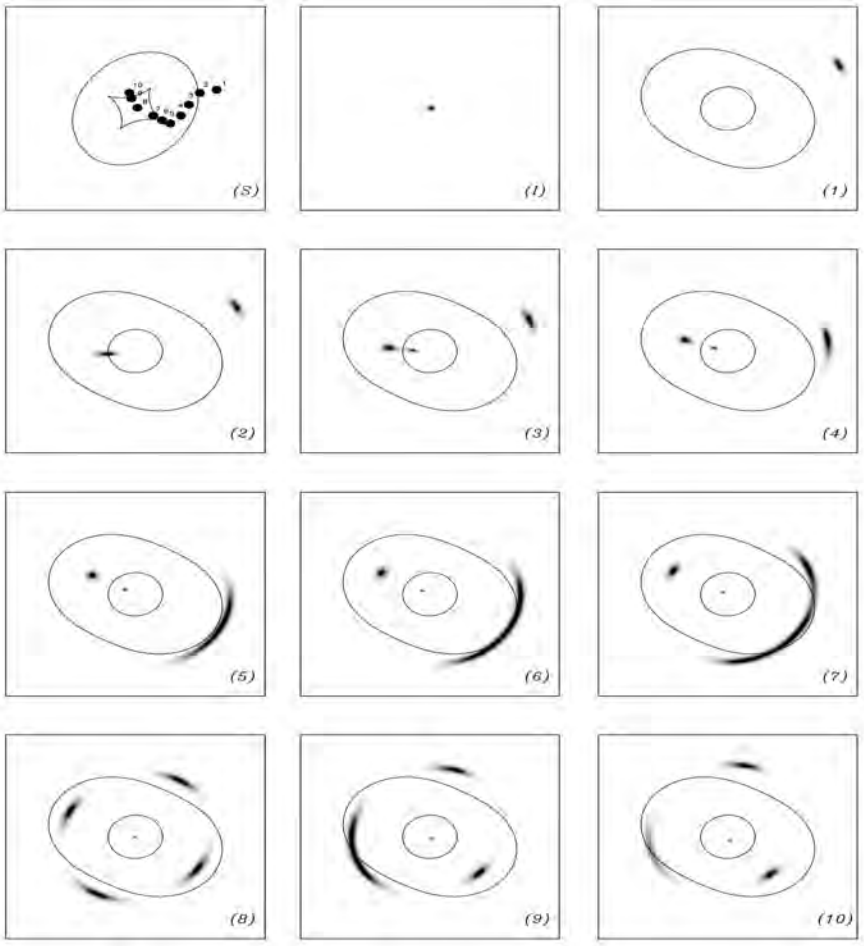

Figure A.5: Gravitational lensing illustration with an elliptical lens model. Panel S depicts the source plane, featuring caustic lines and ten points, each signifying a source location. Panel I demonstrates the image in the absence of lensing. Panels 1 through 10 show the lensed images corresponding to each source position in panel S relative to the caustic. The panels showcase several lensing effects, including characteristic ones such as arcs and Einstein crosses, based on the positioning of the source relative to the caustics. [81]

Critical curves and caustics are central to gravitational lensing. They provide insights into the mass distribution of dark matter in the lensing object. Strong lensing of distant galaxies is a favorable and fortunate configuration, as it allows us to study the properties of distant galaxies and enhance our understanding of the early universe.

A.2 Small scale crisis and Motivations for SIDM

ΛCDM model successfully explains the large-scale structure. It is consistent with a wide range of observational data, including the CMB, the distribution of galaxies, and the number of galaxy clusters in the Universe [135, 111, 137]. Moreover, simulations based on ΛCDM reproduce the universe on large scales remarkably well [97, 137].

Despite its successes, the ΛCDM model faces challenges on small scales. For instance, it predicts a larger number of small satellite galaxies around Milky Way-like galaxies than observations show, which is a problem known as the "missing satellites problem" [22]. It also predicts a cusp in the density profile of dark matter in galaxies, which is in contrast to the observed cores, a discrepancy called the "core-cusp problem" [115, 35, 22]. The "too-big-to-fail" (TBTF) problem arises from the observation that the most massive subhalos predicted by CDM simulations are denser than any of the observed satellite galaxies of the Milky Way [19, 107]. Finally, a problem referred to as the "diversity problem" refers to the diversity in rotation curves in low surface brightness galaxies, despite CDM simulations predicting them to be uniform [72, 117].

These small-scale problems have motivated the exploration of alternative dark matter models. The SIDM model has emerged as a viable competitor to the ΛCDM model. In SIDM, dark matter particles can interact with each other, not just through gravity but also through dark sector forces. This leads to potential solutions to each of these small scale problems [145].

A.2.1 Core-Cusp Problem

The core-cusp problem is one of the most significant and notable challenges faced by the ΛCDM model. It predicts high-density cusps at the centers of dark matter halos, while observations show flat density cores in dwarf and low surface brightness galaxies [121, 115,

35, 22]. It has been suggested that feedback from star formation and supernovae could potentially flatten the central density profiles, providing a possible solution to this problem while maintaining the CDM model [35], but it is not clear whether this can fully resolve the problem, nor whether we know the baryonic physics well enough to simulate it [139]. SIDM can provide a compelling solution to this problem. The self-interactions between dark matter particles can lead to the transfer of heat and mass from the inner dense core to the outer dilute halo, which creates a cored profile [47]. This mechanism has been shown to be effective in producing core profiles in SIDM simulations that are consistent with observations [47].

A.2.2 Too-Big-To-Fail Problem

The "too big to fail" problem predicts a population of dense, massive subhalos that should host bright dwarf galaxies, but no such galaxies are found in the Local Group [19]. SIDM can potentially solve this problem. The self-interactions can redistribute the dark matter in subhalos and reduce their central densities which makes them less likely to host bright galaxies, an effect shown in SIDM simulations [76].

A.2.3 Diversity Problem

The diversity problem refers to the diverse range of inner slopes in galactic rotation curves seen in spiral galaxies, which is difficult to reproduce in the ΛCDM model [105]. This problem points to a shortcoming of ΛCDM on galactic scales and suggests that the nature of dark matter and galaxy formation may not be fully understood [72, 117]. SIDM thermalizes halos on shorter timescales than baryonic feedback, thus SIDM halos are generally insensitive to feedback during its formation history [117, 158, 72]. Scattering also redistributes matter in SIDM halos, which opens the door to a wider range of possible rotation curves, matching the observed diversity [158, 72]. It should be noted that a recent study that looked at

90 galaxies from the Spitzer Photometry and Accurate Rotation Curves survey found no preference between the SIDM model and CDM that is affected by feedback, where both are able to explain diversity in spiral galaxies, while CDM that was not affected by feedback was unable to explain them [158].

A.2.4 Missing Satellites Problem

The missing satellites problem is another discrepancy between the ΛCDM model and observations. The ΛCDM model predicts a much larger number of small satellite galaxies around Milky Way-like galaxies than what is observed [79]. SIDM has been proposed as a potential solution to this problem. The dark matter particle self-interactions can lead to the evaporation of smaller dark matter subhalos and reduce the number of visible satellite galaxies. Recent simulations have shown that SIDM can indeed produce a satellite galaxy population that is in better agreement with observations [146]. On the other hand, recent observations and improved simulations have begun to alleviate this problem. It is now understood that much of the missing satellites could be too faint to detect with current telescopes, and the inclusion of baryonic physics in the simulations can significantly reduce the number of bright satellites [22].